

MASTER THESIS

Estimation of dosimetric uncertainties of dose accumulation using different deformable image registration strategies in the pelvic region

carried out for the purpose of obtaining the degree of Diplom-Ingenieurin

submitted at TU Wien

Faculty of Technical Physics

by

Maude CORNU

Mat. No.: 12227685

under the supervision of

Univ.Prof.Dipl.-Ing. Dr Dietmar Georg (TU Wien)

Dipl.-Ing. Wolfgang Lechner, PhD (MedUni Wien)

Wien, December 10, 2024

Signature



Die approbierte gedruckte Originalversion dieser Diplomarbeit ist an der TU Wien Bibliothek verfügbar
The approved original version of this thesis is available in print at TU Wien Bibliothek.

Affidavit

I declare in lieu of oath, that I wrote this thesis and carried out the associated research myself, using only the literature cited in this volume. If text passages from sources are used literally, they are marked as such. I confirm that this work is original and has not been submitted for examination elsewhere, nor is it currently under consideration for a thesis elsewhere. I acknowledge that the submitted work will be checked electronically-technically using suitable and state-of-the-art means (plagiarism detection software). On the one hand, this ensures that the submitted work was prepared according to the high-quality standards within the applicable rules to ensure good scientific practice "Code of Conduct" at the TU Wien. On the other hand, a comparison with other student theses avoids violations of my personal copyright.

Place and Date

Signature

Acknowledgments

First and foremost, I would like to thank my thesis supervisor, Dr. Wolfgang Lechner, for supporting me throughout this thesis and for always taking the time to give me feedback, answer my questions and share his expertise with me.

I would also like to thank Univ.-Prof. DI Dr. Dietmar Georg for giving me the opportunity to carry out my thesis at the Department of Radiation Oncology of the Medical University of Vienna and for his valuable insights on my work.

A special thanks to my friends for their constant encouragement and the joy they bring into my life.

Finally, I would like to express my deep gratitude to my family for their ongoing support during my studies, and especially to my parents for their invaluable help along the way.

Contents

Abstract	viii
1 Introduction	1
1.1 Physical background	1
1.1.1 Physical principles of external radiation	1
1.1.2 Photon-matter interactions	3
1.2 Medical background	6
1.2.1 Cancer	6
1.2.2 Treatment of cancer	7
1.2.3 Radiation therapy	10
1.2.4 Radiobiology	11
1.3 Radiation therapy process	15
1.3.1 CT scan	15
1.3.2 Treatment planning	16
1.3.3 AI segmentation	19
1.3.4 Re-irradiation	21
1.3.5 Registration	22
1.3.6 Dose accumulation	23
1.4 Aim of the thesis	26
2 Material and Methods	27
2.1 Patient cohort	27
2.2 RayStation	28
2.2.1 Treatment planning system	28
2.2.2 Deformable registration algorithm	28
2.3 3D Slicer	29
2.3.1 Elastix	29
2.3.2 TotalSegmentator	30
2.4 Previous work	31
2.5 Segmentation comparison	32
2.6 Registration evaluation	33
2.7 Dose mapping evaluation	34
2.8 Data Handling	35
2.9 Dose uncertainties calculation	38

2.10	Qualitative evaluation	40
2.11	Quantitative evaluation	41
2.11.1	Metrics	41
2.11.2	Statistics	43
3	Results	45
3.1	Preliminary results	45
3.2	Segmentations	46
3.3	Registrations	48
3.4	Dose mapping	53
4	Discussion	57
4.1	Segmentations	57
4.1.1	Structure correspondence	57
4.1.2	Segmentation performance	59
4.1.3	Outlook and limitations	61
4.2	Registrations	63
4.2.1	Controlling structures	63
4.2.2	Data variability	65
4.2.3	Bowel	66
4.2.4	DSC performance	66
4.2.5	Anal canal and urethra	67
4.2.6	Outlook and limitations	67
4.3	Dose mapping	68
4.3.1	Body contour	68
4.3.2	Gradients	70
4.3.3	Geometric uncertainties	72
4.3.4	Systematic errors	73
4.3.5	Second treatment	74
4.3.6	Outlook and limitations	75
5	Conclusion and Outlook	77

Abstract

Cancer is the second most common cause of death in the world, responsible for approximately 10 million deaths in 2019. Survival rates have improved significantly in the last 50 years, and the increase in life expectancy after a radiation therapy resulted in an increase in the incidence of recurrences and new cancers in people who have already undergone radiotherapy in the past. Hence, there is a growing usage of re-irradiation in recent practice. For patient safety, it is necessary to use registration in order to localize previously irradiated tissue from a former treatment and consider it as background of the new treatment. However, there is no common standard or protocol for re-irradiation and a lack of clinical consensus, as well as common ground for the studies done on this subject. Moreover, the evaluation of dose mapping is complicated as there is no ground truth to compare results to. This thesis uses data from the ReCare trial to explore possible data analysis strategies and aims to calculate the best estimate of dose deformation by combining different registrations, and derive dosimetric uncertainties from it. It was also an additional goal of the project to determine whether it would be possible to use an AI-powered segmentation tool as QA for the manual registrations coming from different institutions in the ReCare cohort.

"Whole body" segmentations were performed with TotalSegmentator on 3D Slicer and compared with the manual segmentations on RayStation with HD and DSC metrics. To increase the number of organs to compare, the AI-colon and AI-spinal cord were modified to a pseudo-AI rectum and a pseudo-AI cauda equina, matching the ReCare segmentations. On RayStation, a rigid image registration (RIR) was performed, and, using ANACONDA, an intensity-based deformable image registration (DIR) (noContROI), as well as two hybrid DIRs (ContROI & Wall). On 3D Slicer, an intensity-based DIR was performed using Elastix (SDIR). The calculation of dosimetric uncertainties in dose deformation was based on a best estimate made of the five registrations, assuming that a geometry-based registration could deform dose because of the spatial correlation between anatomy and dose distribution. The highest 1% and average standard deviation of dose ($u_{D,1\%}$ & $u_{D,av}$) were recorded for each organ-at-risk (OAR) and the PTVs of the second treatments.

A very good similarity (lowest Dice similarity coefficient (DSC): Rectum 0.79) was found between AI and manual segmentation. However, a low structure correspondence was found: only three organs are segmented by both methods, whereas the list of OARs in the ReCare trial counts ten of them.

Moreover, the theoretical time gain could not be made profitable because of the capacities of the computer used. The general DSC means retrieved were 0.81 for ContROI, 0.74 for noContROI, and 0.70 for SDIR. The general HD means measured were 1.57 for ContROI, 1.87 for noContROI and 1.69 for SDIR. DIR performed particularly better for filling organs such as the bladder, the bowel and the rectum, which all exhibited significant differences between algorithms. Significant DSC differences were also found between the two intensity-based algorithms, ANACONDA gave better DSC values, while Elastix performed better for HD measurements. Dosimetric uncertainties were found to be generated by a complex combination of geometric uncertainties, a steep gradient dose distribution, and a certain dose magnitude. Geometric variations were found to be due to image information, to the use of controlling structures, and to differences in the handling of body contours. For intensity-caused variations, the anal canal region was identified as being prone to dosimetric uncertainties. The presence or absence of the RIR in the calculation of dosimetric uncertainties was not found to be significant in the majority of OARs or in the PTVs. The PTVs' $u_{D,av}$ range from 0.30% to 13.90%, which highlights how case-specific the impact of dosimetric uncertainties is on the patient's safety.

The lack of structure correspondence between manual and AI-segmentation limits the use of TotalSegmentator as a QA tool for the ReCare manual segmentations. The registration analysis resulted in the observation that hybrid DIR gives better results than intensity-based DIRs, as it offers more subjectivity to match the specificity of each case. The differences between the two intensity-base DIRs were found to be due to their use of different optimization metrics. The significant dosimetric uncertainties in the body contour were attributed to the inability of the RIR to correct for them. Quantifying and localizing dosimetric uncertainties, such as those extracted in the new treatment PTVs, demonstrates how incorporating these uncertainties into treatment planning can potentially increase patient safety. Further research using additional patients is necessary to strengthen the results, confirm the trends identified, and deepen the analysis of factors of dosimetric uncertainties. Additionally, examining other anatomical regions where TotalSegmentator might be more suitable and DIR algorithms could yield different results would be an interesting direction for further investigations.

List of Figures

1.1	Dose distribution of different technologies' treatment plans [9].	2
1.2	Relative importance of the three main photon interaction processes with atomic number (Z) and photon energy [13]	3
1.3	Photoelectric effect (a) and alternative ways of excess energy release after an inner electron shell vacancy is filled (b)&(c). [11]	4
1.4	Compton effect [11]	5
1.5	Pair production [11]	6
1.6	Cell cycle [44]	11
1.7	Cell survival curve [50]	12
1.8	GTV, CTV, PTV, and ITV schematic definitions (ICRU Report 62) [71]	17
1.9	Schematic representation of CNN segmentation [82]	19
1.10	U-Net architecture [84]	20
1.11	Schematic representation the use of image registration to map dose distribution [101]	23
1.12	Current landscape of dose mapping use cases [101]	24
1.13	Illustration of the expected anatomical variations, re-irradiation suffers from inter-treatments variations [101]	25
2.1	Basic modules of Elastix registration [106]	29
2.2	Some segmented structures on whole body CT [108]	30
2.3	Schematic representation of the segmentation workflow	33
2.4	Schematic representation of the registration workflow	33
2.5	Schematic representation of the dose accumulation workflow	34
2.6	Simplified schematic representation of the complete workflow	37
2.7	DICOM data tags	39
2.8	Metadata	40
2.9	DSC Volume dependence [117]	41
2.10	Boundary delimitation similarities with HD [118]	42
2.11	Dose-volume histogram of patient n°2339	43
3.1	Frequency of each organ being used as controlling ROI across cohort . .	45
3.2	General box plot of the four segmented structures	47
3.3	Volume variations of the five segmented structures	47
3.4	Average volume variation for analyzed organs	48

3.5	General box plot of the three methods	49
3.6	Bladder box plot of the three methods	50
3.7	Bowel box plots of the three methods	51
3.8	Lumbar plexuses box plots of the three methods	51
3.9	Cauda equina box plots of the three methods	52
3.10	Bar chart of the three methods' DSC and HD for filling organs	52
3.11	Dose uncertainties due to controlling ROI-caused geometric variations in steep dose gradients. Patient 2694	53
3.12	Dose uncertainties due to controlling structures outside of steep dose gradient. Patient 2339	53
3.13	Dose uncertainties due to intensity-caused geometric variations. Patient 2281	54
3.14	Important deformation handled differently by the registrations taking place out of the high dose region do not generate dosimetric uncertainties. Patient 2694	54
3.15	Differences in contour dose uncertainties between all reg. and noRIR.	55
4.1	Difference between spinal cord and cauda equina	57
4.2	Difference between colon and rectum	58
4.3	Differences in bowel delineation	58
4.4	Differences in kidneys delineation	59
4.5	Influences on bladder delineation	60
4.6	Pseudo-AI rectum delineation process, with ReCare rectum in orange, Slicer colon in yellow, and pseudo-AI in pink	61
4.7	Example of contour improvement with controlling ROI (Patient 2281)	63
4.8	Example of significant bladder volume variation (Patient 2551)	64
4.9	Anatomical location of the plexuses (green & blue) and cauda equina (yellow)	65
4.10	Importance of good contour match for patient 2282	69
4.11	Impact of dose homogeneity on dosimetric uncertainties. Patient 2219	70
4.12	Dosimetric uncertainties due to intensity-based geometric uncertainties in steep dose gradient area. Patient 2694	71
4.13	Dosimetric uncertainties due to controlling structures-generated geometric uncertainties in steep dose gradient area. Patient 2551	71
4.14	Dose difference between the original SDIR and checkSDIR files, Patient 2281	73
4.15	Dose difference between the original Wall file and the exported and directly re-imported Wall file, Patient 2694	74
4.16	Dose distribution in different planes. Patient 2319	75
5.1	Checklist method	95

List of Tables

2.1	List of analyzed organs for the pelvic region	27
2.2	Different runtime and memory requirements for whole body CT [108] . .	31
3.1	Comparison of methods (all 10 organs) from project [109]	45
3.2	Means and standard deviations of the DSC and HD of the five segmented structures	46
3.3	Means and standard deviations of the DSC and HD of the three methods	48
3.4	Statistical comparisons between different methods (all 10 organs)	49
3.5	Comparison of methods on selected structures (DSC p-values)	50
3.6	Comparison of methods on selected structures (HD p-values)	50
3.7	Mean \pm std of $u_{D,1\%}$ and $u_{D,av}$ for every organ	56
3.8	p-values for $u_{D,1\%}$ and $u_{D,av}$ between all reg. and noRIR calculations . .	56
3.9	RSD values of the PTV1 of the second treatment, all reg. calculation . .	56
5.1	Organs used as controlling ROIs in ContROI and Wall methods	94

Glossary

3DCRT 3D conformal radiation therapy.

AI artificial intelligence.

ANACONDA anatomically constrained deformation algorithm.

CBCT cone beam computed tomography.

CIOD composite information object definition.

CNN convolutional neural network.

CT computed tomography.

CTV clinical target volume.

DCNN deep convolutional neural network.

DICOM digital imaging and communication in medicine.

DIR deformable image registration.

DMA dose mapping/accumulation.

DSC Dice similarity coefficient.

DVF deformation vector field.

DVH dose volume histogram.

EBRT external beam radiotherapy.

FEM finite element method.

GTV gross target volume.

HD Hausdorff distance.

HU Hounsfield unit.

ICRU international commission on radiation units and measurements.

IGRT image-guided radiation therapy.

IMRT intensity-modulated radiation therapy.

ITK insight segmentation and registration toolkit.

ITV internal target volume.

LET linear energy transfer.

LINAC linear accelerator.

MLC multileaf collimators.

MR magnetic resonance.

OAR organ at risk.

PRV planning organ-at-risk volume.

PSQA Patient specific quality assurance.

PTV planning target volume.

QA quality assurance.

RBE relative radiobiological effectiveness.

RIR rigid image registration.

ROI region of interest.

RSD relative standard deviation.

RT radiation therapy.

RTT radiotherapy technologist.

TPS treatment planning system.

VMAT volumetric modulated arc therapy.

XAI explainable artificial intelligence.

1 Introduction

1.1 Physical background

1.1.1 Physical principles of external radiation

X-rays are able to damage cells' DNA because they belong to ionizing radiation. Ionizing an atom stands for ejecting an orbital electron and hence forming a positive ion [1]. This ionization process can take place in a direct or indirect manner. A direct ionization radiation interacts directly with the target in the cell that needs to be damaged, which is most of the time the DNA. Indirect ionization radiation will interact with other molecules or atoms, and by ejecting an orbital electron, they will create free radicals [2]. It is the free radicals that will then damage the target, and not directly the beam's particles. Which of these two processes will take place depends on the radiation source. Charged particles are involved in direct ionization while uncharged particles will reach the target indirectly [3].

In brachytherapy, β -rays (which have mass and charge) and γ -rays (which have no mass or charge) originating from the radioactive decay of the radionuclide, can also be used to reach the target. The difference between X-rays and γ -rays is their origin. X-rays are produced by bremsstrahlung, while γ -rays are emitted by excited nuclei, but their energies are similar [4]. These two particles are therefore functionally identical and will damage the DNA in the same way.

In clinical EBRT, LINACs are used to generate megavoltage X-rays (4-25 MV). Monoenergetic electrons of energies between 4 and 25 MeV are used as a source to produce the X-ray beam [5]. An X-ray beam is created by accelerating electrons to energies where Compton scattering and pair-production are predominant. The electrons are accelerated by a tuned-cavity waveguide, where a radiofrequency is used to create a standing or travelling wave. Electrons then undergo a rapid deceleration on a high Z target material that will produce an X-ray spectrum by bremsstrahlung radiation, into which a part of the electrons' kinetic energy has been converted [6]. LINACs have many advantages as they not only produce a reliable, flexible and accurate radiation beam, but the machine can also be turned off when not needed and its use doesn't require heavy shielding but the one to protect from radiation.

In LINACs, collimators are used to change the shape and size of the beam. Newest technologies use multileaf collimators (MLC), made of more than 50 tungsten leaf pairs able to move independently into the beam path during a step-and-shoot or dynamic process, allowing to create a limitless number of beam shapes [7]. Techniques in photon external beam radiotherapy evolve constantly, however there are three main techniques, evolutions of one another, that are the most commonly clinically used.

3D conformal radiation therapy (3DCRT) uses a 3D CT scan to plan the treatment. Multiple cross firing is used to deliver the dose to the target, which means that the conformal beams are fired from different angles [8].

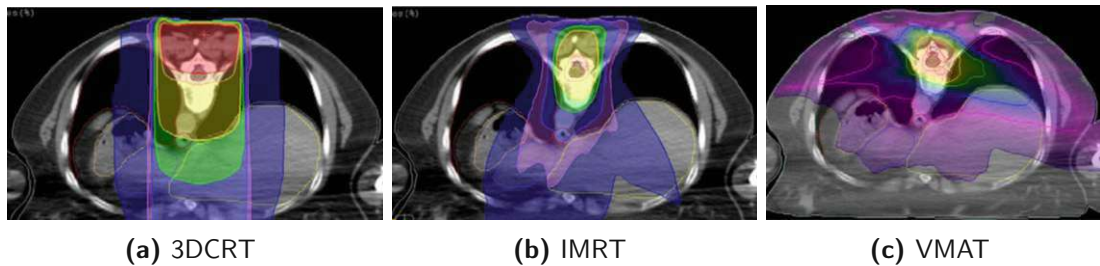


Figure 1.1: Dose distribution of different technologies' treatment plans [9].

Intensity-modulated radiation therapy (IMRT) allows not only to change the shape of the beam but also its intensity profile, which makes this technique more efficient than 3DCRT (Figure 1.1) [10]. The beam is broken up into many smaller beam 'segments' in order to design an appropriate fluence profile. The tuning of specific segments of the beam makes this technique very precise. An increased precision also leads to the possibility of using higher doses, as it is assured that it won't reach healthy tissues. Volumetric modulated arc therapy (VMAT) is an evolution of IMRT, or, more precisely, its dynamic application. Indeed, IMRT sends beams of varying doses of radiation from a sequence of fixed angles. Hence, the MLC will be modified following the step-and-shoot process. However, in VMAT, the gantry doesn't have to stop to deliver radiation, forcing the MLC to change in a dynamic way to allow the continual adjustment of the beam shape. Each rotation is called an arc, and multiple arcs can be used depending on the complexity of the treatment. VMAT allows a more precise dose-to-target delivery, as well as a time gain because of its dynamic nature.

Image-guided radiation therapy (IGRT) is an enhancement that is typically used in conjunction with both IMRT and VMAT, using an imaging technique to validate the tumor position improves the precision and accuracy of these radiation delivery techniques. With this technique, corrections in the beam can be made for differences in the patient positioning or anatomy before the administration of the treatment [10]. Indeed, the tumor can shift in the body, but also shrink due to the treatment, and if a new image isn't done, the high dose doesn't reach (only) the target and damages healthy tissues.

Making new images before every fraction adds some treatment time and costs, and depending on the imaging technique, also adds radiation exposure to the patient. However, it makes the treatment a lot more accurate and minimizes drastically the risk of delivering high doses to healthy tissues. Moreover, it allows to reduce the safety margins and again, reduce toxicity to healthy tissues.

1.1.2 Photon-matter interactions

Once the dose prescription and the tumor volume are defined, the X-ray beams' energies and positions will be calculated for an optimized treatment. For these calculations to have a realistic rendering of the beam's path in the body and of the actual dose reaching the target, they take into account the interactions taking place between the photons and the matter. Photon-matter interactions are of interest because they can scatter photons, hence change the beam trajectory, or they can also absorb photons, hence attenuate the beam. Different types of interactions can take place between photons that constitute the beam and the medium it goes through. The type of interaction that will most likely take place will depend on the photon energy and the atomic number of the absorber (Figure 1.2). The effective atomic number of soft tissue is close to the one of water (10) and can be estimated to 7.4 [11].

The energy level of the X-ray beams used for treatment will depend on the location of the cancer, more precisely on how deep in the body it seats [12]. For skin cancers, superficial X-rays are used, in the range of 10 keV and 100 keV. Orthovoltage X-rays (100-500 keV) are used for slightly deeper tissues. For reaching deep-seated tumors, megavoltage X-rays are used. They range from 1 MeV up to 25 MeV (X-rays above 15 MeV are rarely used). In this context, there are three different types of photon interactions: photoelectric scattering, Compton scattering, and pair production [11]. Each of them is dominant in different contexts.

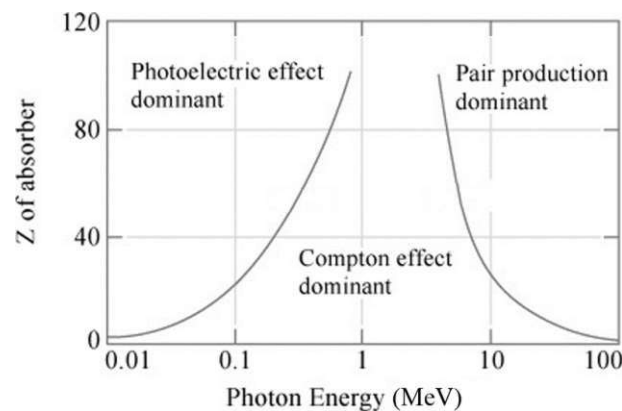


Figure 1.2: Relative importance of the three main photon interaction processes with atomic number (Z) and photon energy [13]

The photoelectric effect, or photoelectric absorption, takes place when the photon interacts with an inner shell electron of the atom, then called "photoelectron", and removes it from its shell. The incident photon is completely absorbed in the interaction (Figure 1.3a). Once the photoelectron has left the atom, it needs to be stabilized and will use an outer-shell electron to fill the vacancy left in the inner shell. Such rebalancing transmits energy as the electron drops to the inner shell, this energy will be then be emitted as characteristic radiation (Figure 1.3b) or Auger electron (Figure 1.3c) [14].

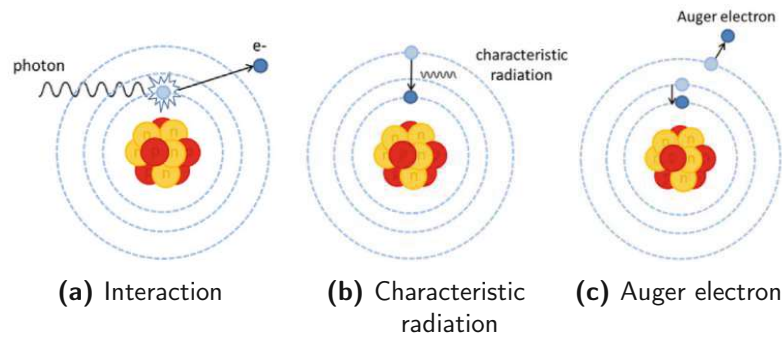


Figure 1.3: Photoelectric effect (a) and alternative ways of excess energy release after an inner electron shell vacancy is filled (b)&(c). [11]

In this interaction, the energy is conserved: the energy of the incident photon is firstly used to remove the photoelectron from the shell, the remaining energy is then used as kinetic energy for the photoelectron. The probability of occurrence follows:

$$p \left(\frac{Z^3}{E^3} \right) \quad (1.1.1)$$

with p , the physical density of the attenuation medium, Z , its atomic number, and E , the energy of the incident photon [15].

It is also more likely to take place when the energy of the incident photon is equal or slightly greater than the binding energy of the electron in the atom, hence the probability becomes really small once the energy reaches 140 keV.

Compton scattering is dominant in human tissues with radiation energies between 30 keV and 30 MeV. It takes place between a photon and a free electron, or a loosely bound valence shell electron. It is an inelastic scattering process as the resultant incident photon changes direction and transfers energy to the recoil electron (Figure 1.4). Indeed, the loss in the photon energy corresponds to the gain in energy of the recoil electron.

This energy loss generates an increase in wavelength (λ), which is called Compton shift and determined by:

$$\frac{h}{(m_o c)}(1 - \cos(\theta)) \quad (1.1.2)$$

with h , Planck's constant, m_o , the rest mass of the electron, c , the speed of light, and θ , the angle through which the photon is scattered [16].

Hence showing the significant role of the scattering angle theta in the energy redistribution, as energy can be defined as $E_\lambda = hc/\lambda$ [16]. The energy of the scattered photon decreases with increasing scattering angle. The probability of the Compton effect taking place is directly proportional to the electron density and the physical density of the absorbing material, but only weakly dependent on the photon energy [17].

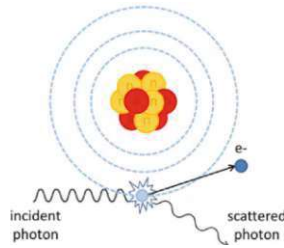


Figure 1.4: Compton effect [11]

The third interaction is pair production and takes place when a photon interacts with the electric field of a nucleus. The photon undergoes a change of state and the creation of a subatomic particle and its antiparticle takes place, resulting in the total attenuation of the incident photon (Figure 1.5). In this interaction, the principle that energy and mass are interchangeable ($E = mc^2$) is used as matter is created from energy of the massless photon [18]. Therefore, for this interaction to take place, the energy of the incident photon needs to be of at least the sum of the resting masses of the resulting particles. Different pairs can be created by this effect, but in the energy range used in radiotherapy, the most common pair is an electron and a positron, which necessitates a high energy incident photon of at least 1.022 MeV. If the energy of the incident photon is greater than 1.022 MeV, it will be shared between the two particles as kinetic energy.

The probability of pair production follows

$$ZE(-1.022)p \quad (1.1.3)$$

with Z , the atomic number of the attenuator, E , the incident photon energy, and p , the physical density [15].

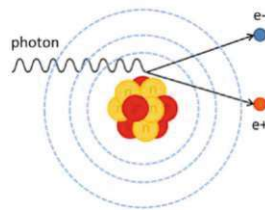


Figure 1.5: Pair production [11]

In medical imaging, techniques can be used to reduce the photon-matter interactions for a better image. However, in the context of radiotherapy, these interaction cannot be avoided but are instead taken into account for a more realistic treatment approach.

1.2 Medical background

1.2.1 Cancer

Cancer is defined as uncontrolled cell growth and multiplication. It is a disruption of regulating mechanisms that leads to the formation of an abnormal tissue mass, called a neoplasm or tumor, made of the body's own degenerate cells. What makes a tumor cancerous is its behavior, or dignity. A malignant (cancerous) tumor has for example a rapid growth, blurred limits, is invasive or even destructive, spreads and forms metastases [19]. The starting point of any cancer is an abnormal growth of cells. However, the location of these cells can vary, as any cell in the human body can be the origin of a tumor.

Cancers are differentiated depending on where it began. Carcinomas originates in the epithelium, sarcomas in the mesenchyme, leukemia in blood and lymphomas in the lymphatic system. At the beginning, the tumor is small and can get the nutrients and oxygen that it needs from the nearby blood vessels. As it grows, it will push the tissues cells nearby, damaging or even destroying them. The consequences of such a growth can be the loss of function of the neighboring organs, stenoses, circulatory disorders, bleedings due to vascular erosion or important disturbances of the metabolism [20].

As stated above, the limits of a tumor are blurred, which means that the cells don't really stick together, which makes it easier to spread. The tumor tissue can then be carried away via bloodstream, lymphatic system or even into a cavity, and will then create daughter tumors with no continuity to the primary one called metastases [21]. This is considered an advanced stage of cancer. However, a tumor can also be at a pre-cancerous stage, which means that the structural and functional changes have already taken place in the cells, but the tumor has not been invasive to neighboring tissues yet. This is the best stage for a cancer to be diagnosed in, as it is still localized, and the chances are higher to eradicate it completely [22].

Cancer is caused by a gene damage leading to cell mutation. This genetic change will modify the orders that any cell follows about when to grow, work, divide and die. These genetic mutations can be inherited, i.e. passed on by one parent, or acquired during lifetime. The most common risk factors for acquired genetic changes are usually age, smoking and sun exposure [23]. Some genes are considered specific to cancer, when these genes are silenced, they cannot do their work anymore, increasing the chances for a tumor to develop. Furthermore, when talking about mutation, it is important to stress that it is not necessary a single mutation that will cause cancer but more likely a build-up of mutations acquired during a period of time [24].

1.2.2 Treatment of cancer

The choice of treatment type for a patient with cancer can vary a lot depending on the situation. The most common factors assessed to choose a treatment are the type of cancer, its location, its stage and whether it has spread or is affecting other organs. However, the general health of the patient as well as their age and medical history must also be considered [25]. A treatment can have different goals: cure, control, or palliation. A treatment with curative goal will aim to eliminate the tumor. A controlling treatment will manage cancer as a chronic disease by trying to stop the tumor from growing and therefore, improving the patient's quality of life and life expectancy. When the cancer is at an advanced stage and/or cannot be controlled, treatment can be used to ease the symptoms caused by the tumor, this use of treatment is considered as palliative. The most common treatments in patients with cancer are surgery, radiation therapy, chemotherapy, and more recently, immunotherapy.

Surgery is the oldest form of cancer treatment, it acts locally and will physically remove cancer. It works best for solid tumors that are contained in one area, often meaning that the cancer is in its early stages. Furthermore, it can be considered as curative in these cases. However, surgery cannot be an option for leukemia, lymphomas or any cancer that has spread, as it is a local treatment. Another restricting factor can be the location of the tumor. Whether it is near sensitive tissues, vital organs, or major blood vessels, it might be too dangerous to perform a surgery or even inaccessible for any surgical method. Curative surgery will remove the tumor as well as some healthy tissue around it (surgical margins). The lymph nodes neighboring the tumor can also be removed to determine whether the cancer has spread or not and establish if further treatment is needed [26]. Surgery can also be used as a supportive treatment, to debulk the tumor. Debulking means that only a part of the tumor will be removed to reduce its size and make other treatments easier or lower the damage that the tumor is making to another organ. In a preventive goal, an organ can be surgically removed before any cancer has developed. The risks in cancer surgery are the same as for any other surgery and include pain, infection, bleeding and, depending on what was removed during surgery, loss or alteration of organ function [27].

Radiotherapy is mainly used as a local treatment in many different types of cancers including some lymphomas, leukemia, brain cancers, and spinal cord cancers [28]. Furthermore, it can be used to treat metastasis, but only locally. The main operating principle of radiation therapy is based on the capacity of ionizing radiation to kill cells. More precisely, it will attack cells that divide rapidly and struggle to repair their DNA. This especially triggers cancer cells as they divide quickly and cannot repair damage, hence having a higher chance to die as their neighboring healthy cells. Used for a controlling or palliative purpose, radiotherapy will shrink a tumor, hence reducing symptoms caused by the spread of the tumor in neighboring organs [29].

Radiotherapy is divided into two main techniques: external and internal radiation. This means that the ionizing radiation can come from an external beam of γ -rays or X-rays or accelerated particles such as electrons or hadrons, or from a radioactive nuclide placed inside the patient. Internal radiation, more commonly called brachytherapy, is used for cancers located in the head and neck, breast, cervix, prostate, and eye [29]. The main challenge in any radiation technique is to find a balance between deposited dose being high enough to have an effect on cancer cells but not too high that it would affect healthy cells. This problem is addressed in brachytherapy, as the source is very close or even in the tumor, and in external beam radiotherapy (EBRT), with new techniques allowing dose to reach more precisely the target. The side effects will depend on the size of the area treated, the dose used and the type of tissues in the close neighborhood of the target. An important limiting factor to radiation is that every tissue has a tolerance limit to radiation dose [29]. Once reached, the risk of suffering severe side effects becomes dangerously high.

Chemotherapy is a systemic treatment, which means that the drugs travel throughout the whole body. Indicating that it can reach cancerous cells anywhere, even the ones that have metastasized and are far from the primary tumor [30]. Chemotherapy encompasses the use of different drugs that all have a similar functioning, which is to inhibit mitosis or induce DNA damage in a way that it will interfere with cell division as well as damage cells and lead to their death [31]. Different drugs will attack different cell targets, at different times during the cell cycle. In the same way as in radiotherapy, cancer cells are more prone to be affected by chemotherapy because they divide more quickly than healthy cells and cannot repair DNA damage. However, cancer cells can have very different reactions to these drugs, furthermore, they can also build resistance to them. Therefore, to reduce the chances of this happening and to destroy as many cancer cells as possible, several drugs are often used together, one after the other or in combination. The drugs can be delivered in many different ways, some of them are intravenous, oral, injected or even topical [32]. Side effects will affect cells in the bone marrow, the digestive tract or in the hair follicles leading respectively to immunosuppression, mucositis, and alopecia [33].

Immunotherapy is an expanding field in oncology and has significantly changed the cancer treatment landscape and research is still ongoing to expand its application. As its name suggests, immunotherapy will make use of the immune system of the patient to attack cancerous cells. Indeed, cancer cells have antigens that can trigger an immune response. However, cancer cells can be difficult to recognize for the immune system because they start in normal cells [34]. By boosting the immune system, immunotherapy will improve its ability to kill cancer cells [35].

Two main types of immunotherapy are available, the passive and active types [36]. The passive, or "off-the-shelf" treatment, will stimulate the immune response in general, in a non-specific way. For example, checkpoint inhibitors will block checkpoints in the immune system to allow a stronger immune response. The active therapy is, on the other hand, very specific to the type of cancer that is treated or even to the patient. Adoptive cell-based therapies will remove cells from the tumor, change them in the lab to make them stronger, and putting them back in the patient. Cancer vaccines are also of the active type as they will teach the immune system to react to a specific cancer, the same way vaccines are used against viruses [37]. Therefore, immunotherapy is best suited for cancers showing special characteristics either for easier identification or because of their link with the immune system [35]. Treatment duration and side effects can vary greatly depending on the immunotherapy administered to the patient. However, the side effects will be caused by the overreaction of the immune system, causing for example rashes and itching of the skin, gastrointestinal problems and joints inflammation.

In many cases, the treatment types are paired for a more efficient handling of the cancer. The structure of such a treatment is as follows [25]:

- Neoadjuvant treatment: secondary therapy used before the primary treatment to make it easier.
- Primary treatment: main therapy that aims to completely remove cancer and kill all cancer cells.
- Adjuvant treatment: secondary therapy that aims to kill any remaining cancer cell after primary treatment, hence reducing the chances of cancer recurrence.

It is also interesting to note that certain chemotherapy drugs, when used during radiotherapy, will enhance the effects of radiation [38].

1.2.3 Radiation therapy

As explained in the previous paragraph, there are two main radiation techniques that differentiate themselves on the origin of the radiation: from the inside of the body or from the outside. The advantage of having different techniques lies in having different treatment approaches for the variety of cancers. In external beam radiation, a high energy beam is aimed at the tumor from outside the body. The beam can be made of different particles, like photons (X-rays or γ -rays), ions, or electrons. The interesting difference between these particles is their interaction with tissues when they reach the body. Photons will penetrate deep in the body and scatter along their way while protons will not scatter as much, allowing them to deposit the majority of their energy at the exact place they stop (calculated to be the tumor). Electrons, at the energies typically used in radiation therapy, cannot penetrate deeply in the body and will therefore be used only for tumors at the surface of the skin [39]. To create the beam, the particles need to be accelerated, while photons are produced by directing a high energy electron beam onto a metal target. A linear accelerator (LINAC) will be used to accelerate electrons and other relatively lightweight particles, for heavier particles synchrotrons or (syncro)-cyclotrons are preferred.

In order to give the healthy cells some time to recover from the radiation, the treatment is organized in fractions. This also allows the dose to the target to be higher. The fractions usually take place 5 days a week, using the weekend as recovery time [40].

Brachytherapy is a type of internal radiation therapy, where a radioactive source is placed inside or near the tumor. There are many application techniques of this type of treatment, and they vary along three main parameters, where the device is put, for how long, and what source is used. The implant takes the form of seeds, pellets, capsules, or tubes and contain a sealed radiation source. They are usually put in place with the help of a catheter or an applicator. It can either be interstitial, which means directly into the tumor, or intracavity, indicating they are put within a natural body cavity, or a cavity created by a surgery, or even episcleral, which typically means it is attached to the eye [41]. These implants can be of low dose rate and will be kept for several days. High-dose rate implants can only be kept inside the body for a few minutes. There are also permanent implants that will never be removed because the radiation will get weaker and will almost completely go away [41]. Sources mostly produce γ -rays, which have the same effect on cancer cells as X-rays, and the most used are Iridium-192, Iodine-125 and Caesium-131 [42]. The choice of these different treatment parameters mostly depends on the type of cancer, its location, the patient's health, and treatment history. Brachytherapy is most popular for cancers like prostate, cervical, uterine, vaginal, eye, breast, or liver cancer [43]. It is important to note that for implants that can stay in, whether it is for days or indefinitely, the radiation safety for others must be considered as the patient becomes a radioactive source [43].

1.2.4 Radiobiology

The human body is made of eukaryotic cells, where the nucleus holds the genetic information, the DNA. There are two main categories of cells, somatic and germ cells, the latter will evolve to be a reproductive cell while all of the other cells in the body are somatic. Both cell categories propagate through a division process; called meiosis for germ cells and mitosis for somatic cells. Both processes are divided in different time periods, as illustrated in Figure 1.6, it includes the division period (M phase), the DNA synthesis (S phase) which are separated by two gap phases: G1 and G2.

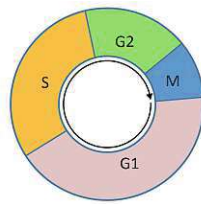


Figure 1.6: Cell cycle [44]

The first factor influencing the radiosensitivity of the cells is the phase they're in at the time of damage. Radiosensitivity is increased when the cell is in the division phase and in the G2 phase. On the contrary, cells are more resistant when they are in the late S phase [45].

Cells exist in the body in different states such as stem cells, transit cells and mature cells. Stem cells are cells that will self-perpetuate and produce cells for differentiated cell populations. Differentiated cells are specialized cells performing specific functions in the body. Transient cells are in the process of maturing and becoming differentiated these populations. Mature cells, however, are fully differentiated and will not divide anymore. As the state of a cell has an impact on their dividing rate, it has an indirect effect on their radiosensitivity [46].

Irradiated cells can react in different ways [47]:

- No effect
- Delay in division
- Apoptosis, cell death before it can divide
- Reproductive failure, where the cell dies as it attempts to divide

The radiation damage can also be classified as either lethal, hence irreversible, or sub-lethal, which can be repaired in hours. Malignant cells have a shorter cell cycle than healthy ones and their abilities to repair damage are impaired, hence making them very sensitive to reproductive failure [47]. Healthy cells have the time to repair the damage made before they attempt the subsequent mitosis.

Bergonié & Tribondeau’s law state that “radiosensitivity of a biological tissue is directly proportional to the mitotic activity and inversely proportional to the degree of differentiation of its cells” [48]. This is because, as explained above, cells are more sensitive when they are in M and G2 phases, hence a cell that has a high reproductive rate has a higher probability of being in these phases at the time of irradiation. Moreover, a less differentiated cell will divide faster than more differentiated cells, hence they will also have a higher chance of being in a sensitive phase of mitosis. This means that cells are more radiosensitive when they have an increased rate of cell division, a low level of cell specialization, and an increased length of time where they are actively proliferating [49].

Another factor that has a big impact on radiosensitivity that was not clearly stated in Bergonié & Tribondeau’s law but is indirectly linked to their observation is the presence of oxygen. The oxygen effect is due to the fact that O_2 reacts with free radicals (induced by ionizing radiation) and produces very reactive species that generate irreparable damage [45]. The presence of oxygen in the cell can be due to a highly active metabolism, which is usually the case for cells with a high division rate. This means that cells are more radiosensitive when they have a higher metabolic rate, an increased oxygenation and are well nourished. Differences in radiosensitivity of cells leads to differences in radiosensitivity of tissues.

Cell survival curves (Figure 1.7) are used to describe the surviving fraction of cells and absorbed dose. Different models are used to describe the survival of cells depending on the radiation. The linear-quadratic model allows to describe cells’ reactions to sparsely ionizing radiation and shows an initial slope followed by a shoulder region and becomes nearly straight at high doses.

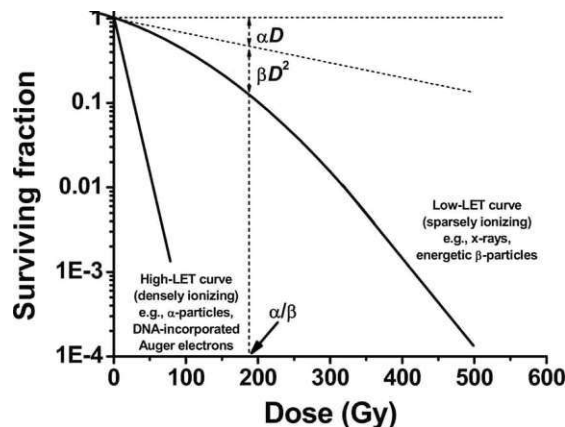


Figure 1.7: Cell survival curve [50]

The model describes the fraction of cells S surviving a dose D as:

$$S(D) = e^{-\alpha D - \beta D^2} \quad (1.2.1)$$

α : constant describing the initial slope of the cell's survival curve

β : smaller constant describing the quadratic component of cell killing

This model assumes two death mechanisms: a single lethal event, and the accumulation of sublethal damages that leads to cell death. Hence, the ratio α/β gives the dose at which both mechanisms are equal [47].

The factors that can be altered to decrease healthy cells' radiosensitivity are, on one hand aiming to decrease the oxygen effect and on the other hand, aiming to increase the chance of damage repair. The first goal can be reached by removing oxygen to put the cells in a hypoxic state or by adding chemical radical scavengers that will convert radicals into non-radical products [47, 51]. The second goal is achieved by the fractionation of the treatment. For the same radiation dose, if the radiation is delivered at a lower dose rate, it will kill less healthy cells. This is because the time between the fractions allows for cells to repair sublethal damages that occurred during irradiation. This sends the constant β -accounting for deaths coming later in time- towards zero [45].

Dividing dose into multiple fractions is based on the "4Rs" theory [52], it:

- Spares normal tissues through:
 - Repair of sublethal damage between fractions
 - Repopulation: rapid proliferation of surviving tissue after cell-killing induced radiation
- Increases tumor damage through:
 - Reoxygenation: due to reduced demand from dying tumor cells
 - Redistribution: cells tend to pile up at a G2 checkpoint after being exposed to radiation, making them more sensitive in subsequent radiation

As mentioned when introducing cell survival curves, the type of radiation has a role to play in the cells' response to it. To define the quality of an ionizing radiation beam, the linear energy transfer (LET) value is used. This value describes the density of energy deposition in a material, and more precisely the linear rate of energy absorption by the absorbing medium as the charged particle traverses it. In the context of external beam radiation therapy, the secondary charged particles produced by X-rays and γ -rays are low LET radiations so they deposit only a small amount of energy along their path in the body [45]. Higher LET radiations will mean higher abilities to perpetrate biological damage. The quantification of this observation is made through the relative biological effectiveness (RBE), which is a ratio between a dose of standard radiation known to produce a given biological effect, and a dose of a test radiation that produces the same biological effect [45].

RBE can vary according to various parameters such as the type of radiation, the target tissue, the biological effect in question, the dose rate, and its fractionation. Hence, the therapeutic use of RBE comes in when the RBE value is higher for healthy tissues than for cancerous ones.

The overall intended outcome from radiotherapy is cancerous cell damage, or death. As explained, it can also be caused on healthy cells that are not the target of the treatment, although it is avoided as much as possible. The damage to healthy cells creates side effects, which vary in severity, causes, and delay. First factor differentiating side effects is determined by the dose and the time when the side effects appear.

An acute side effect will show soon after a short time exposure to a high dose radiation. High dose radiation kill cells and the effects can vary greatly, going from vomiting to death. On the contrary, a chronic side effect is delayed and takes place after long term irradiation to low dose. Low dose irradiation only causes damage to cells which explains that the effect can only be observed later in time.

Chronic side effects can again be separated in two types: somatic and genetic. Genetic side effects will only be suffered by the offspring of the person that was irradiated. Somatic side effects, on the other hand, will be suffered by the person during their lifetime. One of the most common somatic late effects is carcinogenesis, or in other words, radiation-induced cancer.

The last categories used to differentiate the side effects relates to threshold dose. In deterministic effects, which are mostly acute but can be chronic, the severity of the symptoms increases with the dose. In stochastic effects, which are mostly chronic but can be acute, the probability of occurrence increases with the dose. However, the severity does not depend on the dose, it is therefore said that there are no threshold doses for stochastic effects [47].

One of the most frequently discussed side effect is radiation-induced cancer because of its counterintuitivity, it is however not the only late side effect of a radiotherapy treatment. Radiation can damage tissues and induce fibrosis, which creates permanent scar tissue instead of parenchymal tissue [53]. This causes the tissues to be less flexible, which can lead to vascular constriction and nerve compression [54]. The lymphatic system can also be damaged and cause swelling and obstructive symptoms [55]. When blood vessels are damaged by radiation; thrombotic, inflammatory and fibrogenic complications can take place [56]. Radiation necrosis can also be caused by damaged blood vessels, reducing blood supply to healthy tissue and causing it to die by ischemia [57]. Nerves are radiosensitive, and are hence prone to damage. Damage takes place in three phases: (1) micro-vascular injury, (2) capillary damage, (3) nerve demyelination [58]. Bones can also be victim of radiation damage although they are not very radiosensitive, the damage can cause weakening of the bones, osteoporosis, or even osteonecrosis [59].

In the context of pelvic radiation, the organs suffering of these damages are the bladder, the rectum, the bowel and the reproductive organs. The effects to the bladder can be an overactive functioning due to the shrinking of the organ, and hence reduced urine quantity holding capacity, because of damage of the tissue making it less flexible. Incontinence can happen if the pelvic floor muscles and the urethral sphincter were weakened. On the contrary, another side effect can be urine retention caused by damage to the nerves near the bladder which will affect the muscles' work, making it impossible to empty the bladder completely. Other side effects can be pain and burning when passing urine as well as haemeturia (blood in urine) [60]. For the bowel, atrophy of the organ, fibrosis and vascular changes can cause intestinal problems like pain, diarrhea, steatorrhea and bleeding which can lead to malabsorption of nutriments like vitamin B12 [61]. The effects to the rectum are increased stool frequency, urgency, rectal bleeding, pain, as well as variable degrees of incontinence and strictures [62]. Infertility can be a side effect to both male and female reproductive systems. However, women can also suffer from early menopause, vaginal bleeding, vaginal dryness, fibrosis of the vaginal tissues, and vagina stenosis [55]. Nerve damage taking place because of pelvic irradiation can cause tingling, weakness, or loss of sensation in one or both legs [63].

1.3 Radiation therapy process

1.3.1 CT scan

Treatment plans are based on CT scans in treatment position, it is therefore important to know what this data shows. A CT scan is made of an X-ray tube and a row of detectors rotating around the patient, allowing to take measurements at multiple angles and positions and can be reconstructed as slices afterwards. Although it uses an X-ray beam like in EBRT, for imaging purposes, the energies of the X-rays are lower as in therapy and are set around 20-150 keV, where photoelectric and Compton effects rule the interaction between the X-rays and matter [64]. The underlying principle of CT scan is to measure the intensity of the X-ray beam after it has crossed different tissues. Their different capacities to attenuate X-rays are visually translated with different shades of grey, which can be modified with windowing. A high absorption of X-rays translates most of the time a high atomic number, hence a high physical density as well as a high electron density [65]. The shade of grey showing at the exit of the tissues represents the proportional sum of the attenuation coefficients of all the tissues the beam has traversed [64]. The Hounsfield unit (HU) offers a quantitative interpretation of the different shades of grey, and links it to the attenuation coefficients in the form of a linear transformation of attenuation coefficient, based on the arbitrarily-assigned radiodensities of air and pure water.

$$HU = 1000 \frac{\mu - \mu_{water}}{\mu_{water} - \mu_{air}} \quad (1.3.1)$$

with $\mu_{air} = -1000$, $\mu_{water} = 0$ and μ , the average linear attenuation coefficient of the voxel [66].

Moreover, CT scans gives a good contrast for tissues that have "extreme" densities, like bones showing very bright or lungs filled with air showing very dark. However, the contrast between different organs made of soft tissues can be very light and make it difficult to differentiate the organs.

1.3.2 Treatment planning

Treatment planning consists of the customization of therapy and delivery according to the patient's tumor burden and anatomy. The planning of the treatment involves the choice of the technique used, the dose administered, the duration of the treatment, as well as its fractionation. The principal factors influencing these decisions are the localization, size, density, and sensitivity of the tumor [67]. Here, the discussed treatment planning refers to external beam radiation therapies. The shape and angles of the beam will have to be established after analysis of the anatomic location of the target site via a simulation made on the latest CT scans [68].

In order to assure that the patient will be in the same position from simulation to treatment, as well as from fraction to fraction, but also assure that they will not move during the treatment, immobilization devices are used as part of the patient setup. These devices include masking tape, velcro belts, elastic bonds, or even sharp fixation systems [69]. The patient position is determined with the help of a scout image, which is a survey of the region of interest that will also be used to select the dedicated image acquisition area [47].

The patient data retrieved from the CT scan are the external shape of the patient, as well as the adjacent areas, like the couch, to account for scattered radiation. However, MR imaging plays an increasing role in treatment planning, as it offers a better soft tissue contrast than CT scans. MR based treatment planning has however some issues such as the physical dimensions of the machine reducing the position possibilities as well as the choice of immobilization devices, electron density is also lacking, and geometrical artifacts and distortions are still present in this imaging device [70]. Therefore, when used for treatment planning, MR images should be registered or fused with CT data to combine information.

It is necessary to define the volumes of interest by delineating the relevant organs and tissues.

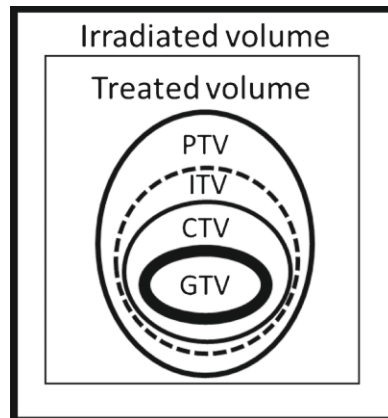


Figure 1.8: GTV, CTV, PTV, and ITV schematic definitions (ICRU Report 62) [71]

For the tumor's delineation, different volumes are defined for different uses (Figure 1.8) [72]. The gross tumor volume (GTV) will highlight the visible extent of the tumor. Around the target, the OARs surrounding the tumor are delineated. Then, the GTV will be extended to delineate the real target, which is called the clinical target volume (CTV). It is defined as the true target because, compared to GTV, it includes margins surrounding the visible tumor's boundaries which might contain cancerous cells and are part of the volume to be eliminated for safety. Now the CTV is expanded to the planning volume target (PTV), which will account for technical set up margins. It should take all possible geometrical variations into consideration to make sure that the CTV will actually receive the prescribed dose [73]. The PTV takes all uncertainties and dose variations into account as it includes the internal margin as well as an additional margin for set up uncertainties, machine tolerances and intra-treatment variations. More precisely, the internal target volume (ITV) is defined as the CTV and the internal margin, which accounts for organ motion [72]. Then, the PTV consists of the sum of the ITV and the external margin.

Furthermore, it can be stated that the PTV considers systematic and random errors. The treatment preparation creates systematic errors such as setup errors, organ motion during planning CT, delineation errors, or equipment calibration errors. While the treatment execution introduces random errors which are due to inter- and intra-fraction changes. These different volumes are either volume defined or geometric concepts [74]. Indeed, the GTV, the CTV and even the OAR, have an anatomical basis to their delineation, hence it is a result of a medical judgment. However, the PTV, as well as other volumes like the ITV or the planning organ-at-risk volume (PRV), are constructed volumes to ensure the correct dose delivery to the CTV and OARs. These volumes consist only of the addition of the correct margins for the respective indication and patient. Moreover, the PTV depends on the irradiation technique while the CTV does not.

Margins are essential to radiotherapy to assure safety of the dose delivery (assure that the target is in the treated field 90% to 95% of the time [75]). It is however important to remember that, as margins are three dimensional, a small margin increase translates in a large volume increase. The dose delivered to the target should be as homogeneous as possible, although some heterogeneity is accepted due to technical reasons. The ICRU report 50 recommends a target dose uniformity within +7% and -5% relative to the dose delivered to a well defined prescription point within the target [76].

To visualize treatment beam axis and outlined structures for a virtual treatment simulation, a cone beam CT is used (CBCT). The anatomy is then compared with the planning CT, and modifications can be made if necessary. Such imaging method provides volumetric images and allows a precise localization of the target area and hence, an accurate dose calculation. Moreover, as it is mounted on the LINAC gantry, it enables beam adjustments based on real-time images. This is part of the optimization process in the virtual treatment simulation, as the radiotherapy technologists (RTTs) or the medical physicists will be trying to ensure the highest effect on the tumor while excluding the healthy tissues and organs in the vicinity of the target dose. In the most common cases, the target dose is between 40 and 70 Gy [67]. It could however be tuned accordingly to the patient's specific reaction to radiation. This prescription is made by the radiation oncologist and will vary also on the aim of the treatment, whether it is curative or palliative as well as whether it is primary or adjuvant. Depending on the sensitivity of the OARs and their position to the high dose area, it can be necessary to modify the beam arrangement or even the dose to spare them [77].

Every treatment plan has to be evaluated in order to assess the quality of the plan, more precisely to assure that the calculated dose distribution of the dose treatment plan complies with the clinical goals of the treatment [78]. Isodose distribution is one of the tools used to check that the coverage of the target as well as the protection of the surrounding tissues. Another step is patient QA (PSQA), which can be done by recalculation of the treatment plan using a different dose calculation algorithm and/or dose measurements of the treatment plan calculated on the geometry of a dedicated QA phantom.

As explained in above section (1.2.4), dose delivered in fractions gives better results as it allows healthy cells to recover from radiation damage while providing maximum tumor control. Indeed, the dose will be administered in daily fractions (5 times a week) over several weeks. The dose given in one fraction ranges from 2 Gy up to 36 Gy, depending on the fractionation. Hyperfractionation allows small doses as the treatment is given twice a day over the same total treatment duration. On the other hand, hypofractionation delivers higher doses per fraction but there are less fractions, and the treatment is shorter. There is also accelerated fractionation, which uses smaller doses multiple times a day and on a shorter period [79].

This description of the treatment planning process, highlights the interdisciplinary nature of radiotherapy, and how important communication, standardization and harmonization are essential for a proper functioning. The ICRU reports serve, to a certain extent, this purpose.

1.3.3 AI segmentation

Segmentation is a key component of the radiotherapy workflow. More precisely it is crucial in registration, whether it is to be used as controlling structure or as a quality assurance metric, as well as in treatment planning for the target or organs at risk (OARs) definition. Tools currently used in clinics such as intensity analysis, shape modeling, thresholding, and region growing already make use of deep learning [80]. However, they leave an important role to manual editing, which has to be carried out by experts. Although it is a validated and widely used process, it has three main disadvantages [81]. Firstly, it is very time consuming and significantly contributes to the treatment planning duration. Secondly, although there are some guidelines on how segmentation should be performed, in the end, there is no "ground-truth" of what a perfect good segmentation should look like. Thirdly, as manual input is necessary there is a high inter- and even intra-observer variability, which makes this process practically impossible to reproduce. The two last arguments also make it difficult for any multi-institutional comparison.

That is when AI-powered segmentation comes into play. Here, convolutional neural networks (CNN) are used. They have the ability to extract low-level image features through hidden layers and are developed using retrospective peer-reviewed treatment contours [81]. They offer a real difference in segmentation as they can handle a wider variety of complex anatomical structures and variations (Figure 1.9). Moreover, deep convolutional neural networks (DCNN) also learn independently a hierarchical representation of the input data, but need however a large input data to do so effectively.

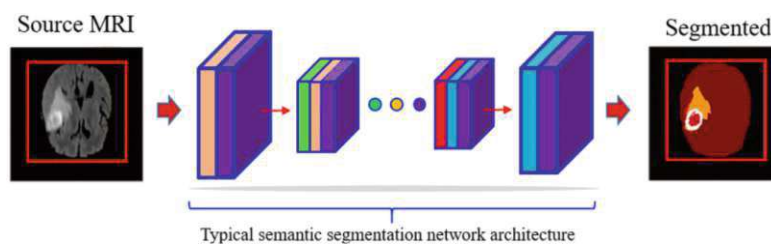


Figure 1.9: Schematic representation of CNN segmentation [82]

The CNNs used in medical practice are adapted from the ones used in conventional image segmentation, but the nature of medical data complicates the adaptation. These difficulties consist of the scarce training data, the high number of modalities, the 3D nature of tomographic imaging, and the domain shifts between medical practices or protocols [83].

For medical segmentations, the most common CNN architecture used is U-Net [81]. These models have an encoder-decoder structure, each made of four levels, giving it a U shape (visible on Figure 1.10), which it is named after. The encoder uses convolutional layers and max pooling as a contracting path, where it reduces the spatial information (size of input halves with each level) and increases the feature information (number of channels doubles with each level). This part of the model is responsible for identifying the relevant features in the input image, but in image segmentation, the location of the features play an important role. Therefore, the expansive path (the decoder) will work on locating the features as well as decoding the encoded data.

The decoder has the same structure as the encoder for each level, but in order to up-sample the image, it uses transposed convolution, also called deconvolution, instead of convolution layers. To retrieve spatial information lost in the encoding, the decoder uses skip connections ("copy and crop" gray arrows on Figure 1.10), which give access to information that do not go through all of the convolution layers.

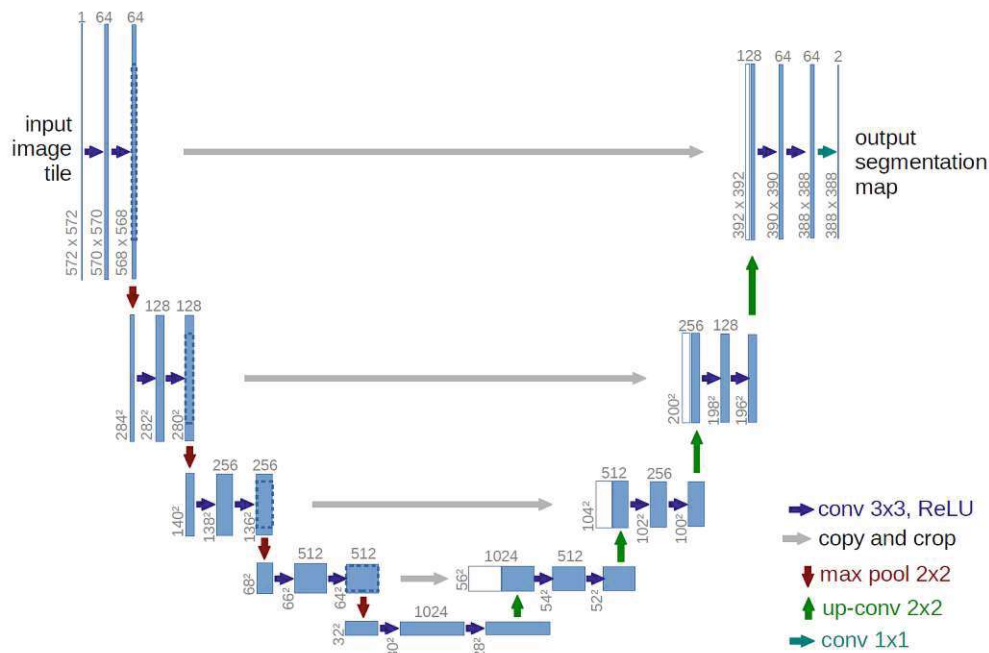


Figure 1.10: U-Net architecture [84]

AI segmentation could accelerate the treatment process, as well as increase its quality and reproducibility. Introducing it into clinical workflow could then reduce effort and bias, and offer efficiency and consistency, which would be a notable advancement in radiotherapy patient care. It has indeed been proven to outperform physicians in similarity metrics as well as time [81, 85].

It should however still further demonstrate robustness when presented to different patient populations, diversity in patient anatomies, and changing tumor treatments and protocols. Before being implemented into clinics, these models should assure adaptability and flexibility to structures with significant variability. Moreover, it should be able to manage the differences between the training data and the actual patients, which can arise from different demographic characteristics or the choices of contouring guidelines. Although the progress in computing power in the last years pushes beyond the earlier limitations of performance of these models, it also translates a huge dependence on new technology which reduces the accessibility to the tool [86].

Implementing these models into clinics would also be very challenging on the user side. Firstly because, although it is an automated process, the results will be used in human conducted parts of the treatment planning and verifications will always be performed by a clinician. Explainability in AI models is crucial when they are part of a decision making process. Users should also deeply understand how to operate the tool, as well as its intended use and scope [87]. Correct interpretation and verification of the results are essential to the patient's safety. Hence education of the workforce, as well as implementation and utilization guidelines are necessary for an effective and competent use of AI models in clinics [88]. Another dimension of this transparency is to ask the algorithm provider for details about the data used for training [89].

The use of AI in radiation oncology can cause changes in the work and required skills of professionals in the domain such as dosimetrists, physicists, and radiation oncologists, hence their tasks might have to be refocused [90].

1.3.4 Re-irradiation

Re-irradiation is a new course of treatment, either to a previously irradiated volume or where the cumulative dose raises concerns of toxicity [91]. It takes place in patients with recurrent cancer, metastatic cancer, or new malignancies following an initial course of radiotherapy. There is an increasing interest and use of re-irradiation, which are probably caused by an increase in the long-term cancer survivors, earlier detection, better staging, an improvement in treatment modalities like precision in planning and delivery, and the improvement of multidisciplinary approaches.

However, before administering a re-irradiation treatment, it should be made sure that the patient can clinically tolerate a second irradiation, that the information about the first irradiation is sufficient to plan a safe second radiation and that the technique used for re-irradiation is the most adequate [92]. The factors from the first radiation that will be looked at are: the dose that was prescribed, the volume irradiated, the chosen fractionation, the time between the two treatments, and the type of organs that were the targets or OAR [93].

Indeed, a large targeted volume will be more problematic, as well as a high dose, but it is also very dependent on the irradiated area, whether the neighboring tissues and organs are radiosensitive or not [94]. Tissues also have different recovery factors, meaning that the cells could have totally recovered from the first irradiation. For example, rapidly proliferating tissues will tolerate re-irradiation to almost full dose as they recover well from the initial radiation. Nevertheless, not only is this factor very tissue-specific, but it is also very patient-specific and not very well known [93].

However, the main concern in a re-irradiation treatment is identifying how much overlap actually exists between the two treatments in order to measure the dose accumulation in the treated area. For a realistic treatment planning, biologically equivalent doses should be calculated to account for the delivered dose, and this voxel-by-voxel [95].

There are multiple late side effects that can be induced by radiation, and more importantly, their probability of occurring increases with dose. For this reason, the treatment planning in the case of a re-irradiation should not be handled as if it was a first-time treatment. Therefore, as explained above, the dose already received by the tissue should be considered. However, patients' anatomies change over time. These already occur in between fractions and are cared for in the IGRT technique. Furthermore, these changes are even more important in re-irradiation situations, as years have gone by. These anatomic changes lead to the impossibility of simply superposing the scans of the two treatments. This translates the need of changes of the primary scan to match the present one, in order to take the primary dose into account in the current treatment plan, only then will the overlap be realistic.

1.3.5 Registration

The anatomical changes taking place between the two treatments can be of different types and causes, they can result from surgery, changes in habitus, patient positioning, organ filling and internal motion. These changes translate in the datasets to variations in position and location, as well as in size. In the context of this work, registration is used for re-irradiation, but it is also used between different modalities (e.g. CT-CBCT, CT-MR), or between CTs in a different context such as inter-fraction images. The process used to superpose the two scans is called image registration:

"The process of spatially aligning two or more image datasets of the same scene taken at different times, from different viewpoints, and/or by different sensors."[96]

The two types of registrations used in re-irradiation are rigid image registration (RIR) and deformable image reformation (DIR). As its name suggests, RIR only allows rigid transformations of the image set, hence translations and rotations. This can improve positional problems but cannot help size changes as it preserves the relative distance between every pair of points. In contrast, DIR is a nonlinear process that can achieve stretching or shrinking transformations.

It was showed in multiple studies that DIR give better results than RIR when used correctly [97–99]. On the representation side, RIR transformations are described by a matrix while a displacement vector field is used in DIR.

Any basic algorithm will try to optimize transformation parameters to find a registration that optimizes a similarity metric. A regularization term is typically included in the similarity metric to allow only transformations that are judged desirable and physically plausible. Different matching criteria can be used in a DIR algorithm. For example, the criterion could be intensity-based and use intensity to optimize the registration. This will work better for datasets with clear features and high contrast. Landmarks and/or structures that are defined in both image sets can be used to help the optimization process. Another criterion can be biomechanical properties, which means that modeled physical properties of the tissues are used. These properties are modeled by finite element methods (FEM) [100].

1.3.6 Dose accumulation

Dose summation consists of the addition of doses. However, when anatomical changes are accounted for between the two dose plans, dose must be accumulated rather than just summed. Dose accumulation refers to the process of summing a mapped dose with another dose. Every dose plan is linked to a CT scan on which it is implemented. Once the registration, either RIR or DIR, is performed between the CTs, the dose of the first treatment can be mapped to the second one using the registration transform (Figure 1.11).

It is assumed that the information attached to the images changed in the same way as the anatomical changes, hence making the use of DIR transformation to warp dose valid (Figure 1.11b). The importance of the precision and accuracy of a DIR is emphasized in re-irradiation as the dose accumulation will be used as input of a process for planning or delivery [101].

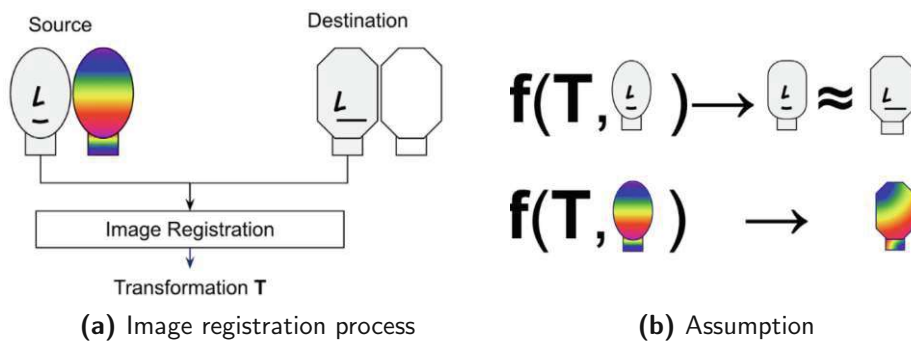


Figure 1.11: Schematic representation the use of image registration to map dose distribution [101]

Re-irradiation is in fact the intended use of dose accumulation that has the highest impact on the patient's health and safety because it is incorporated in the patient's treatment workflow (Figure 1.12). The effect of a flawed registration can be relapse, because of a treatment not strong enough, or severe side effects, because of a treatment too strong for the patient.

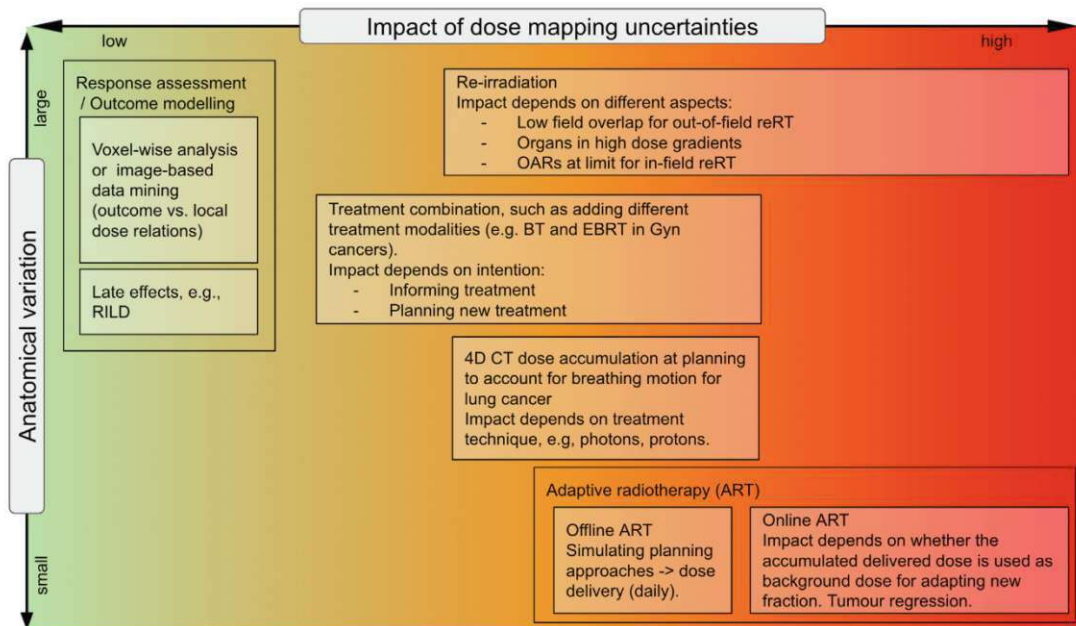


Figure 1.12: Current landscape of dose mapping use cases [101]

Notably, dose mapping uncertainties will be introduced because of uncertainties in the registration. However, as dose distributions are highly heterogeneous, the uncertainties in dose mapping will be present particularly in regions where high dose gradients are to be found, which is mostly in the region close to the target [101]. Indeed, uncertainties in steeper dose gradients regions cause stronger dose variations. Moreover, the uncertainties in the deformation vector field (DVF) are spatially correlated, hence, the theoretical impact of registration uncertainties on the mapped dose distribution can be quantified based on the distance to dose difference [102].

As there is no "ground truth" to be judged upon, a proper registration holds in the combination of two aspects: the degree of anatomical variations and the impact of dose mapping variations. Furthermore, a geometrical accurate DIR, which would display a good anatomical match does not assure an accurate dosimetric registration, as it depends on the spatial location of the DVF errors and the dose gradients [101].

The main factor affecting the quality of a registration is anatomical variation. The cases of re-irradiation show the highest the degree of anatomical intra-patient variations because of the time passed between the two scans to be registered (Figure 1.13). However, other factors can also influence a registration such as imaging artifacts, distortion, lack of contrast, or noise [103].

Although there is no standards to qualify a good registration or a good dose mapping, four steps can be used to perform a form of quality assurance (QA) [101]. The first step would be to ensure that the appropriate dose mapping/accumulation (DMA) workflow is in place. The second and third steps are QA checks of both the DIR and DMA results. The final step would be to review the impact that DMA uncertainties could have on clinical application. Another QA for dose mapping stands in the comparison of the dose to the landmark from both the original and mapped dose distribution [104]. According to *Murr et al.*[101], DMA uncertainties related to the registration can be considered as first order effects, there are however also second order effects which include issues such as energy/mass transfer, biological uncertainties, resampling, or even interpolation. Biological uncertainties in the context of dose accumulation can refer to α/β values for the EQD_2 or BED, or to the validity of the LQ model. Actually, the final aim of dose accumulation is to quantify the radiobiological effect of the treatment. For example, replacing the LQ model with EQD_d is a question which can have a big impact on biological dose accumulation [105].

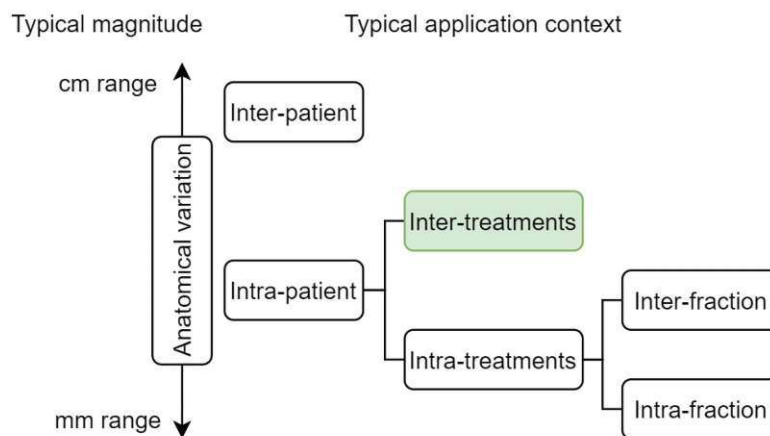


Figure 1.13: Illustration of the expected anatomical variations, re-irradiation suffers from inter-treatments variations [101]

1.4 Aim of the thesis

Thanks to the development of radiotherapy techniques and the increasing number of acquired images, re-irradiation has been extensively adopted in clinical processes. However, no agreement, or standards have been found in the radiotherapy community, whether is it to assure the patient's safety with an optimal use of image registration, to quantify uncertainties and their radiobiologic effects, or to classify and report on the topic.

As none of the available deformable image registration strategies have been proven superior to the others, the aim of this thesis is to calculate the best estimate of dose deformation by combining different DIR strategies, and to derive dosimetric uncertainties. By assessing the different registration performances and estimating geometric uncertainties, an evaluation of the relationship between geometric and dosimetric uncertainties will be possible. The identification anatomical regions sensitive to registration and other factors causing dosimetric uncertainties are also an important part of the strategies' review.

Segmentation is an essential part in treatment planning, but also in image registration and the evaluation of the latter. Hence, in addition to the primary focus, a comparison between manual and AI-driven segmentation will be conducted.

The thesis can be summarized in four goals:

1. The quantitative and qualitative evaluation and comparison of two registration algorithms and their different parameters
2. The deformation of dose using these registrations and the identification of the challenging regions in the context of re-irradiation
3. The calculation of geometric and dosimetric uncertainties in dose accumulation
4. The comparison of manual and automated segmentation

2 Material and Methods

2.1 Patient cohort

All patient data analyzed in this project was part of the ReCare trial and was therefore selected to meet all criteria of re-irradiation. When made available, the data was anonymized and regions of interest (ROI) were manually delineated by a radiation oncologist. Within the framework of the clinical trial, the time between the two cancer treatments must be of at least one year, but can go up to multiple years. Each of the ten cases treated were men, suffering from a new cancer or a recurrence, needing a second radiation treatment in the pelvic region. The most frequent irradiation targets in this patient cohort were the prostate (bed), multiple lymph nodes and the sacrum bone. The dataset of a patient included two CT scans of similar qualities, the two treatment plans associated (first and second treatments), the year when they were conducted as well as the delineation of all ROIs in both scans.

For the analysis of the pelvic area, ten organs were selected to be analyzed for every patient (Table 2.1). The most evident criteria to draw up the list of organs was that they should be delineated in all patients. It was also decided that the ureters would not be considered in the analysis due to their size, and variability in position. The last ruling was made about the sacral plexus, that can be considered as one unit or as a left and a right one. As some dose distributions were asymmetrical, it was decided to consider them as two distinct organs.

Organ
Left kidney
Right kidney
Bowel
Cauda equina
Left lumbar plexus
Right lumbar plexus
Rectum
Bladder
Urethra
Anal canal

Table 2.1: List of analyzed organs for the pelvic region

2.2 RayStation

2.2.1 Treatment planning system

The principal treatment planning system (TPS) engaged in this work was RayStation (Raysearch Laboratories AB, Stockholm, Sweden), implemented in the Department of Radiation Oncology of the Medical University of Vienna/General Hospital of Vienna. A TPS provides a set of computerized tools allowing professionals to create and visualize radiotherapy treatments. RayStation offers adaptive therapy and dose tracking, which are of special interest in re-irradiation. Additionally, RayStation can handle different types of image registration as well as visualization. RIR can be performed manually or with automatic parameters, and two different DIR algorithms are available.

Segmented ROIs are particularly relevant in radiation therapy for registration, dose prescription, beam optimization, and treatment evaluation. RayStation provides different tools to handle them, such as copying, mapping, or performing other algebraic operations. Statistics can also be derived from these structures, whether it is similarity metrics, dimensions, or dose statistics. These numbers can be retrieved via Python scripting directly in RayStation.

Treatment adaptation also includes dose accumulation. Hence, dose plans can be summed or deformed in the "Plan Evaluation" part of the system. Furthermore, RayStation is able to import DICOM data, image plans, structure sets, previous dose treatments, and dose computed in a different TPS.

2.2.2 Deformable registration algorithm

The algorithm used for deformable registration in RayStation is the ANAtomically CONstrained Deformation Algorithm (ANACONDA). This hybrid algorithm can use image information and add boundary conditions computed from controlling structures to drive its deformation processes. In other words, it can use both intensities and delineated contours to drive the registration. The controlling structures usually are anatomical structures called regions of interest (ROI). However, it can also be run with only image information or only controlling structures. In this algorithm, the registration problem is formulated as a non-linear optimization problem where the function is the weighted sum of three non-linear terms:

- Image similarity: measured through the correlation coefficient
- Grid regularization term: designed to keep the deformed image grid smooth and invertible
- Penalty term: added when controlling structures are used, in order to deform the selected structure in reference to corresponding structure in target image (contour regularization & contour matching)

2.3 3D Slicer

3D Slicer is an open source software used for visualization and analysis of medical image datasets. It allows users to handle DICOM data, as well as read and write other formats, visualize in 2D and to perform volume renderings, or carry out rigid and deformable registrations. Slicer is fully research-oriented, and therefore not intended for clinical use or authorization by any regulatory authority. This approach offers transparency, robustness, and reliability as it is easily inspectable and testable, which is not granted in commercial software.

Another useful characteristic of Slicer is its modularity. It allows the creation of modules tailored to particular tasks with minimal impact on other developers or users. It is an ingenious strategy for systems that develop quickly (like medical imaging) and allows different development styles, timetables, and licensing structures between modules. It can also be downloaded online and works on major operating systems.

2.3.1 Elastix

Elastix is an open-source image registration toolbox, that can be used as an extension module in 3D Slicer. It is built upon the Insight Segmentation and Registration Toolkit (ITK) and has a modular structure (Figure 2.1).

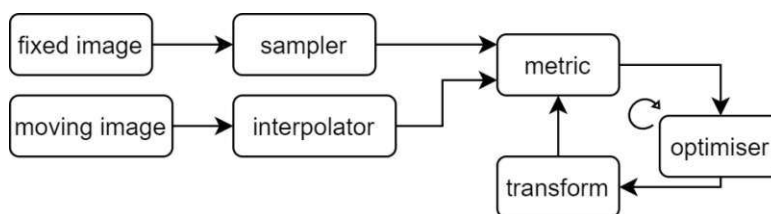


Figure 2.1: Basic modules of Elastix registration [106]

Registration algorithms are usually formulated as optimization problems: trying to have the best metric values while having geometric and time limitations. Hence the optimizer module adjusts the parameters of the transform in order to get a better metric value. The metric module is a mathematical function giving a quantitative criterion to be optimized. The type of metric can be changed depending on the context. The sampler is used to select voxels for the metric module, and the interpolator ensure the correctness of the computed metric values after registration.

The transformation module establishes a correspondence between moving and fixed image for every pixel. In Elastix, the allowable transformations should be defined. The transformation types available are: translation, rigid (translation & rotation), isotropic scaling, affine (scaling & shear), B-splines, and thin-plate splines. They are designed for intensity-based registration of medical images.

In its generic version available in Slicer, the optimizer used is a gradient descent optimizer with an adaptive gain, and the metric is "AdvancedMattesMutualInformation", which computes the mutual information between two images to be registered using the method of *Mattes et al.* [107].

2.3.2 TotalSegmentator

TotalSegmentator is a 3D Slicer extension module for automatic segmentation of anatomical structures on whole body CTs (and other image modalities). It is a deep learning segmentation model and can segment 104 anatomic structures (some of them visible on Figure 2.2).

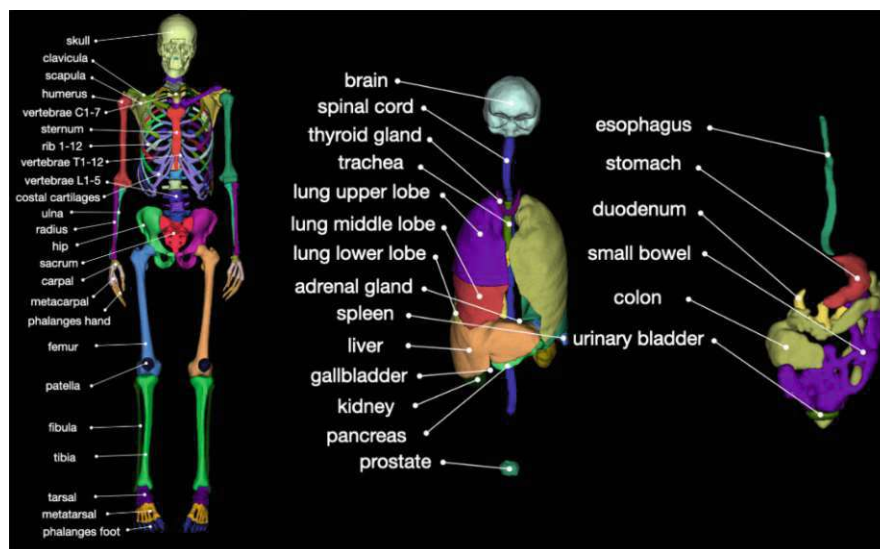


Figure 2.2: Some segmented structures on whole body CT [108]

The algorithm was trained on 1204 CT slices that were randomly sampled from routine clinical studies from different years. The random nature of this selection allows the presence of different ages, abnormalities, scanners, body parts, sequences and sites in this real-world dataset. It is still important to stress the fact that male patients were over-represented in the training dataset [108]. TotalSegmentator has many advantages, like being publicly available, easy to use, able to segment most anatomic relevant structures, and exhibits robust performance. The training dataset is also publicly accessible, which is an important characteristic of explainable AI (XAI).

The model used is a nnU-Net, which is based on a U-Net (see Section 1.3.3) implementation that automatically configures all hyper parameters based on the dataset characteristics [108].

Despite offering reproducibility and repeatability across the different graphic cards (GPU) and processors (CPU), the computing time is significantly influenced by the capacities of the GPU and CPU of the computer used to perform the segmentation. Table 2.2 shows runtime for an Intel Core i9 3.5 GHz CPU and a Nvidia RTX 3090 GPU.

Image Size	1.5mm model (long)			3mm model (fast)		
	Runtime	RAM	GPU Mem	Runtime	RAM	GPU Mem
Small (512x512x280)	1 min 17 s	7.6 GB	6.1 GB	34 s	7.4 GB	5.2 GB
Medium (512x512x458)	2 min 49 s	10.6 GB	8.5 GB	53 s	8.4 GB	7.4 GB
Large (512x512x824)	3 min 32 s	11.8 GB	11.4 GB	1min 23 s	10.6 GB	7.5 GB

Table 2.2: Different runtime and memory requirements for whole body CT [108]

2.4 Previous work

In a previous project [109], different registrations were made with different parameters using ANACONDA. In RayStation, a RIR registration was always acquired to set a Frame-of-reference. After that, three different DIR methods were used:

- The first DIR was done without any controlling ROI, hence using only the intensity-based part of the algorithm ("noContROI"). Showing an amelioration to the RIR, this registration is able to correct for basic long term changes like weight loss/gain and internal organ position shifts.
- Then, the algorithm was used to its full capacity as controlling ROIs were added ("ContROI"). The selected structures had to be delineated on both scans and were selected through a trial and error process to get the best result. This use of the algorithm allows to correct for organ filling, meaning big differences in size, as well as tricky cases of positioning or long term changes.
- A third DIR was performed with the same controlling structures but with a correction on the organs susceptible to filling-caused size variations. The volume of the filling organs is mostly made of matter that will later exit the body. Firstly, it means that this matter does not exist in the other scan and the algorithm cannot achieve a voxel-by-voxel match. Secondly, the dose will not be accumulated there, even if highly irradiated twice, even if the volume is similar in both scans, as it will not be the same content. Therefore, organ walls were created for the bowel (0.5 cm), bladder (0.5 cm), rectum (0.3 cm) and anal canal (0.3 cm), and were used as controlling ROIs in the third DIR ("Wall").

The main concern that drove the choices in the registration parameters was safety. The goal of a registration in the context of the treatment planning of a re-irradiation was to take into account the accumulation of dose to the tissues where the two treatments overlapped. Hence, in a clinical perspective, a good registration is a registration that gives adequate results in the areas that overlap.

To identify the relevant organs in the context of re-irradiation, a distance-to-dose assessment was done for each organ, in each treatment. The coincidence of relevance in both treatments translated an overlap of dose and made the organ relevant for the registration. The choice of the controlling structures was made on the basis of this identification. Hence, most controlling structures were re-irradiation-relevant organs. However, depending on the case, other organs could be used as controlling ROI. Firstly, it could be due to the spatial vicinity of organs, making their delineation propagation dependent on each other. Secondly, it could be due to physically unrealistic propagation. It usually took place in the bones or the external contour, these were then added to the controlling ROIs as tools to assure a reasonable structure. Some organs were used to control the registration more often than others, it was however a very patient-specific process of trial and error that allowed to get a satisfying registration.

2.5 Segmentation comparison

To respond to the fourth goal of this thesis, a comparison of segmentation techniques was done. The segmentation of the organs given as part of the ReCare project was done manually, while TotalSegmentator performed AI segmentation (Figure 2.3). The aim of this comparison analysis was to determine whether the TotalSegmentator's segmentation could be used as QA for the multiple manual segmentations in the ReCare cohort coming from different facilities.

In 3D Slicer, the segmentation was performed on both CTs (AI-Seg CT1 & AI-Seg CT2), visually controlled, and then exported to RayStation in order to measure similarity with the manually segmented structures (STR CT1 & STR CT2). However, TotalSegmentator and the ReCare segmentation protocol had only three structures in common: the right kidney, the left kidney, and the bladder.

This difference in segmentation policy was also visible in the rectum and cauda equina segmentations. TotalSegmentator labeled the rectum as part of the colon, and the cauda equina as part of the spinal cord, making it impossible to compare segmentations. In order to still be able to compare the rectum and cauda equina's segmentations, modifications were performed on the AI-segmented colon and spinal cord to create pseudo-AI-segmented rectum and cauda equina. Similarity metrics of the five organs on the two CTs were then retrieved to compare the segmentation methods.

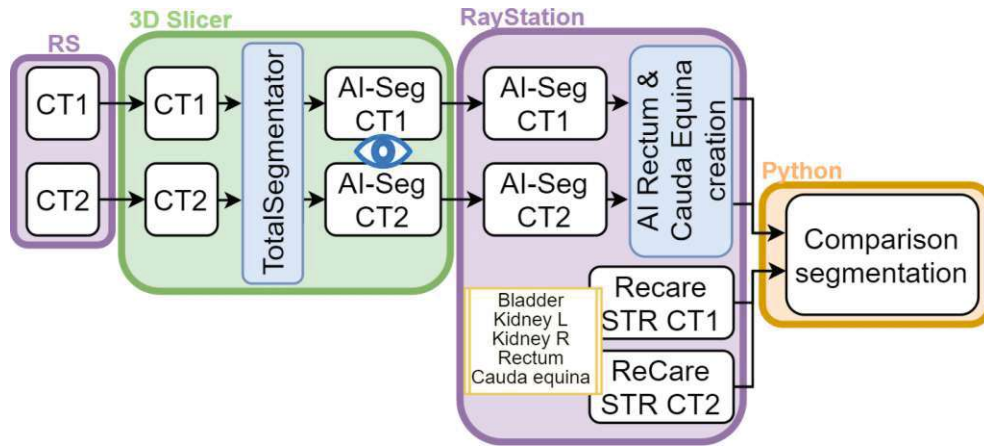


Figure 2.3: Schematic representation of the segmentation workflow

2.6 Registration evaluation

The two algorithms used to perform registrations were ANACONDA and Elastix. As explained in Section 2.4, three methods were tested with ANACONDA and their performances were analyzed in a previous project [109]. In the context of the thesis, a new registration was carried out on 3D Slicer, the workflow established to do so is illustrated in Figure 2.4. To perform a registration, Elastix, as any registration algorithm, needs both moving and target CT scans (CT1 & CT2). In this module, the registration process creates a transform (DIR transform in blue) as well as a new volume representing the registered CT. At this point, a visual evaluation was mandatory, to check the credibility of the registration.

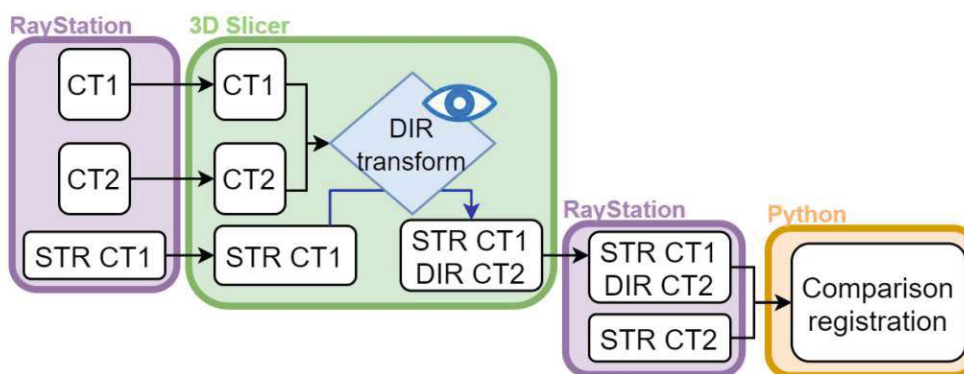


Figure 2.4: Schematic representation of the registration workflow

In order to evaluate and compare this registration with the others, it was necessary to export it back to RayStation. However, the transform couldn't be exported as such to RayStation, and the registered CT cannot be used for analysis on its own. Indeed, what was used to perform registration evaluation were similarity metrics, in particular the Hausdorff distance (HD) and the Dice similarity coefficient (DSC), which were measured between corresponding structures. It was therefore necessary to also import the ten manually-segmented ROIs of CT1 (STR CT1) to 3D Slicer. The DIR transform was thereafter used to register these structures to CT2 in the transform module. The mapped segmentation (STR CT1 DIR CT2) was then exported back to RayStation to be compared to the target segmentation (STR CT2).

2.7 Dose mapping evaluation

In order to analyze dose deformation and its linked uncertainties, it was necessary to generate all registrations. Indeed, the registrations were used to map the dose files using the same transform, as it was assumed that geometric changes in the scans were equivalent to the ones in dose distribution.

The two software have different approaches for dose deformation (Figure 2.5). 3D Slicer uses the DIR transform (in blue) in the same way as it was done for the ROI structures (STR CT1 in Figure 2.4). Hence, in order to perform this transformation, the original first dose file (DOSE CT1) was imported into 3D Slicer.

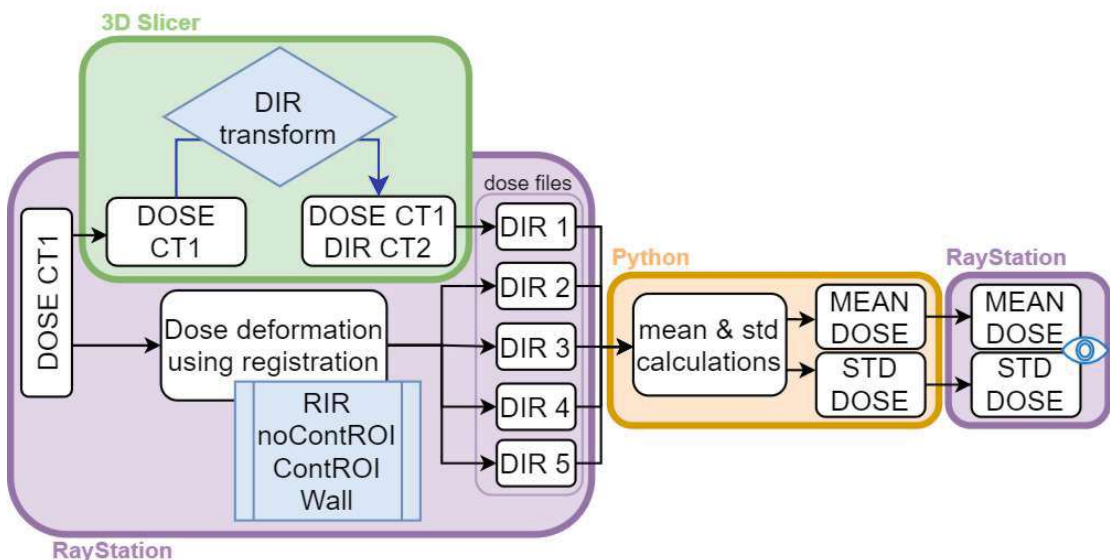


Figure 2.5: Schematic representation of the dose accumulation workflow

Before exporting the dose from RayStation, a weighted sum of that dose was calculated. However, a limitation of RayStation is that even though the coefficient can be modified by the user, it cannot be equal to 1. In order to have a summed dose file with dose values as close as the original one as possible, a weighting factor of 0.99 was applied first. Then, a new summed dose file was created using the first sum, with a coefficient of 1.01, to reach 0.9999 of the original dose. Finally, this second summed dose file was exported, and used in 3D Slicer.

The RT plans were exported as DICOM files to be handled in Python. However, the dose files couldn't be exported from 3D Slicer in the same format as from RayStation. Therefore, the DOSE CT1 DIR CT2 was firstly exported from 3D Slicer to RayStation (DIR 1) and then from RayStation in the same way as the other ones (after the creation of the 0.99x1.01 summed dose file). These five dose files were then imported into Python, and used to create a mean dose file (MEAN DOSE) and a standard deviation dose file (STD DOSE) from their dose values. Then, the two new dose files (mean & standard deviation) were re-imported into RayStation.

There, quantitative and qualitative (see Sections 2.10 & 2.11) evaluations took place. The quantitative evaluation consisted of retrieving dose statistics for the 10 organs, both from the mean and standard variation dose files. The qualitative evaluation consisted of visual identification and analysis of the anatomic location of standard deviation hotspots, in respect to anatomic variation and dose gradients.

2.8 Data Handling

In theory, it should be easy to export a segmentation, a registration, or a dose file from 3D Slicer, and import it into RayStation, as both software use DICOM files and work from the same input (CT1 & CT2). However, in order to compare the performances of the different programs, the data format had to be carefully tracked (Figure 2.6). The detailed checklist established to do so is available in the appendix (Figure 5.1). Although both treatment planning software offer similar tools to perform registration, segmentation and measurements, the communication between both software was difficult. Even comparable formatted files were treated differently in both software and hence not easily shared from one software to another.

Digital Imaging and Communications in Medicine (DICOM) is a technical standard developed for the communication and management of medical images and related data [110]. This format organizes information in datasets. In DICOM, a Composite Information Object Definition (CIOD) represents parts of several entities in the DICOM Model of the Real-World [111]. They are not inherent to the object but rather inherent to the related real-world objects, and usually consist of non-image data. In a CIOD, the entire context is exchanged between application entities.

The CT scans are stored as CT Image CIODs, segmented ROI sets are exported as RT Structure Sets CIODs, and dose files as RT Plan CIODs [112]. Each of them have modules in common, like Patient, Clinical Trial Subject, General Study, Frame of Reference, or General Equipment. However, they also all have modules that are specific to their respective use. Moreover, they do not store the actual data in the same way. The CT image CIOD makes use of the Image Plane and Image Pixel modules, the RT Structure Set CIOD uses the Structure Set and ROI Contour modules, and the RT Plan CIOD stores its data in the RT General Plan and RT Beams modules [112].

In order to perform image similarity measurements, both segmentations had to be on one software, either Raystation or 3D Slicer. The major problem arising when using 3D Slicer was its requirement of CPU and GPU power while performing specific tasks. Similarity measurements with 3D Slicer could only be performed on binary labelmaps. In a binary labelmap, a value is attributed to each voxel to specify whether it is inside or outside the region. However, the computing power necessary to convert a closed surface segmentation to a binary labelmap was too demanding for the computer's capacities. The configuration of the computers at disposal being insufficient to ensure a smooth handling of the measurements, it was decided that the comparison would be done on RayStation. However, a structure file couldn't be exported from 3D Slicer to a RT Structure Set file on its own, it had to be exported as part of a study, containing its corresponding CT.

In the same way as for structure sets, dose files could not be exported from 3D Slicer on their own, but needed a CT scan to be linked with in a study. It is important to specify that, for each patient, three different studies had to be exported. The first one containing the AI-segmentation of CT1 (AI-Seg CT1) and CT1. The same structure could not be used for CT2, because there were two different segmentations to export, and the DICOM format can only accept one. Hence, the second study contained the AI-segmentation of CT2 (AI-Seg CT2) and CT2. The third study compiled the dose file deformed to the registration performed in 3D Slicer (DOSE CT1 DIR CT2), the ReCare segmentation registered to CT2 in Slicer (STR CT1 DIR CT2), and the CT2.

Once uploaded to RayStation, the CTs appear as additional CTs to the patient data, identical to the original CTs but bearing the structure sets and linked to the imported dose file. The newly imported CTs was aligned to the original ones via a Frame-of-Reference before the imported ROIs were copied to the original CTs. Having the original and registered ROIs, as well as the manually- and AI-segmented ROIs, on the same CT allowed for DSC and HD measurements, necessary for registration and segmentation evaluations, to be done.

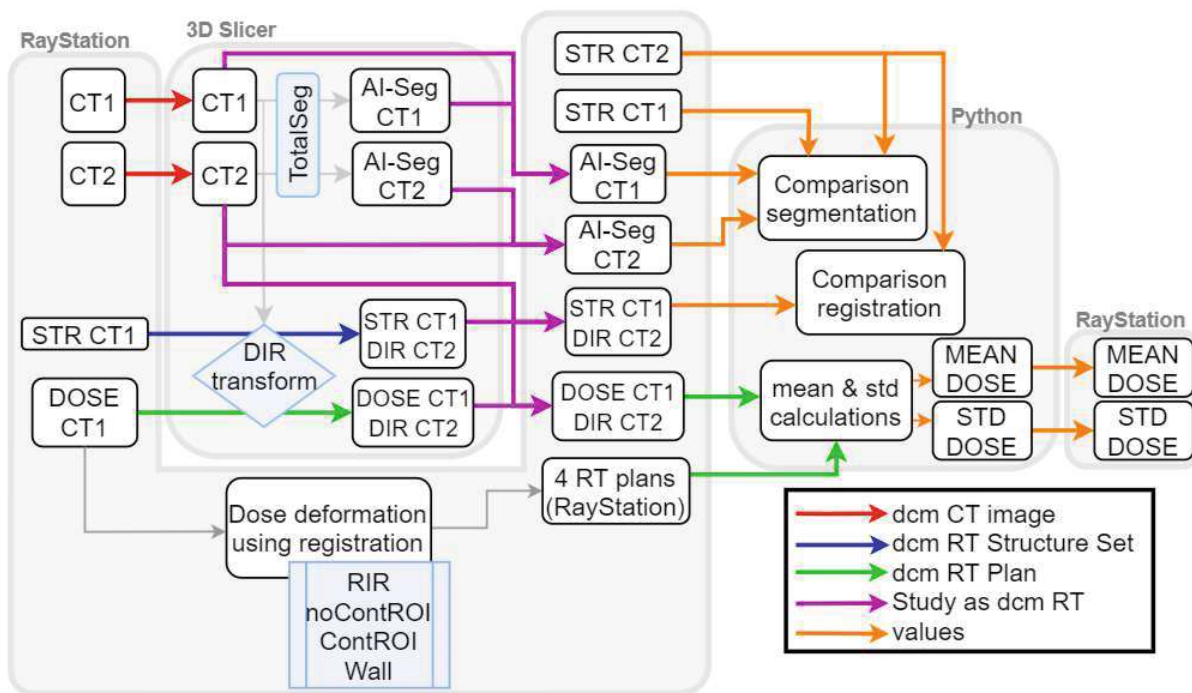


Figure 2.6: Simplified schematic representation of the complete workflow

In the context of segmentation comparison, five structures were copied to the original CT: the right kidney, the left kidney, the bladder, the colon, and the spinal cord. Then, using ROI algebra, a pseudo-AI-segmented rectum and a pseudo-AI-segmented cauda equina were created from the colon and spinal cord structures respectively. To do so, the manually segmented structure (Rectum_ReCare or CaudaEquina_ReCare) was selected as expression A with 5 cm margins in the right, left, anterior, and posterior directions. The output (Rectum_3DS or CaudaEquina_ReCare) was the intersection of the expression A and the AI-segmented structure selected as expression B. With the brush tool, the contours were then modified in order to match the rectum rather than the colon contour. This step was not necessary in the cauda equina case. DSC and HD were then performed on ROIs segmented on both CTs to evaluate the segmentations.

The comparison of dose deformation did not require the segmented ROIs, but the mean dose and its standard deviation. These two dose files were created in a Python code, with the five dose files (four from RayStation and one from 3D Slicer) as input.

2.9 Dose uncertainties calculation

In order to quantify dose accumulation uncertainties, the mean and standard deviation were calculated from five dose files of the same original dose and registered with different strategies (Figure 2.5). Although this process does seem straight forward, and easily implementable in a Python script, a major challenge arose. Because of the DIR process, the dose files didn't have the same dimensions as the original CT1 dose file. Furthermore, because the registrations were not all performed on the same software, the files did not have the same dimensions once registered. Indeed, between 3D Slicer-deformed dose files and RayStation-deformed ones, differences in each of the three dimensions (slices, rows, columns) were accounted for in every dataset. Because the comparison was then made on RayStation, and because there were more dose files generated by this software, the RayStation dimensions were chosen to be used as reference.

The data had to be resampled in order to align the Slicer dose distribution to the reference and change its dimensions. It is important to mention that, as the registrations were non-rigid, the dimension changes were not centered, nor did the pixel information match. Therefore, a solution that would use pixel padding to re-center the dose file and match the dimensions would not only be complicated because of location of the padding, but also because the alignment would never be satisfying. For this reason, the two dose files (Slicer and the RayStation reference) were converted to the ITK image format. Indeed, an image in ITK format is not treated as an array of pixels/voxels, but as a set of points on a grid occupying a physical region in space [113]. The definition of the region in physical space that the image occupies is given by:

- Image origin: location in the world coordinate system of the voxel with all zeroes coordinates
- Pixel spacing: distance between pixels (along each of the dimensions)
- Direction: cosine matrix
- Size: number of pixels in each dimensions

The benefit of using ITK rather than the pixel array retrieved from the *dcmread* function is highlighted by the three first parameters.

The notion of the image's location in physical space is essential to align them. The image origin consists of the three coordinates of the first voxel (T_x , T_y , T_z). Moreover, it is a parameter that is given in the Image Plane Module of the DICOM file as the Image Position Patient attribute (IPP in Figure 2.7) [114].

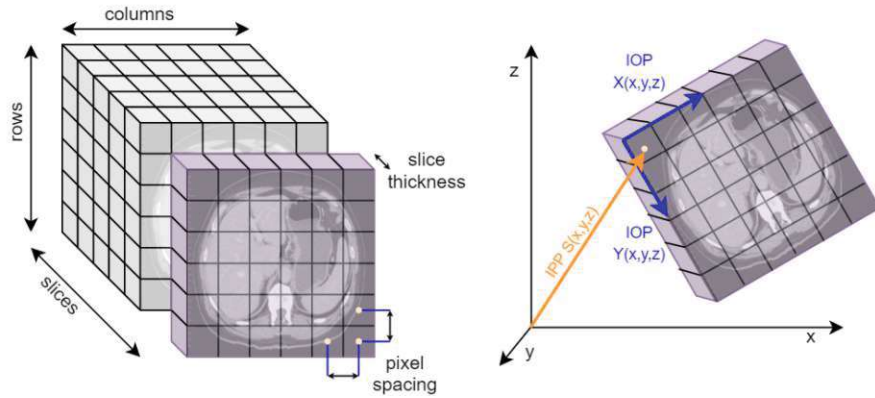


Figure 2.7: DICOM data tags

Furthermore, the Direction gives the direction of each axis. It is stored in the Image Orientation Patient (IOP in Figure 2.7) of the DICOM file as 2x3 matrix (R_{nx}, R_{ny}) , giving the direction cosines of the first row and first column with respect to the patient. The Patient-Based Coordinate System is a right handed system, i.e., the vector cross product of a unit vector along the positive x-axis and a unit vector along the positive y-axis is equal to a unit vector along the positive z-axis [114]. Provided as a pair, these attributes give the input of a spatial transformation matrix as follows:

$$\begin{bmatrix} R_{xx} & R_{xy} & R_{xz} & T_x \\ R_{yx} & R_{yy} & R_{yz} & T_y \\ R_{zx} & R_{zy} & R_{zz} & T_z \\ 0 & 0 & 0 & 1 \end{bmatrix} \quad (2.9.1)$$

Although it was not a problem with the datasets used in this thesis, specifying the pixel spacing, and not assuming an isotropic spacing is important. Once again, this information is stored in the DICOM file, under the Pixel Spacing attribute (row, column) and the Slice Thickness attribute (slice).

The ResampleImageFilter class was used to resample the Slicer image to match the RayStation grid by changing its orientation and origin. By using SetReferenceImage, the filter sets the output image's size, origin, spacing and direction to match the provided reference image [115]. Since resampling involves mapping from one grid to another, an interpolator was required to compute the values at positions that do not align directly with the grid points of the output image, especially because resampling is performed in physical space coordinates rather than voxel grid coordinates. Three interpolators are available to choose from: linear, nearest-neighbor, and B-spline [115]. The three of them were tested, and after visual evaluation of the results, the B-spline interpolator was selected as the most satisfying.

Once the Slicer dose file was the same size as the four other files, they were all used for further calculations. Three for loops were used to go through every voxel of the datasets and perform a mean and standard deviation calculation. However, in order to make sure that the calculations were done on correct grounds, two verification files were also created: checkDIR and checkWall. The checkWall was just the wall dose file re-written in a new DICOM file (could be done with any RayStation file). It was used to check on the loops and on the DICOM saving process, as it should not display any changes. The checkDIR is simply the resampled 3D Slicer dose file. It was used to see and quantify the impact of interpolation. It also allowed to perform a mean file as a summed dose file in RayStation and check the accuracy of the Python computed mean. Although there was nothing to compare the standard deviation calculation to, the other verifications provided enough proof of correctness.

The new dose files then had to be saved as DICOM files. To do so, the arrays' content was converted to 16-bit unsigned integers, and saved on a copy of one of the RayStation DICOM file. Before saving the new DICOM file, the file's metadata was mostly re-used to be sure it was correct. Metadata includes attributes such as the ones mentioned in Figure 2.8.

```
(0028, 0002) Samples per Pixel          US: 1
(0028, 0004) Photometric Interpretation CS: 'MONOCHROME2'
(0028, 0008) Number of Frames          IS: '80'
(0028, 0010) Rows                      US: 52
(0028, 0011) Columns                   US: 78
(0028, 0100) Bits Allocated             US: 16
(0028, 0101) Bits Stored                US: 16
(0028, 0102) High Bit                   US: 15
(0028, 0103) Pixel Representation       US: 0
(7fe0, 0010) Pixel Data                 VR.OV: Array of 648960 elements
```

Figure 2.8: Metadata

In the case of old scans where the orientation and position would be very different from the new ones because of changes in standards, a modification of the code should be done. A pseudo-RIR was performed in the code before using the ResampleImageFilter class. The main goal being the translation of the origin. The rotation values were also used as input in the code, the outcome was however not significant.

2.10 Qualitative evaluation

The subsequent analysis aimed to identify the challenging regions of dose deformation using the mean and standard deviation dose files, and to determine the factors causing these dosimetric uncertainties. Dosimetric uncertainties can usually be defined as a combination of a certain dose distribution pattern and geometric uncertainties. Hence, a side-by-side evaluation allowed to locate the standard deviation hotspots and directly put them in perspective with the mean dose at this specific position.

While geometric variations were examined on the "Deformation grid" tool, or by looking at the similarity metrics gathered from the registration evaluation. The geometric differences between the two CT scans were also visually inspected using the "Fusion" tool. Moreover, data from the previous project [109], gathering evaluation of overlap and computation of registration with controlling structures, was be accessible for a better understanding of the geometric differences. The dose statistics to organs were also retrieved and used for identification of patients and ROIs of interest and for analysis.

2.11 Quantitative evaluation

2.11.1 Metrics

Although a qualitative evaluation is essential for situation assessment and determination of a registration strategy, a quantitative evaluation is necessary to confirm the results and compare them. In this thesis, two metrics were chosen: the Dice Similarity Coefficient (DSC) and the Hausdorff Distance (HD). They were selected because they are some of the most used in validation of image segmentation and registration. Moreover, they both give different information on the similarities between two sets. Both metrics are also retrievable directly on RayStation with the function `SimilarityForDeformablyMappedRoiGeometry()`.

The DSC measures the overlap between two volumes by giving a ratio of the intersection of the two sets to their union [116]. Hence, a score of 1 would mean a full overlay of the two sets, while a score of 0 indicates no match between the two volumes.

$$D = \frac{2 | A \cap B |}{| A | + | B |} \quad (2.11.1)$$

It is important to note that the DSC is dependent on the volume of the structure and will not give similar results for very large and very small structures for the same variation (Figure 2.9).

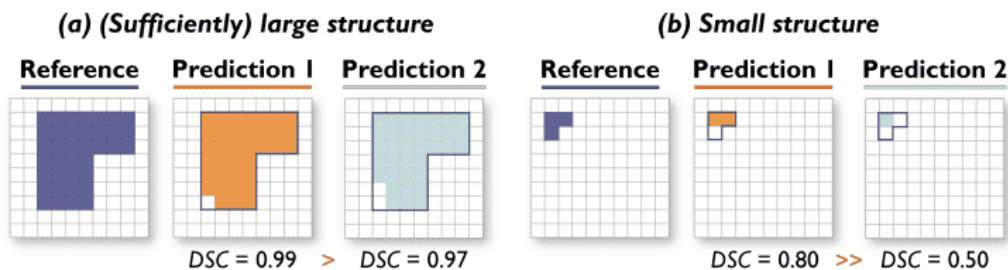


Figure 2.9: DSC Volume dependence [117]

On the other hand, the Hausdorff distance is a spatial distance based metric, evaluating the quality of the delineation propagation [118]. This metric will give the maximal distance from a point in one set to the closest point in the other set. As stated in the Raystation function description, two distance transforms are computed:

- Each point (/voxel) on the surface of ROIA will be assigned the minimum distance to a point (/voxel) on the surface of ROIB
- Each point (/voxel) on the surface of ROIB will be assigned the minimum distance to a point (/voxel) on the surface of ROIA

The HD is then given by the maximum of the the maximum of the distances in the first distance transform and the maximum of the distances in the second one.

$$\delta_H(A, B) := \max\{\sup_{a \in A} d(a, B), \sup_{b \in B} d(A, b)\} \quad (2.11.2)$$

The smaller the HD, the better the delineation propagation. It will give information on the shape similarities that DSC cannot provide, as illustrated in Figure 2.10.

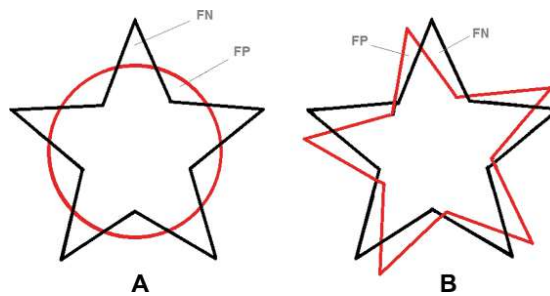


Figure 2.10: Boundary delimitation similarities with HD [118]

Dose statistics

Dose statistics convey the quantity of dose received by a volume. It consists of how much dose is received in a certain percentage of the volume. Dose-volume histograms (DVH) translate this relation between radiation dose and volume. Dose statistics can be retrieved from DVH. Hence, the D99 dose is the dose received by 99% of the volume. For example in Figure 2.11, D1 of the bowel is of 2.76 Gy, meaning that only 1% of the bladder receives 2.76 Gy, whereas 99% of the urethra gets 52.89 Gy. Despite giving a precise measure of the volume receiving a certain dose, DVH does not provide spatial information.

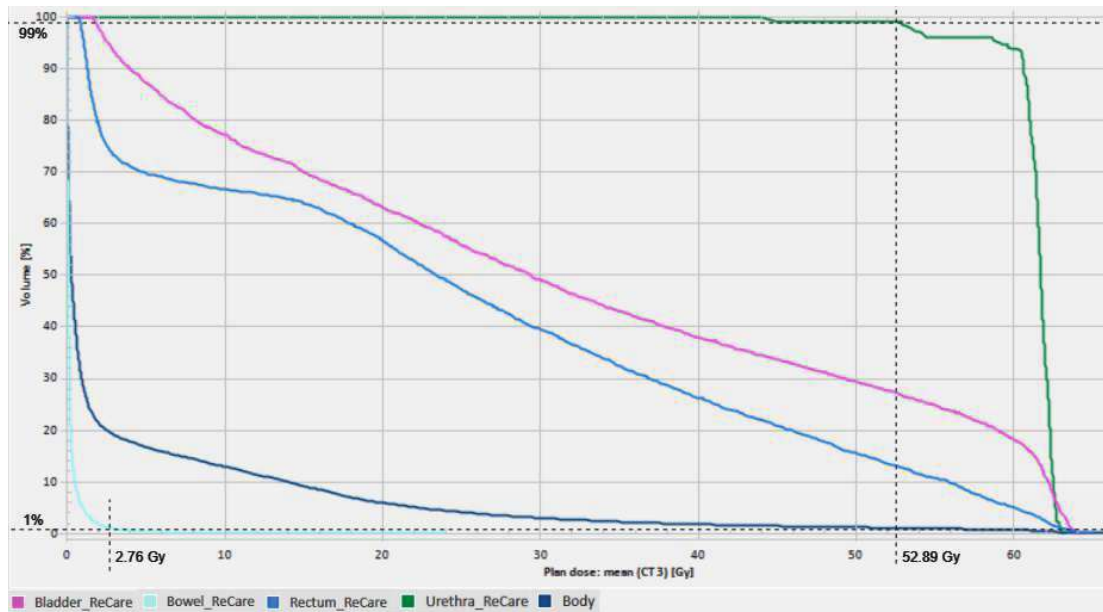


Figure 2.11: Dose-volume histogram of patient n°2339

However, when retrieved from the STD DOSE (Figure 2.5), the dose values do not represent the radiation dose to volume, but rather its variation. The dose statistics retrieved were D1, D99 and Daverage, and give a quantitative evaluation of the dose uncertainties in ROIs. D1 is used for the identification of hotspots, and Daverage rather for inter-ROI or inter-patient comparisons.

2.11.2 Statistics

The registration analysis was performed on the DSC and HD values of the ten organs belonging to the ten selected patients. The samples were paired because the performance of the three methods were compared when applied to the same ten patients. Because of the nature of the two metrics chosen for analysis, the data did not follow a normal distribution. DSC data were right skewed, and HD data was left skewed. In such situations, the application of the t-test was not possible.

In the case of DSC, it was possible to use its logit value in order to obtain a normal distribution and perform a t-test. Hence, a two-tailed t-test was done on the logit DSC values. The distribution of the HD values cannot be changed, hence a two-sided Wilcoxon Rank-sum test was done on the HD values, as a symmetrical distribution of the data was assumed.

It is necessary to specify which standard deviation was used to calculate the standard deviation dose file. As described in Section 2.9, the calculation was done for each voxel one by one. Therefore, the input to the calculation is five values, one of each dose file, and hence the sample standard deviation should be used.

$$\sigma = \sqrt{\frac{\sum_{i=1}^n (x_i - \bar{x})^2}{n - 1}} \quad (2.11.3)$$

with n , the number of data points; x_i , the individual values in sample; and \bar{x} , the mean of x_i .

However, for quantitative comparison analysis, the relative standard deviation (RSD) values was employed. As made explicit in the following equation, the RSD is the ratio of the standard deviation and the mean, presented as a percentage.

$$RSD = \left| \frac{\sigma}{\bar{x}} \right| \times 100 \quad (2.11.4)$$

In this work, the RSD values calculated with the values retrieved from the MEAN DOSE and STD DOSE files were referred to as $u_{D,1\%}$ and $u_{D,av}$.

3 Results

3.1 Preliminary results

The main tendencies of the preliminary project are summarized in this section. The employed metrics indicated a lower performance of the method without controlling ROIs (noContROI) than the two other methods, while the method with controlling ROIs and the one using wall structures had very similar values. The statistical tests (Table 3.1), confirmed this tendency: there was a significant difference ($p < 0.05$) between the ContROI and noContROI methods, as well as between the Wall and noContROI ones. Furthermore, there was no significant difference between the two methods using controlling structures.

Metric	ContROI-noContROI	Wall-noContROI	Wall-ContROI
DSC p-value	5.42E-6	4.11E-6	0.612
HD p-value	1.98E-5	3.69E-5	0.373

Table 3.1: Comparison of methods (all 10 organs) from project [109]

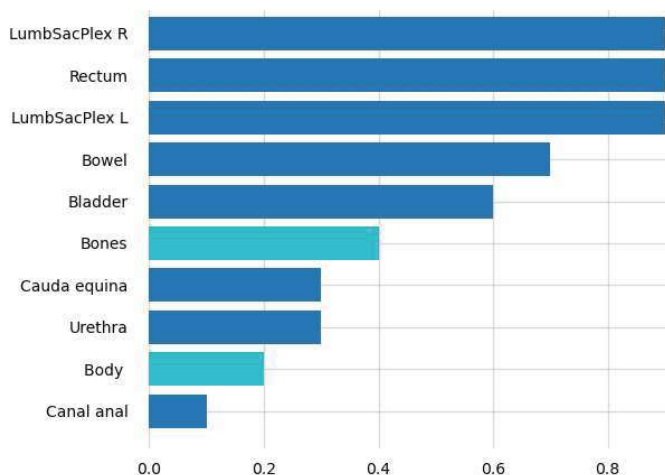


Figure 3.1: Frequency of each organ being used as controlling ROI across cohort

One of the goals of the prior project was to determine the most appropriate selection of controlling structures to get the best registration in the patient-specific re-irradiation context. The structures used as controlling ROIs have a direct impact on the quality of registration of the ROI and its neighboring region.

As the registrations were analyzed and further used in this work, it is important to know how often organs were used as controlling ROIs in registrations, which is summarized in Figure 3.1. The kidneys are not mentioned in the table because they were never used as controlling structures. Body and bones are not part of the segmented organs list, but were still sometimes used as controlling ROIs.

3.2 Segmentations

Compared to other similarity metrics retrieved in this work, the ones presented here for the segmentation analysis contain measures retrieved from both CTs of every patient. It means that for each organ there were 20 samples instead of the usual 10 samples available. However, one pair (one patient) of rectum volume measurements was identified as significant outliers and had to be removed. Therefore, the volume means, standard deviations, and statistical analyses were performed using only 18 samples.

Table 3.2 collates the means and standard deviations of the DSC and HD between manually and AI-segmented structures. These values translate a very high similarity between the two segmentation methods, as well as a low variability in their performance.

Metric	Bladder	Left kidney	Right kidney	Rectum	Cauda equina
DSC	0.89 ± 0.09	0.91 ± 0.02	0.92 ± 0.02	0.79 ± 0.25	0.85 ± 0.02
HD /cm	1.46 ± 1.18	2.26 ± 0.17	2.16 ± 0.46	1.34 ± 1.00	1.30 ± 0.40

Table 3.2: Means and standard deviations of the DSC and HD of the five segmented structures

Counterintuitively, the kidneys demonstrate the highest DSC scores, but also the highest HD ones. However, they show the lowest interquartile ranges in both metrics in this dataset's box plot (Figure 3.2). The bladder shows the highest HD data spread (both IQR and whiskers), but its mean and median are considerably lower than the kidneys.

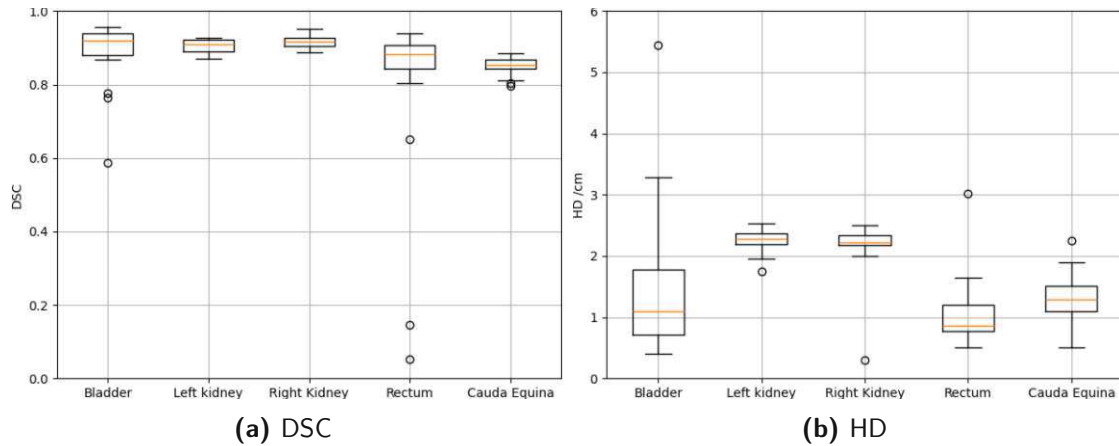


Figure 3.2: General box plot of the four segmented structures

Figure 3.3 translates the volume differences between the two segmentations. Specifically, this bar chart shows the mean and standard deviation of the ratio of the ReCare and Slicer volumes for each organ. It represents the volume differences, with positive values indicating the manual segmentation is larger and negative values indicating it is smaller than the AI one. Thus, manual segmentation tends to delineate a larger volume for the kidneys and rectum, while the AI segmentation volume is larger for the bladder and cauda equina.

A value near zero means the volumes are almost identical, which is the case of the bladder. Moreover, a one-sample t-test was performed to determine whether there is a significant difference from zero, with conclusive p-values ($p < 0.05$) indicated by a star in Figure 3.3.

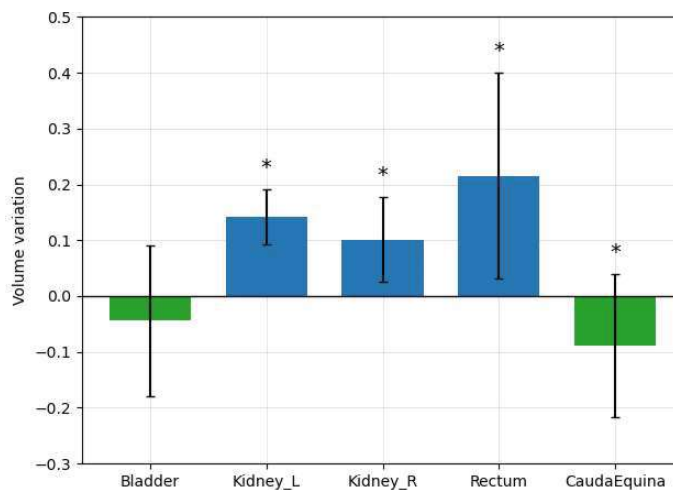


Figure 3.3: Volume variations of the five segmented structures

3.3 Registrations

In order to have a better understanding of the anatomical variations in between the two datasets, Figure 3.4 compiles for each organ, the average ratio of the bigger volume and the smaller volume of the two CT scans. The figure demonstrates the existence of filling organs, thus showing that their volume was more prone to variation.

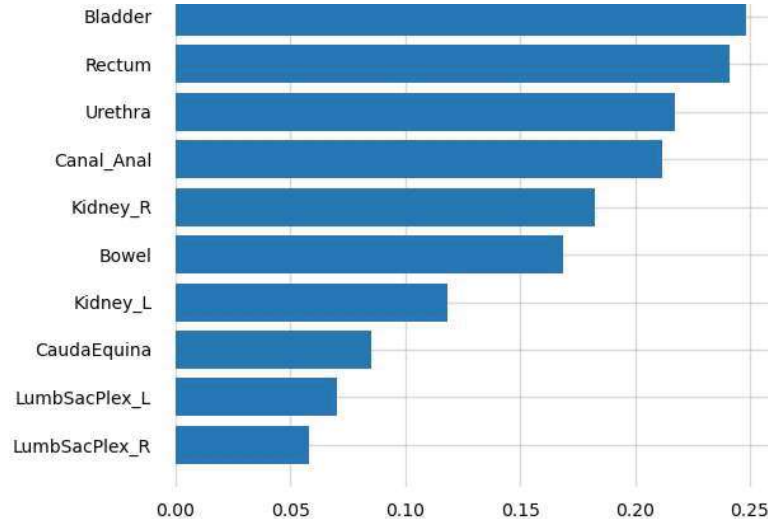


Figure 3.4: Average volume variation for analyzed organs

The Elastix DIR used in 3D Slicer is intensity-based, therefore two comparisons are of interest: one with the intensity-based ANACONDA method (noContROI), and one with the method using controlling structures (ContROI). Table 3.3 displays the mean and standard deviation for each of these methods, and each metric highlights a tendency. The DSC shows a similar performance of the two intensity based algorithms while the ContROI method clearly outperformed them. The HD presents a contrasting tendency, as the Slicer DIR (SDIR) clearly demonstrates a better performance than the noContROI method, whereas the ContROI method still gives better results. Moreover, the HD standard deviation of the Slicer DIR is substantially smaller than the two others.

Metric	noContROI	ContROI	SDIR
DSC	0.74 ± 0.19	0.81 ± 0.22	0.70 ± 0.20
HD /cm	1.87 ± 1.69	1.57 ± 1.80	1.69 ± 1.23

Table 3.3: Means and standard deviations of the DSC and HD of the three methods

The statistical results in Table 3.4 confirm the general trend that was already observed in the project: both intensity-based algorithms exhibit similar performances, while using controlling structures demonstrates a significant difference. However, for the general DSC results, a higher p-value but still significant one arises between noContROI and SDIR.

Metric	ContROI-noContROI	noContROI-SDIR	ContROI-SDIR
DSC p-value	5.42E-6	0.002	9.12E-11
HD p-value	4.85E-5	0.922	2.03E-4

Table 3.4: Statistical comparisons between different methods (all 10 organs)

Although the interquartile ranges (IQR) are relatively similar, the wider spread of outliers in the HD box plot (Figure 3.5b) reflects the greater variability in the RayStation data, which corresponds to the larger standard deviation mentioned earlier. The DSC box plot (Figure 3.5a) is also similar to the previously presented data with the ContROI method exhibiting significantly higher DSC, and noContROI showing a better performance than SDIR. Moreover, the Slicer DIR has a median lower than 0.8.

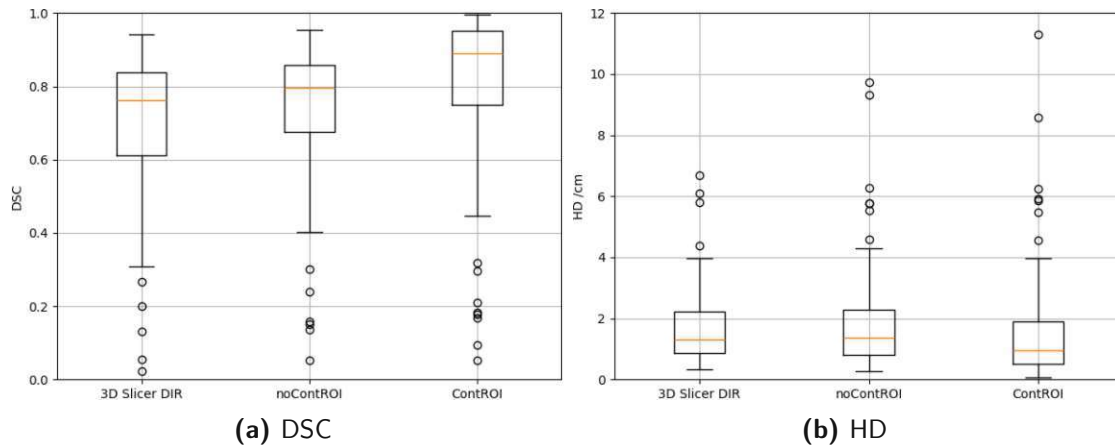


Figure 3.5: General box plot of the three methods

Table 3.5 collates the significant results of the statistical tests on the DSCs. Significant differences between the two RayStation methods were identified in half of the organs analyzed: the bladder, the bowel, both sacral lumbar plexuses, and the rectum. These values confirm the general trend as p-values are similar between ContROI and noContROI and between ContROI and SDIR. The SDIR also shows significant differences with both RayStation registrations for the cauda equina, as well as with noContROI for both lumbar sacral plexuses.

Organ	ContROI-noContROI	noContROI-SDIR	ContROI-SDIR
Bladder	0.005	0.176	0.005
Bowel	0.021	0.767	0.039
Cauda equina	0.432	0.001	0.005
Left lumbar plex.	1.61E-4	0.007	9.39E-6
Right lumbar plex.	1.42E-4	0.018	5.96E-5
Rectum	0.010	0.062	0.002

Table 3.5: Comparison of methods on selected structures (DSC p-values)

Table 3.6 compiles the results from the statistical analyses of the HDs, including only those with p-values under 0.05. It confirms the first tendency, as the impact of controlling structures is defined as significant against both intensity-based methods for the bladder and the right sacral lumbar plexus.

Organ	ContROI-noContROI	noContROI-SDIR	ContROI-SDIR
Bladder	0.006	0.625	0.004
Right lumbar plex.	0.037	0.625	0.037

Table 3.6: Comparison of methods on selected structures (HD p-values)

In Figure 3.6, both metrics of the bladder dataset exhibited a similar trend when controlling structures were used in ANACONDA: an improvement in performance, as well as a decrease of the interquartile range and of the size of the box plot's whiskers, although some outliers remained.

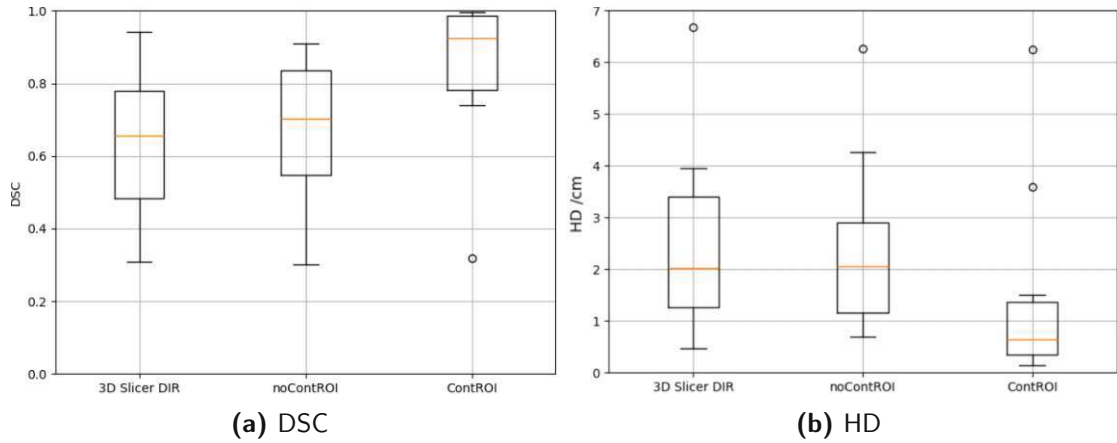


Figure 3.6: Bladder box plot of the three methods

The differences of the bowel's HD is presented in Figure 3.7b, where a better performance can clearly be observed when the Slicer registration was used rather than noContROI. This difference was however not significant. For this organ, the size of the IQR is considerably greater in ANACONDA methods. The DSC box plot (Figure 3.7a) pictures more classical results; the hybrid method outperforms the two others. It can nevertheless be specified that all DSCs for this organ are relatively high.

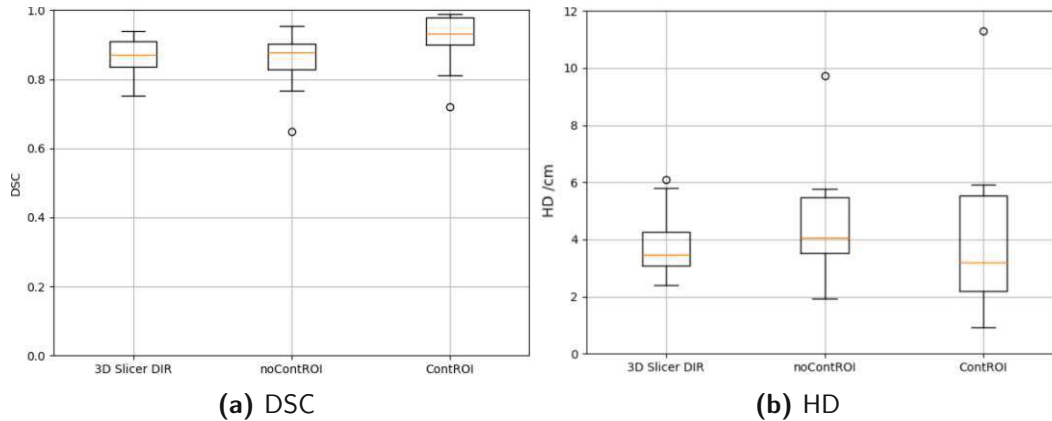


Figure 3.7: Bowel box plots of the three methods

Both sacral lumbar plexuses have very similar DSC box plot, thus only the left one is shown in Figure 3.8a. It translates a great improvement when controlling structures were used, confirming the extremely low p-values. The difference in the spread of HD data between both plexuses is important and helps make sense of the asymmetry in p-values. Focusing only on the IQR of the HD box plots, the right lumbar sacral plexus (Figure 3.8b) shows a significantly lower range than the left one (Figure 3.8c), while the medians are consistent between both plexuses across all methods. Furthermore, the HD box plots clearly show lower HD medians for the ContROI method.

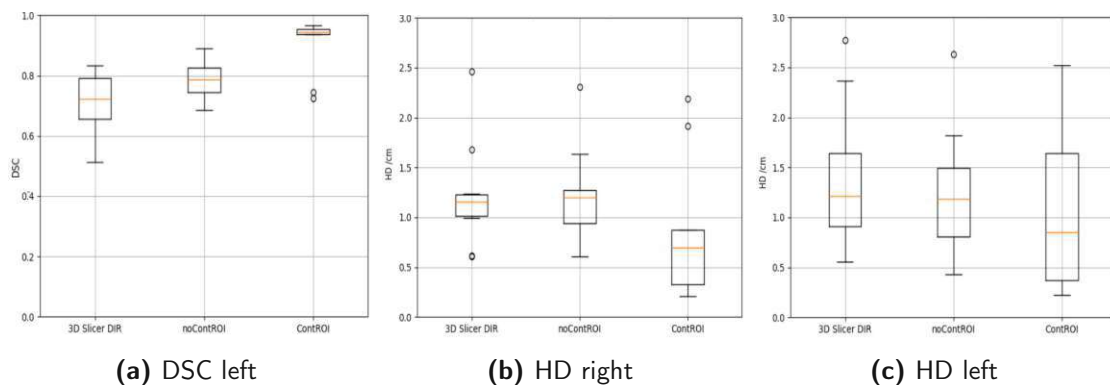


Figure 3.8: Lumbar plexuses box plots of the three methods

Figure 3.9a gives a visual explanation of the statistical results of the cauda equina. The spread of the SDIR DSC data is considerably larger than the ANACONDA methods, and its median value is also notably lower. The HD box plot in Figure 3.9b, shows slight differences in performance, but mostly similar median values, IQRs and whiskers' sizes.

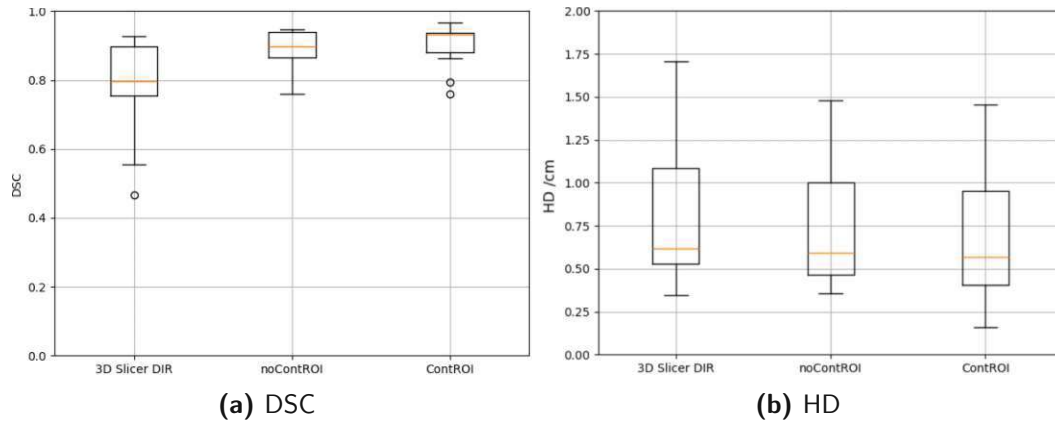


Figure 3.9: Cauda equina box plots of the three methods

The "filling organs" were a group of interest in the analysis of deformable registrations as they were the ones having the biggest and most frequent volume changes. The bar charts in Figure 3.10 illustrate how methods using controlling structures generally gave a better mean score in both metrics. However, it also shows that they did not improve the scores of the anal canal.

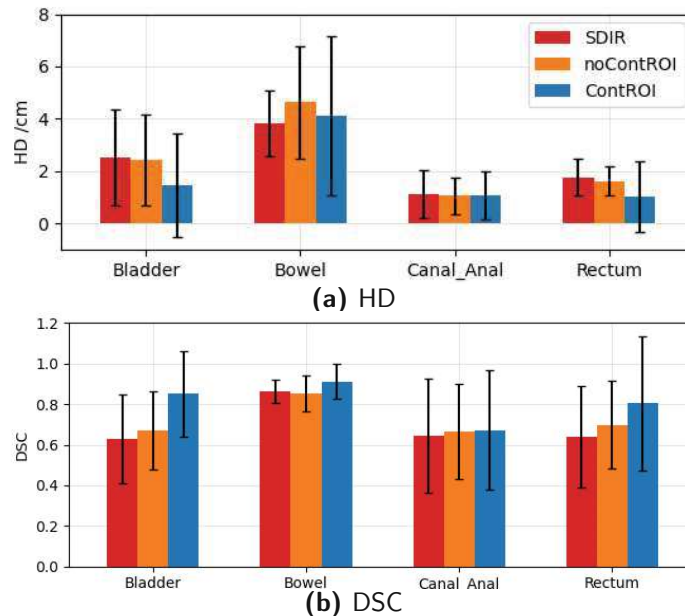


Figure 3.10: Bar chart of the three methods' DSC and HD for filling organs

3.4 Dose mapping

The evaluation of the dose accumulation was mainly qualitative, dose and uncertainties statistics (Table 3.7) were used as a tool to identify patients and ROIs with important dosimetric variations. Out of this visual examination, four factors of dose uncertainties were identified: dose gradients, body contours, ROI deformation (by controlling structures and image information), and the distance to target. Although these factors are distinct, it is usual for a variation hotspot to be the result of multiple factors acting in combination.

Uncertainties caused by steep dose gradients were observed in all patients. However, the regions where they were identified were different for each patient as dose distributions are case-specific. The example shown in Figure 3.11 illustrates dose variations in the steep gradient region along the rectum contour (in orange), which was used as a controlling structure in the two hybrid DIRs.

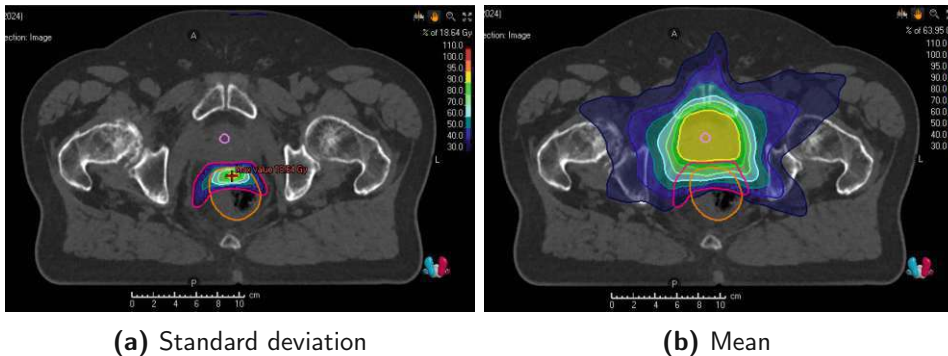


Figure 3.11: Dose uncertainties due to controlling ROI-caused geometric variations in steep dose gradients. Patient 2694

Other uncertainties could be directly linked to specific organs and their deformation. Dosimetric uncertainties located in the vicinity of a ROI used as controlling structures were observed in nine patients. In Figure 3.12, the bladder (green), bowel (red), and rectum (orange) were used as controlling structures and generate dosimetric uncertainties in a region without gradient or high dose.

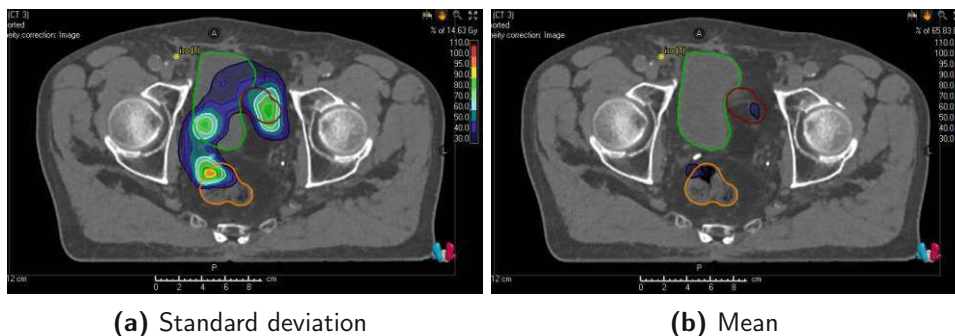
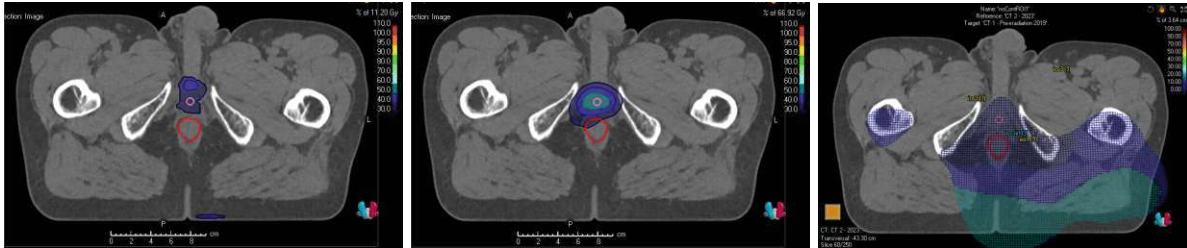


Figure 3.12: Dose uncertainties due to controlling structures outside of steep dose gradient. Patient 2339

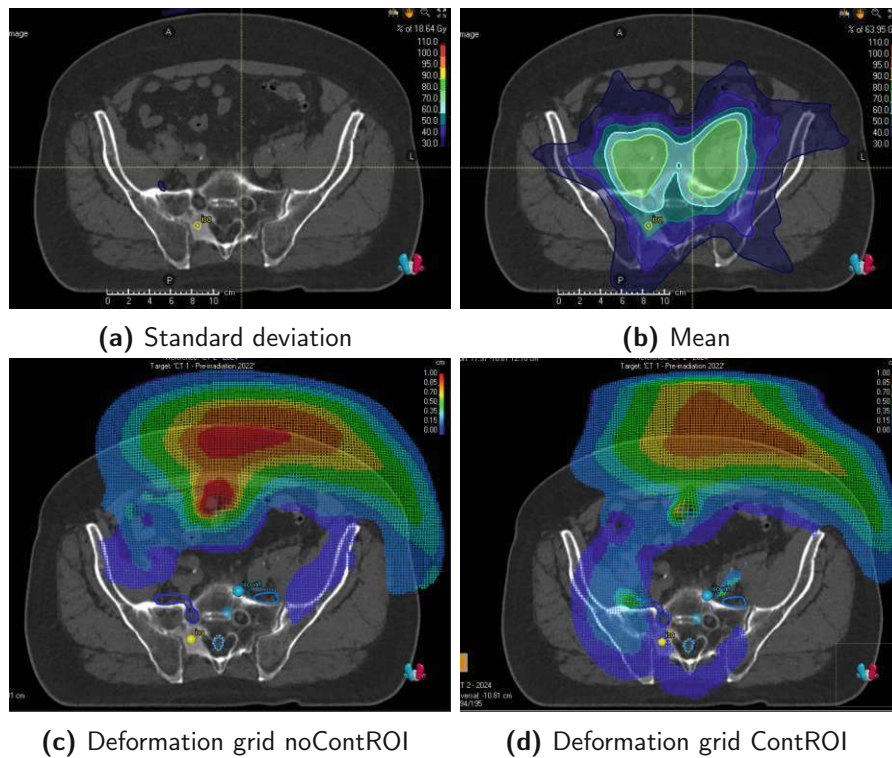
It was also determined in six different patients that some regions, hence ROIs, were subject to important intensity-based deformations. The region most prone to intensity-driven deformation is the region of the anal canal as visible in Figure 3.13. This region also shows high $u_{D,1\%}$ and $u_{D,av}$ values in Table 3.7.



(a) Standard deviation (b) Mean (c) noContROI deformation grid

Figure 3.13: Dose uncertainties due to intensity-caused geometric variations. Patient 2281

It is however important to keep in mind that dosimetric uncertainties are a complex combination of dose distribution and geometric uncertainties. Hence many significant geometric deformations visible on the deformation grid did not induce dosimetric uncertainties.



(c) Deformation grid noContROI (d) Deformation grid ContROI

Figure 3.14: Important deformation handled differently by the registrations taking place out of the high dose region do not generate dosimetric uncertainties. Patient 2694

The case of patient 2694 presented below shows how large variations in the contour and the bowel (Figure 3.14c & 3.14d), handled differently in both ContROI and no-ContROI methods (and others), did not generate large dosimetric uncertainties as they were not close to high dose regions (Figure 3.14a & 3.14b). Conversely, small geometric deformations taking place in a high dose distribution will induce a significant standard deviation.

Important dosimetric uncertainties were highlighted in the external contour (Figure 3.15) of the body in eight patients. A clear reduction of the dosimetric uncertainties is visible between Figure 3.15a and 3.15b. To offer an even clearer visualization of the differences in the contours caused by the removal of the RIR from the mean and standard deviation calculations, Figure 3.15c presents the spatial distribution of the standard deviation difference of the two dose files (all reg.& noRIR). This diminution of standard deviation is also visible in Table 3.7, where the means and standard deviations of $u_{D,1\%}$ and $u_{D,av}$ of the body contour were found significantly (*) smaller for the noRIR calculation than for the all reg. one.

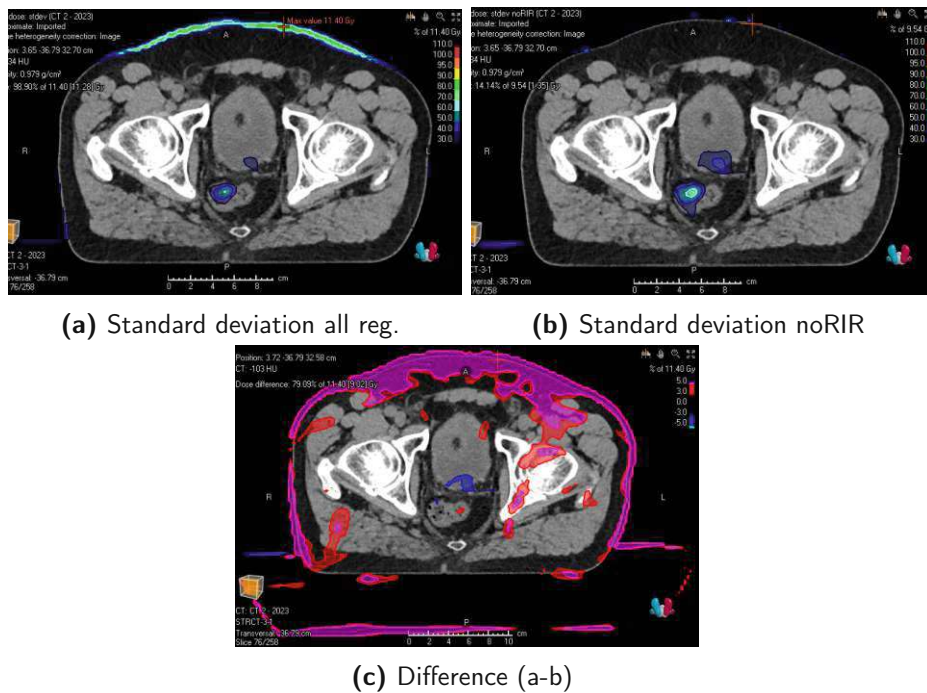


Figure 3.15: Differences in contour dose uncertainties between all reg. and noRIR.

Table 3.7 presents the means and standard deviations of the $u_{D,1\%}$ and $u_{D,av}$ across all organs from both all reg. and noRIR calculations. The significant differences between calculation methods are marked with an asterisk. This table highlights the important variability observed in the anal canal, rectum, and bladder—all of which are filling organs—as well as high $u_{D,1\%}$ values for the kidneys.

Organ	all reg. /%		noRIR /%	
	$(u_{D,av})$	$(u_{D,1\%})$	$(u_{D,av})$	$(u_{D,1\%})$
Bladder	12 ± 14 *	21 ± 18 *	13 ± 14 *	23 ± 19 *
Bowel	8 ± 5	13 ± 6	8 ± 5	13 ± 7
Canal anal	17 ± 16	18 ± 16	17 ± 19	18 ± 18
Cauda equina	3 ± 3	6 ± 5	3 ± 3	6 ± 5
Left kidney	6 ± 5	12 ± 15	7 ± 5	13 ± 17
Right kidney	9 ± 7	14 ± 10	9 ± 8	14 ± 10
Left plexus	3 ± 3	6 ± 2 *	3 ± 3	7 ± 2 *
Right plexus	4 ± 2 *	9 ± 5	4 ± 3 *	10 ± 5
Rectum	10 ± 6	19 ± 9	10 ± 6	20 ± 9
Urethra	4 ± 5	10 ± 5 *	4 ± 5	10 ± 6 *
Body contour	7 ± 3 *	11 ± 5	5 ± 3 *	9 ± 6
PTV1	4 ± 4	9 ± 8	5 ± 5	10 ± 8

Table 3.7: Mean ± std of $u_{D,1\%}$ and $u_{D,av}$ for every organ

Significant differences between calculation methods were found for both $u_{D,1\%}$ and $u_{D,av}$ in the bladder (Table 3.8), only in $u_{D,1\%}$ for the left lumbar sacral plexus and the urethra, and only in $u_{D,av}$ for the right lumbar sacral plexus and the body contour.

Organ	$u_{D,av}$	$u_{D,1\%}$
Bladder	0.028	0.008
Left plexus	0.061	0.038
Right plexus	0.019	0.092
Urethra	0.239	0.041
Body contour	0.014	0.083

Table 3.8: p-values for $u_{D,1\%}$ and $u_{D,av}$ between all reg. and noRIR calculations

Most importantly, dosimetric uncertainties will have an impact on the patient's safety only in the regions where the re-irradiation will take place. Table 3.9 presents the u_D of the PTV1s (PTV with the highest dose when there were multiple PTVs for the same treatment) of the second treatment, and it can be seen that the values vary considerably from one patient to another.

Patient	2219	2281	2282	2319	2339	2390	2419	2551	2678	2694
$u_{D,av}$ /%	7.13	1.67	1.83	1.54	9.01	0.82	13.90	0.30	3.38	2.82
$u_{D,1\%}$ /%	10.02	3.40	12.00	3.06	11.97	1.62	22.87	0.57	22.12	6.82

Table 3.9: RSD values of the PTV1 of the second treatment, all reg. calculation

4 Discussion

4.1 Segmentations

4.1.1 Structure correspondence

The first and principal observation to discuss is the small quantity of corresponding organs between the manually-segmented and AI-segmented structures. Indeed, only three structures are segmented in the same manner in both methods. It represents less than a third of the list of selected organs (Table 2.1), but furthermore, it is a very limited quantity next to the 104 structures available in TotalSegmentator's segmentation. Hence, this comparison doesn't make use of the complete set of capacities provided by the AI segmentation. It is mainly due to the fact that the focus of TotalSegmentator is the domain of radiology while the ReCare selected organs are very radiotherapy-related, and although radiology and radiotherapy have common imaging modalities and segmentation necessities, they do not focus on the same anatomic structures. Indeed, 18 of the 104 structures segmented by TotalSegmentator are muscles and vascular structures, which segmentation represent a real achievement but are of limited interest in the radiotherapy context. This also explains why the lumbar sacral plexuses are not segmented by TotalSegmentator. They are of interest in radiotherapy because they are made of nerves, which are radiosensitive tissues. However, nerves are not significant to radiography, mainly because nerve damage is usually not visible on a CT scan.

Another challenge emerging when trying to compare these two segmentations has no real link to their segmentation technique, or to their radiotherapy or radiography focus, but is rather linked to a protocol choice. This can be seen for three different structures: spinal cord - cauda equina, colon - rectum, gastrointestinal tract - bowel.

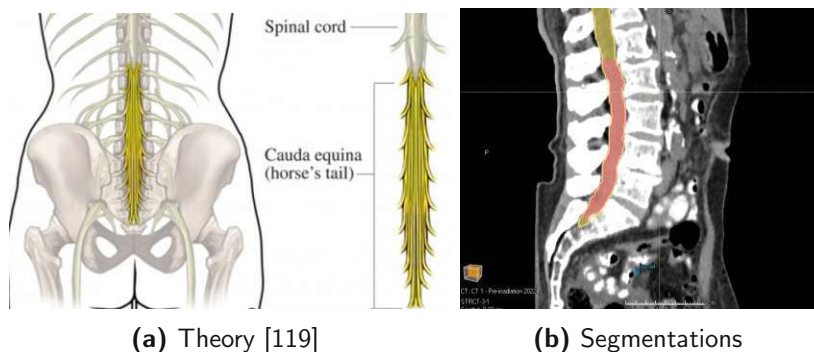


Figure 4.1: Difference between spinal cord and cauda equina

The cauda equina consists of the nerves located at the end of the spinal cord (Figure 4.1a), and is most likely segmented in the ReCare context (red in Figure 4.1b) because of the focus in the pelvic region. On the contrary, in TotalSegmentator, it is segmented as part of the spinal cord (yellow on Figure 4.1b). The same happens for the rectum (blue in Figure 4.2b), which is part of the TotalSegmentator’s colon delineation (yellow in Figure 4.2b).

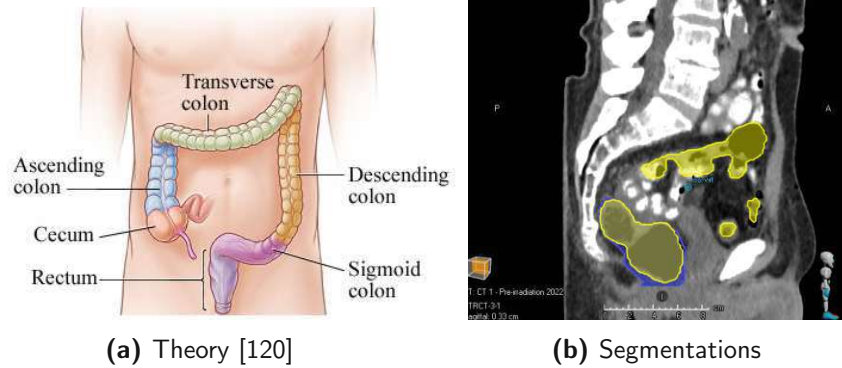


Figure 4.2: Difference between colon and rectum

The ReCare segmentation chose to use a broad delineation of the bowel (red in Figure 4.3), and then segment separately the rectum and anal canal. On the contrary, the TotalSegmentator splits the bowel into three different segments: the duodenum (green in Figure 4.3), the small bowel (purple), and the colon (yellow). The rough contour of the bowel was chosen in the ReCare trial because of the difficulty to identify precisely the boundaries of the organs, but also because of the challenge it opposes in registration [97]. Because of the important magnitude of the anatomical changes in the bowel and of its special shape, a loop-to-loop registration is complicated.

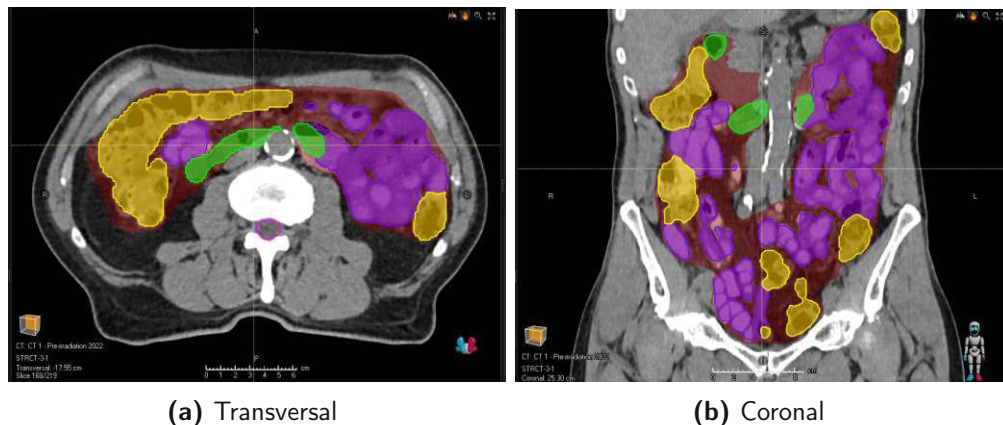


Figure 4.3: Differences in bowel delineation

The only evaluation available for this organ comparison is visual inspection. Hence as it can be seen in Figure 4.3, the rough delineation of the ReCare bowel includes the three different AI-structures. Moreover, some space is included in the ReCare bowel that does not belong to any of the AI-organs. Depending on the anatomical location, it can be explained either by a too broad ReCare delineation or a too tight AI-segmentation, confirming that the ReCare decision is a more cautious solution.

As the bones were identified to sometimes undergo unwanted deformation in the Cont-ROI registrations, it is interesting to see that TotalSegmentator is capable of segmenting the skeleton bone by bone. Although bone segmentation is not the most challenging task, given that bones are easy to segment through thresholding, AI segmentation provides a considerable time and resource advantage. It is faster and simpler than manual thresholding in RayStation (which was done when bones were used as controlling ROI), as well as a complete anatomical knowledge. Moreover, making use of some selected bones as controlling ROIs rather than the whole skeleton could also give a better outcome.

4.1.2 Segmentation performance

The initial and general observation upon reviewing the results is the very high similarity between the two segmentation methods. Moreover, the variations in the similarity metrics are very low.

The kidneys especially exhibit high DSCs and low standard variations. This can be due to many factors, such as their very specific shape, their low inter-patient variability in volume and contour, as well as a good contrast to their neighboring tissues (visible in Figure 4.4). It is indeed usual for kidneys to exhibit good segmentation results [121, 122]. On the contrary, kidneys exhibit the highest HD values along with very low variability. Figure 4.4 demonstrates that the cause of the difference of performance between DSC and HD is caused by the inclusion, or not, of the renal pelvis in the kidney delineation.

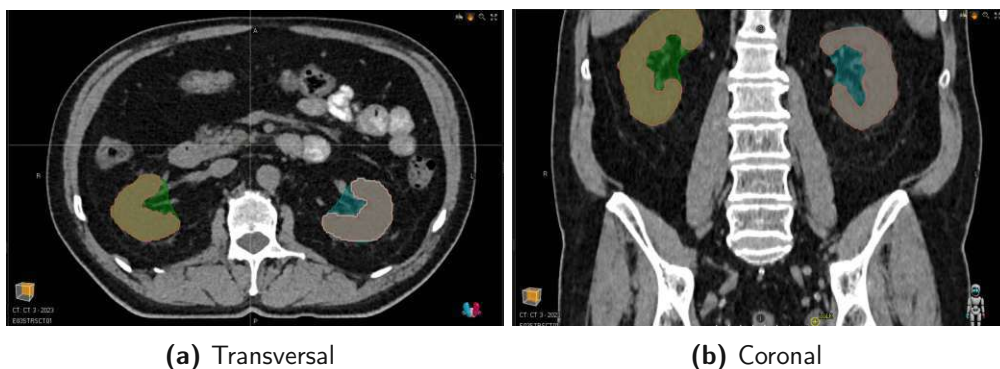


Figure 4.4: Differences in kidneys delineation

ReCare delineation guidelines include the renal pelvis (blue and green in Figure 4.4), while TotalSegmentator does not (orange and pink). Indeed, the HD measures will be sensitive to differences in contour, which does not impact the DSC to the same extent as long as the volumes overlap. It also explains why the manual segmentation exhibits a bigger segmentation volume than the AI-segmentation in Figure 3.3. The difference in volume between the two kidneys could be explained by the fact that the left kidney is positioned slightly higher than the right one and is more likely to be cut depending on the CT's field of view.

The bladder also exhibits a better performance in the DSC than in the HD. Here, it is because the neighboring organs play an important role in its segmentation. Indeed, depending on how the bowel (or small bowel for TotalSegmentator) is delineated, it could change the decision of where the bladder's contour starts, as it wouldn't be realistic to superpose both organs' segmentations (Figure 4.5a & 4.5b). Moreover, TotalSegmentator also delineates the prostate, such structure will also change the contour of the bladder (Figure 4.5b). As the two segmentation methods do not segment the same structures, the impact of the neighboring organs on the bladder's contour are predisposed to be different. Because the relative positions of organs differ for each patient and each CT, the bladder's HD values show significant variability. However, these delineation differences do not generate a significant difference in segmented volumes (Figure 3.3).

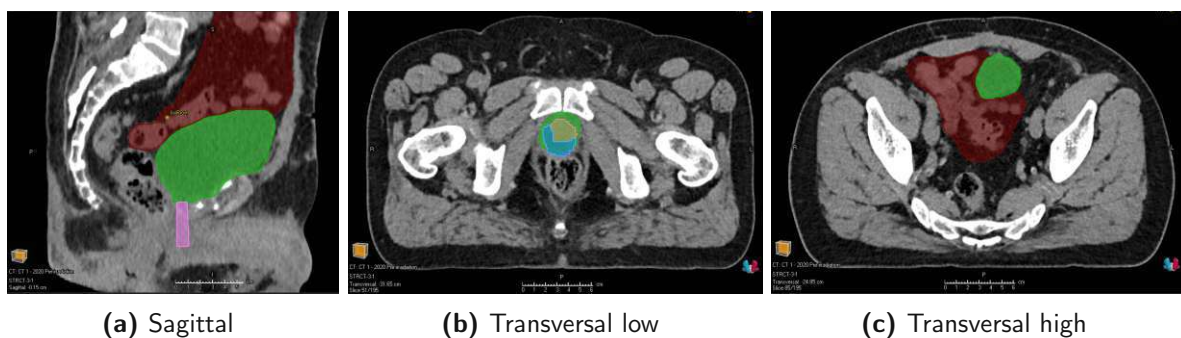


Figure 4.5: Influences on bladder delineation

It is important to keep in mind that the AI segmentation of the rectum and of the cauda equina were not direct imports of 3D Slicer, which means that the comparison is biased. For the cauda equina, the modifications are only done with the ROI algebra tool in RayStation. It means that the length of the pseudo-AI organ is determined by the length of the ReCare cauda equina (Figure 4.1b) and not the TotalSegmentator's segmentation or protocol. However, it also means that the significant difference in volume segmentation relates to the thickness of the delineation rather than its length, and is therefore a difference due to the segmentation method.

For the rectum, two factors adding subjectivity are at play. First, both contours (Figure 4.6) were examined slide by slide to identify where modifications were needed to adapt the colon delineation to the rectum's. Once identified, the ReCare segmentation was hidden to minimize direct influence from the manual segmentation. The second factor is that the modifications made with the brush tool were made without professional segmentation or anatomical expertise.

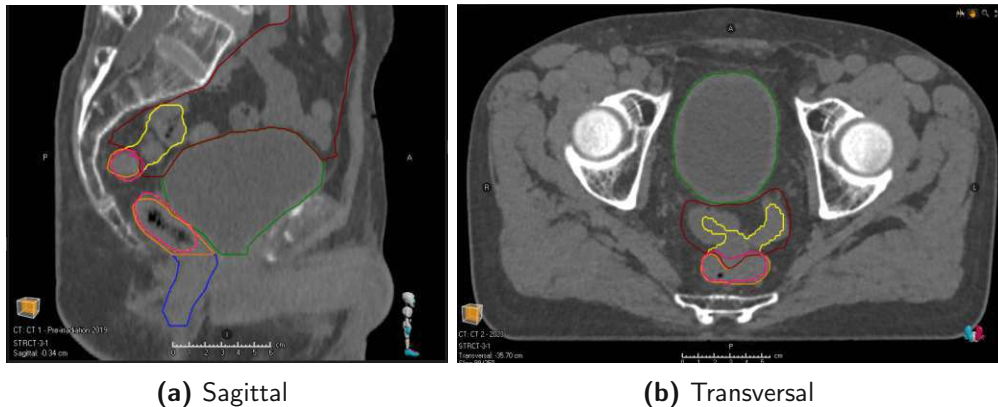


Figure 4.6: Pseudo-AI rectum delineation process, with ReCare rectum in orange, Slicer colon in yellow, and pseudo-AI in pink

The delineation of the anal canal can be seen (in blue in Figure 4.6a) as a continuation of the rectum, which is an additional segmentation difference. Since the ReCare rectum was delineated with the gastrointestinal tract considered as continuous, its end will not be delineated in the same way as it would be if it was handled as a terminal structure, as done in TotalSegmentator's colon segmentation. It is also the location where most of the volume difference originates from.

4.1.3 Outlook and limitations

In general, the performance of the AI-powered segmentation is very similar to the manual one. However, this statement is based only on the five structures that it was possible to analyze. This lack of correspondence in the segmented structures limits its utilization as QA tool in the ReCare trial. Only three organs could be used as such, as the pseudo-AI organs would ask for too much time and subjectivity for a QA task.

It is also important to stress the fact that the great theoretical time gain that the AI segmentation can offer, should not be taken for granted. Indeed, in this thesis, the personal computer used to perform the AI-powered segmentations was not ideal to benefit from it.

With a Nvidia Quadro P520 GPU rather than the RTX 3090 used to give the reference runtimes of a few minutes (Table 2.2), and the Intel Core i7-8565U 1.80 GHz CPU instead of the i9 3.5 GHz, the computation times were significantly higher. Indeed, computing a "whole body" segmentation on an image of medium size on the computer described above took between two and three hours. Moreover, as it requires intensive computer capacities, no other tasks could be performed on the computer in the meantime. Thanks to the Python console embedded in 3D Slicer, some parameters can be changed to have a more efficient segmentation, like the selection of the structures to segment beforehand, or separating the data in multiple smaller datasets. This requirement of computing power highlights the important dependence on technology and hence the reduced accessibility or plausible usage of this tool.

4.2 Registrations

4.2.1 Controlling structures

The first trend shown in the general statistics (Table 3.4) is that using controlling structures gave significantly better results than using only image information. It can be explained, firstly, by the fact that ANACONDA is then used to its full potential as a hybrid DIR algorithm. Indeed, when controlling structures were used, two terms were added to the non-linear optimization problem of the algorithm: the contour regularization term and the contour matching term. The second aspect of this trend is that the controlling structures can be selected, hence adjusted based on the patient, thus more appropriate to the specificity of each case. This allows to select controlling ROIs because of their relevance, either because they show a significant difference in the two sets (in volume or location), or because of their importance in the treatment, hence need in precise delineation propagation. Figure 4.7 shows a strong amelioration of the delineation propagation (dotted lines) as the bladder (green), bowel (red) and both lumbar sacral plexuses (blue) have been used as controlling ROIs. Some remaining problems can however persist, in this case on the left lumbar sacral plexus.

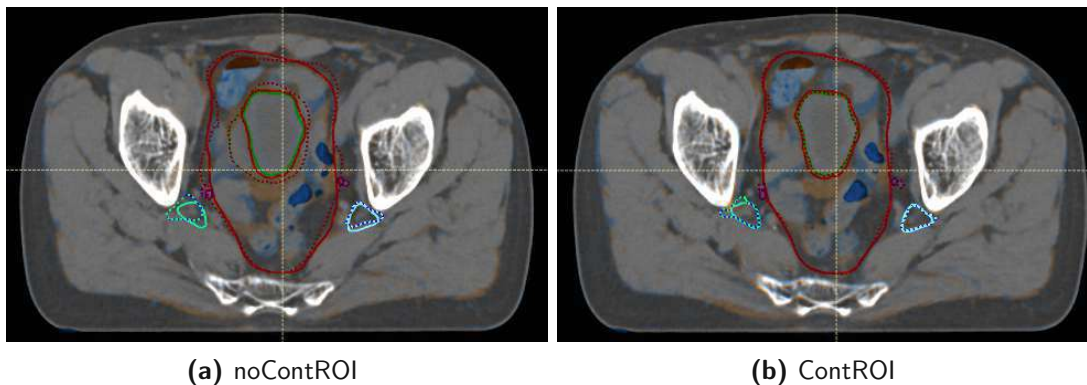


Figure 4.7: Example of contour improvement with controlling ROI (Patient 2281)

Filling organs are problematic because they bring differences that are not due to positioning and, contrary to fractionation, these differences can be voluntary. Indeed, depending on the treatment, a large volume can be required to keep OARs as much away from the high dose target as possible as part of the treatment prescription. This was visible in the important bladder and rectum volume variations as well as in the use of rectal balloons in some patients. The bladder and rectum both show means with a clear better performance by the ContROI method in Figure 3.10.

The bladder showed a significant difference in both metrics as controlling structures were added. This is especially relevant as it is the most volume-varying organ (Figure 4.8 shows an example) and is not the most used ROI as controlling structure. The box plots showed a clear amelioration in the values as well as in the decrease in their spread (Figure 3.6) for the ContROI method. This can be explained by the fact that this organ is very central, touching the rectum, bowel, urethra and bones. Hence, even when it is not used as a controlling structure (either because it added too much constraints to the registration or because it was not an overlap-relevant organ in that case), it will be greatly influenced by the good propagation of the neighboring organs. The results of *Romano et al.* [123] support these values, as they found that the bladder shrinking/enlargement decreases DIR performance when no controlling or only the bladder is used as controlling structure. It confirms the importance of controlling structures and the interdependence of organs.



Figure 4.8: Example of significant bladder volume variation (Patient 2551)

The rectum also showed significant results in its DSC when using controlling structures (Table 3.5), despite different challenging factors. First of all, it is a filling organ, showing a mean volume variation of 24% in this patient cohort (Figure 3.4). Secondly, it is located in the lower pelvic area and is thus very sensitive to positioning changes or weight gain/loss. Therefore, the rectum's registration can suffer from the correction of these changes on top of volume variations. Lastly, it is directly in contact with the bladder and the lower part of the bowel, which both vary a lot in size and location. These challenging factors also highlight why the HD values do not show significant results.

The results obtained here showed the same tendency as the ones presented by *Takayama et al.* [124] for the bladder and the rectum. The prostate and seminal vesicles cannot be compared as they were not delineated in this patient cohort. The fact that *Takayama et al.* have higher DIR DSCs can be explained by the time frame of their study: their DIR was done on fraction CTs rather than re-irradiation ones. The performance of a DIR in the abdominal region can be greatly reduced by the time in between the scans, as the probability of more, and bigger changes increase with time.

4.2.2 Data variability

The cauda equina and sacral lumbar plexuses are ROIs that illustrate very well the focus power of the controlling structures. The three structures showed DSC improvement as controlling structures were added, showing an important increase in DSC (see Figure 3.8a), reaching significantly high scores (>0.95). Because of the geometry and the location of these organs (Figure 4.9), using them as controlling ROIs helps keeping the registrations anatomically realistic. However, their position also mean that if they are not selected in the control list, they are not likely to benefit from improvements in other organs or even rather be penalized by them. It is especially true for the plexuses as they are in contact with other pelvic organs, and it explains why they are the organs most used as controlling structures, alongside the rectum (Figure 3.1).

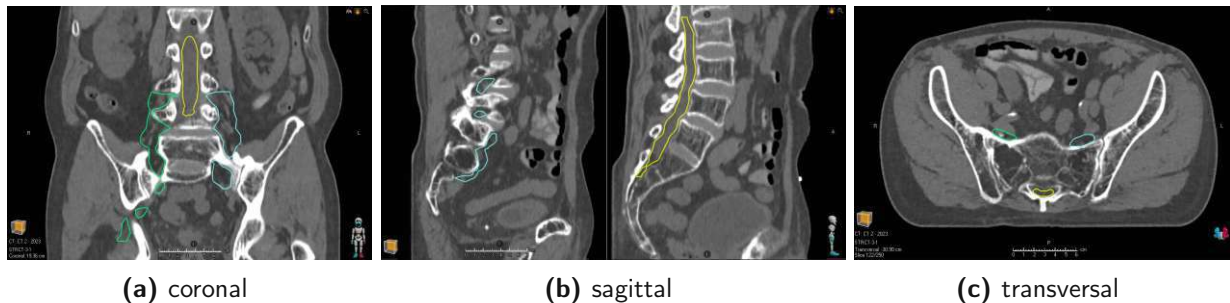


Figure 4.9: Anatomical location of the plexuses (green & blue) and cauda equina (yellow)

Although the p-values comparing the ContROI DSC to the two intensity-based methods' registrations of the plexuses are extremely low, showing a very significant difference, the p-values between noContROI and SDIR were also significant. Median DSC values of the two intensity-based algorithms are considerably distant, furthermore the bigger IQR and longer whiskers of the SDIR data (Figure 3.8) indicate a greater variability compared to noContROI and makes it tend to significance. Indeed, t-tests account for differences in means and in the variability within the datasets.

The impact of the SDIR dataset's variability is also visible in the cauda equina's box plot in Figure 3.9a, that SDIR data shows a lower mean and median, but also a greater variability, which then shows in the statistical results. In this case, significant differences are visible between Elastix and RayStation rather than algorithm types.

However, the right sacral lumbar plexus also showed significant results in its HD values. The difference of results between the two plexuses was unexpected and counterintuitive as the two organs were presented as symmetrical. The asymmetry of the results could be due to the placement of other organs influencing one plexus more than the other.

It illustrates how an organ that is fairly stable in size and location can be influenced when important changes are asked in other organs, in its vicinity. However, the box plot (Figure 3.8) also depicts very well how the variability of data makes it more complex to draw conclusions from statistical analysis.

4.2.3 Bowel

The loose delineation of the bowel allows to achieve good DSC values, already when using the noContROI technique Figure 3.7a. When adding controlling structures, the DSC differences between ContROI and the other methods are even considered significant (Table 3.5) On the contrary, the less the size and shape correspond on both scans, the harder it is to align them. Hence, although ContROI mean and median HD are lower than noContROI, the outliers and the range of the data are still bigger (Figure 3.7b), and no significant difference was found. However, the best HD mean (Figure 3.10a), lowest variability, and lowest outlier, is visible in the SDIR data, highlighting the good performance of the Elastix algorithm in this context.

4.2.4 DSC performance

The following tendency can be observed in the general statistical measures (Table 3.3) and box plot (Figure 3.5): noContROI gives significantly better DSC results than SDIR.

It can be interesting to discuss what could drive such performance difference between algorithms of the same type. The cause doesn't stand on what information the algorithms base their registration on, but rather how they look at it. As both methods are intensity-driven, the difference isn't caused by the registration technique but rather by how the algorithm judges its result. Indeed, both algorithms use different metrics to optimize and verify their registrations.

ANACONDA uses a correlation coefficient, assessing how the two images correlate by comparing their intensity values in a pixel-by-pixel manner. Therefore, it can be sensitive to intensity variations that are not anatomic but due to an inter-modality registration, noise, artifacts or regions that show very homogeneous intensities.

Elastix uses Mattes mutual information, which doesn't rely on a direct intensity match, but rather on the statistical relationship between intensities in the two images. This metric offers a robust performance in regions manifesting a more subtle gradient, which are often located at the organ boundaries.

Offering a good match at the boundaries of the structures has thus a direct impact on the HD. On the contrary, the DSC value does not focus on the exact contour matching, but on the volume overlap.

A trend consistent with this explanation is that the Elastix registration demonstrates smaller HD values and reduced HD variability compared to the noContROI method. Despite being, for example, visible in the bowel's box plot (Figure 3.7) and in the filling organs' means comparison (Figure 3.10), this tendency was never judged significant.

4.2.5 Anal canal and urethra

The anal canal and the urethra are two particularly complicated organs to register. Firstly, because they are located in the very low pelvic area and are thus extremely sensitive to positioning changes or body weight gain/loss. Secondly, the structure matching is complicated because of the small size of the structures. Hence, the differences in intensity taking place around the anal canal make the delineation propagation of all methods equivalent (Figure 3.10). The urethra could be defined as a filling organ because of its volume variation (0.22), however its registration results were not defined as such because the performance is more impacted by its location and reduced size rather than its filling nature.

4.2.6 Outlook and limitations

Hybrid DIR allow to bring subjectivity into the registration with the choice of controlling ROI, e.g. a better handling of filling organs. It was however demonstrated that the location of certain organs makes it impossible even for the best performing algorithm to ameliorate the delineation propagation. It was shown that the similarity metric used in the algorithm had an impact on the its performance, depending on the metric used to judge said performance.

It is important to emphasize the low number of patients, which undoubtedly impacts the results, particularly the statistical analyses. Furthermore, in the case of the urethra, the limited sample size means that when outliers have to be removed, the sample falls below ten, which reduces the power of a statistically analysis.

4.3 Dose mapping

Dose distributions are warped using registrations that align two CTs because it is assumed that the CTs and dose distributions are spatially correlated. However, as explained before, there is no registration that proves to be fully geometrically satisfying. Therefore, the mean dose file represents the best estimate as it compiles all of the selected registrations, hence combining the advantages (and disadvantages) of every strategy. It is done in that manner because there is no ground truth in the matter of dose deformation, and the result cannot be validated against an expectation. In the way they were calculated in this thesis' context, dose uncertainties can be defined as the amount of variation of the mean dose of all registrations, expressed in the form of standard deviation. However, a registration that would present no geometric uncertainties (highly unlikely), would not lead to the absence of dose uncertainties. In this context, an absence of dose uncertainties would be caused by an exact match of the five registrations used to generate the mean dose file.

As geometric uncertainties are introduced by the registration, it is commonly understood that geometric uncertainties are correlated to dosimetric uncertainties [100, 125]. However, the relation between these two different types of uncertainties is neither direct nor linear. Dose uncertainties are caused by a combination of geometric uncertainties, dose gradients, and/or dose magnitude. The extent of the dose uncertainties also depend greatly on this combination of factors. In other words, dose distribution can change the dosimetric relevance of registration errors.

This combination of factors asserts the assumption that a registration judged as geometrically good cannot be straightforwardly assumed to be good for dose deformation. Moreover, this implies that registration should be approached with an awareness of what dose warping could require. Acknowledging dose warping in a registration is only possible when using a hybrid algorithm, as it allows to generate an optimal patient-specific registration. Indeed the selection of controlling ROIs can be done by considering the dose distribution. Furthermore, the level of required accuracy depends on the dose distribution, as a poor registration has no clinical consequence in a homogeneous dose distribution.

4.3.1 Body contour

The uncertainties at the contour of the body are very consistent as they were identified in eight out of ten patients. The second set of MEAN DOSE and STD DOSE files calculated without the RIR highlights one of the main difference between RIR and DIR methods: all DIR methods used in this work have a similar performance of contour delineation propagation, while the RIR does not correct for it.

This difference is visible in Figure 3.15 showing the standard deviation of both all reg and noRIR calculations, and their difference in magnitude in Figure 3.15c. A quantitative approach also confirms this observation, as the body contour's $u_{D,av}$ are significantly lower when the RIR is not used in the calculation (Table 3.7), as well as for the bladder, the plexuses, and the urethra.

It is however important to keep in mind that patient safety will depend on the overlap of the two treatments, hence only anatomical and dosimetric changes in dose-overlap areas are of clinical relevance. For example, the dosimetric uncertainties located in the contour were very important in the rigid registration, both in frequency and magnitude, but they are not necessarily problematic in the re-irradiation context. Indeed, although they are of high importance to evaluate the geometric quality of the registration, uncertainties far from the target are insignificant to the patient's safety. Hence, unless the target is at the skin, these dosimetric uncertainties generated by the rigid registration do not disqualify its use. Indeed, the differences between the two calculation methods were not found significant for the PTV (Table 3.7).

In the patient cohort, only one case can be identified as sensitive to contour variations. As the patient underwent his first treatment in 2013, the dose distribution is characteristic for 3DCRT, i.e. steep gradients and high dose are located at the body contour as visible in Figure 4.10b. Hence, the impact of the contour registration on the dosimetric uncertainties are due to the radiation technique rather than to the position of the target. Moreover, the treatment targets of other patients are either situated near a bony structure or closer to the core of the body, making them minimally influenced by variations at the surface.



Figure 4.10: Importance of good contour match for patient 2282

4.3.2 Gradients

A dose gradient can be defined as a dose difference, divided by the distance between two isodose curves. Therefore, the smaller this distance is, the steeper the gradient, and these quick transitions generate what is referred to as a heterogeneous dose distribution. Usually, the isodose curves are close to each other in high dose regions and then become more spaced out as they move away from the high dose target. Hence, steep dose gradients are typically situated in high dose areas. However, the opposite is not true. It cannot be said that homogeneous regions, thus with low dose gradient, are only situated in low dose areas. A homogeneous dose distribution area is often desired in PTVs. It can of course also happen in the low dose areas but the dose magnitude is not the important factor but rather the homogeneity of the distribution. The magnitude of the dose in a low gradient becomes especially significant at the boundary of the isodose, geometric variations at this location will create dosimetric uncertainties.

Indeed, Figure 4.11 illustrates the impact that the gradients can have on the dosimetric uncertainties. In an homogeneous dose distribution like the 70% surface in green in Figure 4.11b and delineated by its red isodose curve, the uncertainties are very low (Figure 4.11a), although the dose is high. Then, between the 70% isodose in red and the 40% isodose in orange, the gradient is quite steep, and important uncertainties can be accounted for. In the lower dose regions, the uncertainties are visible around the 30% isodose curve in pink, and at the contours where the RIR causes geometric variations.



(a) Standard deviation

(b) Mean

Figure 4.11: Impact of dose homogeneity on dosimetric uncertainties. Patient 2219

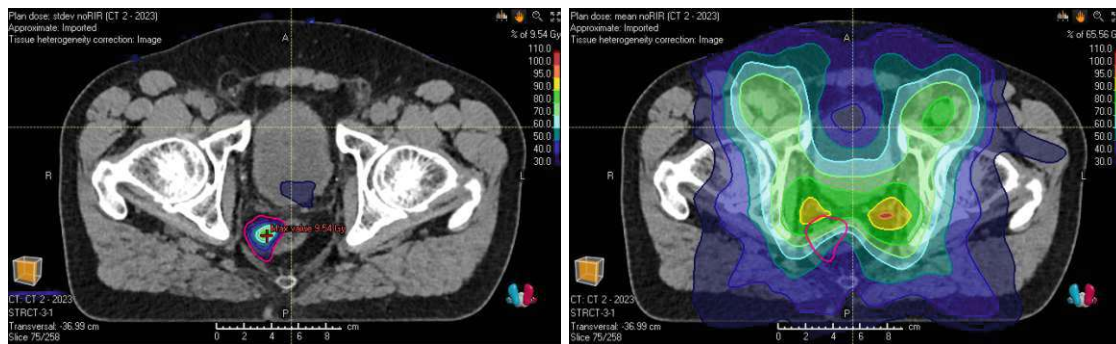
A heterogeneous distribution of dose must be combined with geometric uncertainties to generate dosimetric uncertainties. Although the regions presenting anatomic differences can be identified, predicting the precise location of geometric uncertainties is complicated because it depends on how the algorithm chooses to deform these regions. The geometric differences can be due to the different ways that algorithms handle challenging regions with no controlling structures as in Figure 4.12, or in regions with controlling regions as in Figure 4.13.



(a) Standard deviation

(b) Mean

Figure 4.12: Dosimetric uncertainties due to intensity-based geometric uncertainties in steep dose gradient area. Patient 2694



(a) Standard deviation

(b) Mean

Figure 4.13: Dosimetric uncertainties due to controlling structures-generated geometric uncertainties in steep dose gradient area. Patient 2551

Although steep dose gradients are located relatively close to the target, the shape of the dose distribution, and hence the exact contour of dose gradients are very case-specific and can be considerably far from the target depending on the shape of the isodose surface. Moreover, the dose gradients are non-uniform even along the same two isodose curves. The distance to high dose was taken into account when selecting the controlling structures for the hybrid algorithm, but not where the steep gradients were located.

Registration variations in uniform dose distributions result in small dose errors, while the same geometric variations occurring in regions with steep dose gradients lead to important dosimetric uncertainties. The impact of geometric variations on the dose accuracy depends on the gradient density of the area. As there are less dose gradients further away from the high dose target, dosimetric uncertainties also indirectly depend on the dose magnitude in the area of the geometric errors. If it were to define an acceptable geometric uncertainty that would ensure dosimetric uncertainties to stay under a safety threshold, it could be stated that the acceptable geometric uncertainty would vary along the anatomy.

4.3.3 Geometric uncertainties

Geometric uncertainties arise from variations in how the different registration strategies handle the anatomic differences between the two CT scans. The registrations used to generate the MEAN DOSE and STD DOSE files can be put in three different strategy categories: the RIR, the image information based DIRs, and the hybrid DIRs. Eventually, the variations in how each category of strategy performs, particularly in challenging areas, cause the observed geometric uncertainties. These can be quantified in different ways such as low DSCs, high HDs, or the statistical analysis of these metrics between the different methods (Table 3.5 & 3.6), but also in the volume variation of the organ (Figure 3.4).

ROIs with the highest u_D mean can be identified in Table 3.7. Although dose uncertainties are always multifactorial and case-specific, when ROIs have a high mean u_D , it does imply that they have an inclination for geometric variations. The three organs exhibiting the highest RSD are (in every category) the bladder, the anal canal, and the rectum. These ROIs are all filling organs, which are known to be challenging areas. Their geometric uncertainties are quantified in different ways: the bladder has showed significant differences between registration methods in both metrics, while the anal canal exhibits a low DSC, and the rectum presents a significant DSC difference in the registration performance.

However, as presented in Figure 3.1, the organs most used as controlling structures are not necessarily the ones noted as most challenging or exhibiting the biggest volume variation. Indeed, as the anal canal was only used as a controlling structure in one patient, it can therefore be concluded that the high dosimetric uncertainties in this region are due to intensity-based geometric variations. On the contrary, the rectum was used as a controlling structure in nine patients, its high dosimetric uncertainties can thus be qualified as linked with controlling structures generated geometric variations. Controlling structures can introduce geometric uncertainties because they stress on the registration of certain ROIs delineation that are not otherwise in focus. It also puts the propagation of these ROIs delineation in higher priority than deformations that would be solicited by image information.

The case of the anal canal is special because of the particularly outstanding RSD. Many reasons can explain this high variation numbers. First of all, it is a small, filling organ, and it displays big position variations between the two CTs. Therefore, it is very complicated to offer a good registration for the anal canal. Moreover, it is located near bony structures and in the very low pelvic region, the algorithms thus don't have a lot of flexibility to offer a good geometric outcome. The similarity metrics of the anal canal, that can be seen in Figure 3.10, clearly show that the different registrations cannot perform differently in that region.

Moreover, because of the targets treated in this patient cohort, the anal canal was often situated at the border of an important isodose curve. It is also because of these dose distributions that the urethra does not exhibit the same u_D as the anal canal despite being in the same anatomic region. Indeed, the dose distribution overlapping the urethra is usually fairly homogeneous, while the anal canal is found in a gradient area. This difference can even be said to be significant for D_{av} values for both all reg. and noRIR calculations, along with the other organs exhibiting low dose variation such as the cauda equina, and both sacral lumbar plexuses (signified with stars in Table 3.7). These organs, conversely to the urethra, exhibit good geometric performances.

In the context of $u_{D,1\%}$ values, which indicate the presence of uncertainty hotspots, the same trend does not apply, here only a significant difference between the bladder and the cauda equina was observed. The bladder had the highest $u_{D,1\%}$, while the cauda equina had the lowest value. Although the cauda equina showed better DSC and HD measures than the bladder, this alone does not account for the difference, as other organs show both superior and inferior similarity metrics than this pair. Moreover, both the bladder and the cauda equina showed significant differences between the registration methods. Thus, the dose distribution plays a key role in the impact of geometric uncertainties on $u_{D,1\%}$.

4.3.4 Systematic errors

As presented in the Material & Methods section, the data used for analysis has undergone many steps of import and export from and to RayStation, 3D Slicer and Python. It was also transformed spatially either by RIR or DIR. Some accuracy has been lost in this process, principally caused by interpolation. There is of course the interpolation mentioned in the resampling of the SDIR dose file in Python. The dose uncertainties caused by this interpolation can be quantified with the checkDIR dose file that contains the resampled Slicer DIR dose distribution, and is visible in Figure 4.14.

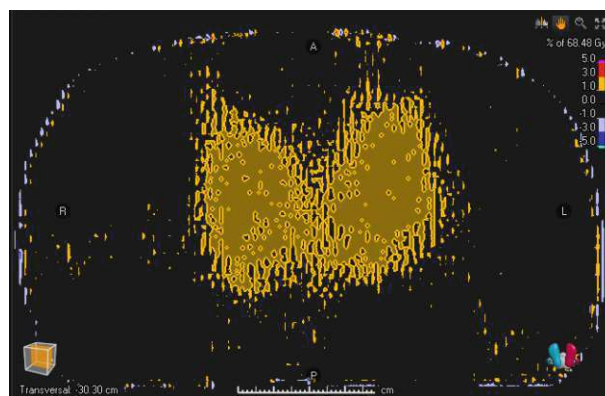


Figure 4.14: Dose difference between the original SDIR and checkSDIR files, Patient 2281

There are however many interpolation steps that are taking place in the background of the TPS and are not explicitly communicated to the user. An aspect that the TPS struggles to handle is the rotation of the dose field. Indeed RIR and DIR can use 3D rotations, which results in a change in spatial orientation, despite having the same dose file of origin. When such a tilted file is exported from RayStation, it is automatically straightened. This implies that if the file is re-imported without undergoing any modification, the imported file will still exhibit differences from the original dose distribution as visible in Figure 4.15.

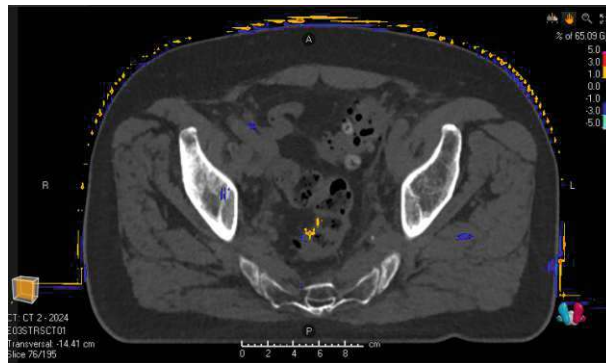


Figure 4.15: Dose difference between the original Wall file and the exported and directly re-imported Wall file, Patient 2694

This is a limitation of RayStation that could not be improved with in this thesis. These type of introduced uncertainties should be mentioned, although they remain small in the context of the observed dosimetric variations.

4.3.5 Second treatment

When all of these observations are put back into the context of re-irradiation, the safety of the patient eventually depends on the dose uncertainties in the high dose region of the second treatment. To illustrate this aspect, $u_{D,1\%}$ and $u_{D,av}$ from the PTV1 from the second treatment for each patient were retrieved and presented in Table 3.9, they were also used for statistical analysis in Table 3.7.

The first observation that can be made from these results is the important variation from one patient to another. This is due to the fact that every factor that can influence dose uncertainties is different for each patient. The geometric uncertainties are different because the anatomical changes between the scans were different. The dose distributions are different because every patient has a different first treatment. Finally, the location of the PTV1 is also different for every patient as it depends on their individual second treatment. It can be seen that the lowest PTV1 u_D is lower than the lowest ROI u_D (Table 3.7) for both maximal and average dose uncertainties. One of the reason for that is the fact that the PTV values are not a mean but individual values.

However, it can be argued that the RSD of the PTVs are quite low because they are located in regions of low primary dose and low geometric variations. Indeed, most of the re-irradiation PTVs have lymph nodes or bones as targets. Bones or targets located near bony structures are known to vary in position only slightly with time. Moreover, primary treatments commonly have targets that are more centrally located, such as the prostate bed, which puts the secondary PTVs far from the high dose of the first treatment. It is however essential to keep in mind that these observations are based only on this specific patient cohort, and could vary greatly depending on the anatomies of the patients and their treatments.

4.3.6 Outlook and limitations

Dosimetric uncertainties are a complex combination of heterogeneous dose distribution, geometric uncertainties and dose magnitude. Although the different factors can be identified, it is complicated to predict, particularly because the geometric uncertainties do not necessarily manifest in (or only in) challenging regions. It is also important to keep in mind that the dosimetric uncertainties are of importance only in specific regions subject to re-irradiation. Hence, the big variations that were identified at the contours were not found to create significant differences in the organs, were high dose overlap is more likely to take place than at the skin. A limitation of the analysis done in this thesis is the dimension in which the dose distribution was viewed. As visible in every example previously given, the dosimetric uncertainties were evaluated in the transversal plane as shown in Figure 4.16a and 4.16b. However some special cases of high dosimetric uncertainties cannot be explained by the presented factors, and looking at gradients in the other planes could help make sense of it, as exemplified in Figure 4.16d where the largest uncertainty was found in the transversal dose gradient near the field edge.

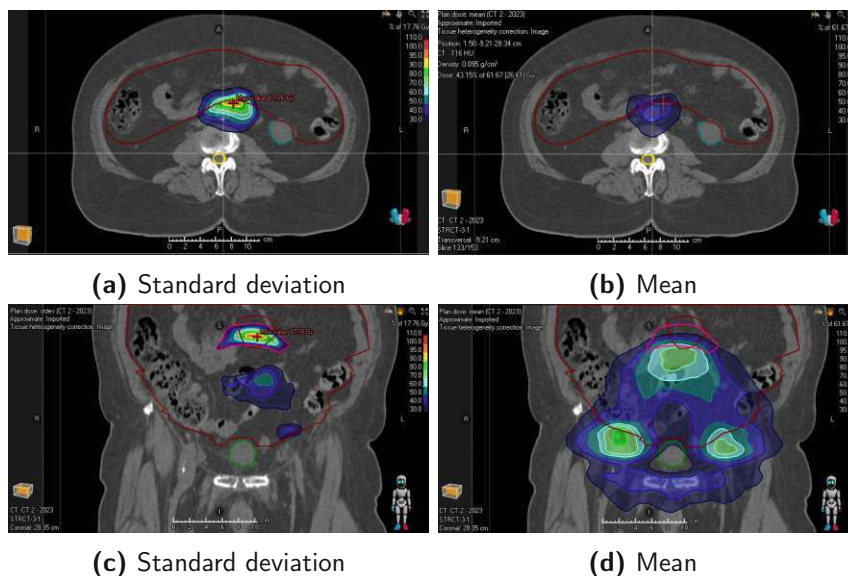


Figure 4.16: Dose distribution in different planes. Patient 2319

5 Conclusion and Outlook

The comparison of manual and AI-powered segmentation resulted in the conclusion that the 3D Slicer module TotalSegmentator is not appropriate to be used as a QA tool for checking the manual segmentation of the ReCare cohort in the pelvic region at the time this work was conducted. Although the results showed a high similarity between the two segmentations, the number of corresponding structures was too low to fulfill this function. The reasons identified for these differences were the radiology focus of TotalSegmentator and some differences in the segmentation protocols. The personal computer's CPU and GPU capacities were identified as a limitation to the theoretical time gain of automated segmentation, highlighting the important dependence of such methods on powerful technology. The modifications made to create pseudo-AI structures were also time consuming and reduced the precision of their similarity metrics. However, if future research focuses on other anatomic regions, TotalSegmentator might be more adequate to perform a QA task there.

The quantitative and qualitative evaluations of the different registration strategies allowed to state that the best results were reached with hybrid DIRs. Using controlling structures offers to the registration the necessary subjectivity to respond to the specificity of each case. The differences between each intensity-based algorithm and the hybrid algorithm were consistent across both DSC and HD metrics, while the two intensity-based algorithms showed significantly different DSC results when tested against each other due to their use of different optimization metrics. Organs offering a challenge to the appropriate performance of the registrations were also identified.

Their challenging characteristic was mainly due to their filling nature, generating important variations of volume and geometry. The specificity of each case, and consequently the important differences between patients, made it unsuitable to generate a general hybrid DIR methodology that would assure a good performance, hence the selection of controlling structures could vary depending on the anatomical changes that took place between the two treatments. To continue this work, more patients should be added to the cohort in order to strengthen the results and confirm the trends identified in this thesis. In a second stage, other anatomic regions need to be investigated, where algorithms might perform differently.

The assumption made, as the dosimetric uncertainties in dose mapping were calculated with previously performed registrations, was that there is a spatial correlation between anatomy and dose distribution. Assuming geometric correlation between dose distribution and anatomy also means that geometric uncertainties are linked to dosimetric uncertainties. It was however observed that dosimetric uncertainties are generated by a complex combination of geometric uncertainties, a steep gradient dose distribution, and a certain dose magnitude. The geometric variations causing dosimetric uncertainties were found to be a consequence of the use of controlling structures in certain registrations, the different handling of intensity-based variations (e.g., anal canal) between registrations, and the absence of contour matching in the RIR. It was also found that the quantification of dosimetric uncertainties was especially important for patient safety in regions of re-irradiation. PTVs, as part of the overlap region, were used to quantify these critical dosimetric uncertainties, particularly due to the high doses involved. The absence of the RIR in the dose uncertainties calculation was found to be significant only for some organs and the body contour, but not for the PTVs. The communication between 3D Slicer, RayStation, and Python appeared to be complicated, adding time-consuming steps as well as interpolation errors. Additional work needs to focus on the resampling errors caused by the change in dimension of the SDIR file. More patients could confirm the results, as well as offer more special cases that could raise interest in other factors to dose variations not yet identified. For a better prediction of dosimetric uncertainties, steep gradients could also be identified in the first steps of the registration workflow and taken into account when selecting the controlling structures of the hybrid DIRs.



Die approbierte gedruckte Originalversion dieser Diplomarbeit ist an der TU Wien Bibliothek verfügbar
The approved original version of this thesis is available in print at TU Wien Bibliothek.



Die approbierte gedruckte Originalversion dieser Diplomarbeit ist an der TU Wien Bibliothek verfügbar
The approved original version of this thesis is available in print at TU Wien Bibliothek.

Bibliography

1. *Ionizing radiation* en. Page Version ID: 1227019209. June 2024. https://en.wikipedia.org/w/index.php?title=Ionizing_radiation&oldid=1227019209 (2024).
2. Murphy, A. *Biomolecular radiation damage | Radiology Reference Article | Radiopaedia.org* en-US. Oct. 2023. <https://radiopaedia.org/articles/biomolecular-radiation-damage> (2024).
3. Keith, S. *et al.* en. in *Toxicological Profile for Radon* (Agency for Toxic Substances and Disease Registry (US), May 2012). <https://www.ncbi.nlm.nih.gov/books/NBK158792/> (2024).
4. IARC. en. in *Radiation* (International Agency for Research on Cancer, 2012). <https://www.ncbi.nlm.nih.gov/books/NBK304365/> (2024).
5. IAEA. *Equipment* en. Text. Publisher: IAEA. Dec. 2020. <https://www.iaea.org/resources/hhc/medical-physics/radiotherapy/equipment> (2024).
6. Joachim Feger. *X-ray tube | Radiology Reference Article | Radiopaedia.org* June 2024. <https://radiopaedia.org/articles/x-ray-tube-1> (2024).
7. Boyer, A. *et al.* *Basic Applications of Multileaf Collimators* en. Tech. rep. (AAPM, 2001). <https://www.aapm.org/pubs/reports/detail.asp?docid=71> (2024).
8. Knipe, H. *3D conformal radiation therapy | Radiology Reference Article | Radiopaedia.org* en-US. Mar. 2023. <https://radiopaedia.org/articles/3d-conformal-radiation-therapy?lang=us> (2024).
9. Studenski, M. T. *et al.* Intensity-modulated radiation therapy and volumetric-modulated arc therapy for adult craniospinal irradiation—A comparison with traditional techniques. *Medical Dosimetry* **38**, 48–54. ISSN: 0958-3947. <https://www.sciencedirect.com/science/article/pii/S0958394712001021> (2024) (Mar. 2013).
10. Koka, K., Verma, A., Dwarakanath, B. S. & Papineni, R. V. L. Technological Advancements in External Beam Radiation Therapy (EBRT): An Indispensable Tool for Cancer Treatment. *Cancer Management and Research* **14**, 1421–1429. ISSN: 1179-1322. <https://www.ncbi.nlm.nih.gov/pmc/articles/PMC9012312/> (2024) (Apr. 2022).

11. Mott, J. & Daniel, J. Interactions of Electromagnetic Radiation and Subatomic Particles with Matter – Part 1. en. *Clinical Oncology* **33**, 451–454. ISSN: 09366555. <https://linkinghub.elsevier.com/retrieve/pii/S0936655521000479> (2024) (July 2021).
12. Ervin B. Podgorsak. Review of Radiation Oncology Physics: A Handbook for Teachers and Students. en. *Journal of Applied Clinical Medical Physics* **5**, 91–92. ISSN: 1526-9914. <http://www.jacmp.org/archive.php?doi=10.1120%2Fjacmp.2021.25315> (2024) (July 2004).
13. Harry Marshall. *Figure 1.3: Dominant photon/matter interactions according to atomic...* en. June 2012. https://www.researchgate.net/figure/Dominant-photon-matter-interactions-according-to-atomic-number-Z-and-photon-energy_fig2_347254387 (2024).
14. Barbara A. Schreiber. *Photoelectric effect | Definition, Examples, & Applications | Britannica* Aug. 2024. <https://www.britannica.com/science/photoelectric-effect> (2024).
15. Raymond Chieng. *Pair production | Radiology Reference Article | Radiopaedia.org* June 2023. <https://radiopaedia.org/articles/pair-production?lang=us> (2024).
16. Engineering LibreTexts. *Compton Effect* en. July 2016. [https://eng.libretexts.org/Bookshelves/Materials_Science/Supplemental_Modules_\(Materials_Science\)/Electronic_Properties/Compton_Effect](https://eng.libretexts.org/Bookshelves/Materials_Science/Supplemental_Modules_(Materials_Science)/Electronic_Properties/Compton_Effect) (2024).
17. Goel, A. *Compton effect | Radiology Reference Article | Radiopaedia.org* en-US. June 2024. <https://radiopaedia.org/articles/compton-effect> (2024).
18. Paul D'Alessandris. *4.3: Pair Production* en. Dec. 2017. [https://phys.libretexts.org/Bookshelves/Modern_Physics/Book%3A_Spiral_Modern_Physics_\(D'Alessandris\)/4%3A_The_Photon/4.3%3A_Pair_Production](https://phys.libretexts.org/Bookshelves/Modern_Physics/Book%3A_Spiral_Modern_Physics_(D'Alessandris)/4%3A_The_Photon/4.3%3A_Pair_Production) (2024).
19. Cancer Research UK. *How cancer can spread* en. Oct. 2014. <https://www.cancerresearchuk.org/about-cancer/what-is-cancer/how-cancer-can-spread> (2024).
20. Cancer Research UK. *How cancers grow* en. Oct. 2014. <https://www.cancerresearchuk.org/about-cancer/what-is-cancer/how-cancers-grow> (2024).
21. IQWiG (Institute for Quality and Efficiency in Health Care). en. in *Informed-Health.org [Internet]* (Institute for Quality and Efficiency in Health Care (IQWiG), Apr. 2022). <https://www.ncbi.nlm.nih.gov/books/NBK279410/> (2024).
22. Hawkes, N. Cancer survival data emphasise importance of early diagnosis. en. *BMJ*, 1408. ISSN: 0959-8138, 1756-1833. <https://www.bmj.com/lookup/doi/10.1136/bmj.1408> (2024) (Jan. 2019).

23. NCI. *The Genetics of Cancer* en. cgVArticle. Archive Location: nciglobal, ncenterprise. Apr. 2015. <https://www.cancer.gov/about-cancer/causes-prevention/genetics> (2024).
24. American Cancer Society. *Genetic Mutations | Types of Mutations* en. Aug. 2022. <https://www.cancer.org/cancer/understanding-cancer/genes-and-cancer/gene-changes.html> (2024).
25. Mayo Clinic. *Cancer treatment - Mayo Clinic* May 2022. <https://www.mayoclinic.org/tests-procedures/cancer-treatment/about/pac-20393344> (2024).
26. NCI. *Surgery for Cancer - NCI* en. cgVArticle. Archive Location: nciglobal, ncenterprise. Apr. 2015. <https://www.cancer.gov/about-cancer/treatment/types/surgery> (2024).
27. Mayo Clinic. *What to know about surgery for cancer* en. Aug. 2022. <https://www.mayoclinic.org/diseases-conditions/cancer/in-depth/cancer-surgery/art-20044171> (2024).
28. Robert Peter Gale. *Radiation Therapy for Cancer - Cancer* en. Sept. 2022. <https://www.msdmanuals.com/home/cancer/prevention-and-treatment-of-cancer/radiation-therapy-for-cancer> (2024).
29. NCI. *Radiation Therapy for Cancer - NCI* en. cgVArticle. Archive Location: nciglobal, ncenterprise. Apr. 2015. <https://www.cancer.gov/about-cancer/treatment/types/radiation-therapy> (2024).
30. American Cancer Society. *Goals of Chemotherapy | How is Chemotherapy Given?* en. Nov. 2019. <https://www.cancer.org/cancer/managing-cancer/treatment-types/chemotherapy/how-is-chemotherapy-used-to-treat-cancer.html> (2024).
31. Robert Peter Gale. *Chemotherapy and Other Systemic Cancer Treatments - Cancer* en. Sept. 2022. <https://www.msdmanuals.com/home/cancer/prevention-and-treatment-of-cancer/radiation-therapy-for-cancer> (2024).
32. NCI. *Chemotherapy to Treat Cancer - NCI* en. cgVArticle. Archive Location: nciglobal, ncenterprise. Apr. 2015. <https://www.cancer.gov/about-cancer/treatment/types/chemotherapy> (2024).
33. Parker, R. Chemotherapy: An Overview. en. *Journal of Biomedical Engineering and Medical Devices* **6**. Publisher: Longdom Publishing S.L, 1–1. ISSN: 2475-7586. <https://www.longdom.org/open-access/chemotherapy-an-overview-87377.html> (2024) (Oct. 2021).
34. American Cancer Society. *Treating Cancer with Immunotherapy | Types of Immunotherapy* en. Dec. 2019. <https://www.cancer.org/cancer/managing-cancer/treatment-types/immunotherapy/what-is-immunotherapy.html> (2024).

35. Memorial Sloan Kettering Cancer Center. *Immunotherapy Cancer Treatment | Memorial Sloan Kettering Cancer Center* en. Aug. 2024. <https://www.mskcc.org/cancer-care/diagnosis-treatment/cancer-treatments/immunotherapy> (2024).
36. Galluzzi, L. *et al.* Classification of current anticancer immunotherapies. *Oncotarget* **5**, 12472–12508. ISSN: 1949-2553. <https://www.ncbi.nlm.nih.gov/pmc/articles/PMC4350348/> (2024) (Dec. 2014).
37. Peterson, C., Denlinger, N. & Yang, Y. Recent Advances and Challenges in Cancer Immunotherapy. *Cancers* **14**, 3972. ISSN: 2072-6694. <https://www.ncbi.nlm.nih.gov/pmc/articles/PMC9406446/> (2024) (Aug. 2022).
38. American Cancer Society. *How Radiation Therapy Is Used to Treat Cancer* en. Dec. 2019. <https://www.cancer.org/cancer/managing-cancer/treatment-types/radiation/basics.html> (2024).
39. NCI. *External Beam Radiation Therapy for Cancer - NCI* en. cgvArticle. Archive Location: nciglobal, ncicenterprise. May 2018. <https://www.cancer.gov/about-cancer/treatment/types/radiation-therapy/external-beam> (2024).
40. American Cancer Society. *External Beam Radiation | Types of External Radiation Therapy* en. Feb. 2023. <https://www.cancer.org/cancer/managing-cancer/treatment-types/radiation/external-beam-radiation-therapy.html> (2024).
41. NCI. *Brachytherapy for Cancer - NCI* en. cgvArticle. Archive Location: nciglobal, ncicenterprise. May 2018. <https://www.cancer.gov/about-cancer/treatment/types/radiation-therapy/brachytherapy> (2024).
42. Mayer, C., Gasalberti, D. P. & Kumar, A. eng. in *StatPearls* (StatPearls Publishing, Treasure Island (FL), 2024). <http://www.ncbi.nlm.nih.gov/books/NBK562190/> (2024).
43. Cancer Research UK. *What is brachytherapy?* en. Nov. 2020. <https://www.cancerresearchuk.org/about-cancer/treatment/radiotherapy/internal/radioactive-implant-treatment/what-is--brachytherapy> (2024).
44. Simon Caulton. *File:Cell cycle simple.png - Wikipedia* en. Aug. 2013. https://commons.wikimedia.org/wiki/File:Cell_cycle_simple.png (2024).
45. Baeyens, A. *et al.* en. in *Radiobiology Textbook* (ed Baatout, S.) 25–81 (Springer International Publishing, Cham, 2023). ISBN: 978-3-031-18810-7. https://doi.org/10.1007/978-3-031-18810-7_2 (2024).
46. Iowa State University. *Nondestructive Evaluation NDE Engineering : Radiation Safety* <https://www.nde-ed.org/NDEEngineering/RadiationSafety/theory/radiosensitivity.xhtml> (2024).

47. Benedict, S. H. Review of Radiation Oncology Physics: A Handbook for Teachers and Students. en. *Journal of Applied Clinical Medical Physics* **5**, 91–92. ISSN: 1526-9914. <http://www.jacmp.org/archive.php?doi=10.1120%2Fjacmp.2021.25315> (2024) (July 2004).
48. Sciacca, F. *Law of Bergonié and Tribondeau | Radiology Reference Article | Radiopaedia.org* en-US. May 2024. <https://radiopaedia.org/articles/law-of-bergonie-and-tribondeau> (2024).
49. OMP. *Principles of Radiobiology | Oncology Medical Physics* en-US. <https://oncologymedicalphysics.com/principles-of-radiobiology/> (2024).
50. Amin I. Kassis. *Figure 6 Mammalian cell survival curves after high-and low-LET...* en. Oct. 2008. https://www.researchgate.net/figure/Mammalian-cell-survival-curves-after-high-and-low-LET-irradiation-With-high-LET_fig6_23133166 (2024).
51. Lobo, V., Patil, A., Phatak, A. & Chandra, N. Free radicals, antioxidants and functional foods: Impact on human health. *Pharmacognosy Reviews* **4**, 118–126. ISSN: 0973-7847. <https://www.ncbi.nlm.nih.gov/pmc/articles/PMC3249911/> (2024) (2010).
52. Ng, W.-L. *et al.* Molecular mechanisms involved in tumor repopulation after radiotherapy. *Translational cancer research* **2**, 442–448. ISSN: 2218-676X. <https://www.ncbi.nlm.nih.gov/pmc/articles/PMC4293635/> (2024) (Oct. 2013).
53. Straub, J. M. *et al.* Radiation-induced fibrosis: mechanisms and implications for therapy. *Journal of cancer research and clinical oncology* **141**, 1985–1994. ISSN: 0171-5216. <https://www.ncbi.nlm.nih.gov/pmc/articles/PMC4573901/> (2024) (Nov. 2015).
54. Fijardo, M. *et al.* The clinical manifestations and molecular pathogenesis of radiation fibrosis. English. *eBioMedicine* **103**. Publisher: Elsevier. ISSN: 2352-3964. [https://www.thelancet.com/journals/ebiom/article/PIIS2352-3964\(24\)00124-5/fulltext](https://www.thelancet.com/journals/ebiom/article/PIIS2352-3964(24)00124-5/fulltext) (2024) (May 2024).
55. Majeed, H. & Gupta, V. eng. in *StatPearls* (StatPearls Publishing, Treasure Island (FL), Aug. 2023). <http://www.ncbi.nlm.nih.gov/books/NBK563259/> (2024).
56. Yusuf, S. W., Sami, S. & Daher, I. N. Radiation-Induced Heart Disease: A Clinical Update. *Cardiology Research and Practice* **2011**, 317659. ISSN: 2090-0597. <https://www.ncbi.nlm.nih.gov/pmc/articles/PMC3051159/> (2024) (Feb. 2011).
57. Jia, A. Y. & Viswanathan, A. N. Vaginal necrosis: A rare late toxicity after radiation therapy. *Gynecologic oncology* **160**, 602–609. ISSN: 0090-8258. <https://www.ncbi.nlm.nih.gov/pmc/articles/PMC8817784/> (2024) (Feb. 2021).

58. Delanian, S., Lefaix, J.-L. & Pradat, P.-F. Radiation-induced neuropathy in cancer survivors. English. *Radiotherapy and Oncology* **105**. Publisher: Elsevier, 273–282. ISSN: 0167-8140, 1879-0887. [https://www.thegreenjournal.com/article/S0167-8140\(12\)00462-8/fulltext](https://www.thegreenjournal.com/article/S0167-8140(12)00462-8/fulltext) (2024) (Dec. 2012).
59. Lynne Eldridge. *Long-Term Effects of Radiation Therapy Everyone Should Know* en. Section: Verywell. Jan. 2022. <https://www.verywellhealth.com/long-term-side-effects-of-radiation-therapy-2249293> (2024).
60. Macmillan Cancer Support. *Managing bladder late effects - Macmillan Cancer Support* en. July 2024. <https://www.macmillan.org.uk/cancer-information-and-support/impacts-of-cancer/managing-bladder-late-effects> (2024).
61. American Cancer Society. *Late and Long-term Effects of Cancer* en. May 2024. <https://www.cancer.org/cancer/survivorship/long-term-health-concerns/long-term-side-effects-of-cancer.html> (2024).
62. Fuccio, L., Guido, A. & Andreyev, H. J. N. Management of Intestinal Complications in Patients With Pelvic Radiation Disease. English. *Clinical Gastroenterology and Hepatology* **10**. Publisher: Elsevier, 1326–1334.e4. ISSN: 1542-3565, 1542-7714. [https://www.cghjournal.org/article/S1542-3565\(12\)00900-7/fulltext](https://www.cghjournal.org/article/S1542-3565(12)00900-7/fulltext) (2024) (Dec. 2012).
63. Cancer Research UK. *Abdominal or pelvic radiotherapy side effects* en. Jan. 2024. <https://www.cancerresearchuk.org/about-cancer/treatment/radiotherapy/side-effects/abdominal-or-pelvic-radiotherapy-side-effects> (2024).
64. Nadrljanski, M. M. *Computed tomography | Radiology Reference Article | Radiopaedia.org* en-US. Jan. 2024. <https://radiopaedia.org/articles/computed-tomography> (2024).
65. Larsson, E.-M. & Wikström, J. in *Handbook of Clinical Neurology* (eds Kovacs, G. G. & Alafuzoff, I.) 579–599 (Elsevier, Jan. 2018). <https://www.sciencedirect.com/science/article/pii/B9780128023952000377> (2024).
66. Greenway, K. *Hounsfeld unit | Radiology Reference Article | Radiopaedia.org* en-US. Jan. 2024. <https://radiopaedia.org/articles/hounsfeld-unit> (2024).
67. Crawford, J. *Understanding Radiotherapy Part 2: How Much Radiation is the Right Amount?* en-US. May 2019. <https://reflexion.com/understanding-radiotherapy-part-2-how-much-radiation-is-the-right-amount/> (2024).
68. Zarepisheh, M. *et al.* Automated and Clinically Optimal Treatment Planning for Cancer Radiotherapy. *INFORMS journal on applied analytics* **52**, 69–89. ISSN: 2644-0865. <https://www.ncbi.nlm.nih.gov/pmc/articles/PMC9284667/> (2024) (2022).

69. Saw, C. B., Yakoob, R., Enke, C. A., Lau, T. P. & Ayyangar, K. M. Immobilization devices for intensity-modulated radiation therapy (IMRT). *Medical Dosimetry* **26**, 71–77. ISSN: 0958-3947. <https://www.sciencedirect.com/science/article/pii/S0958394700000595> (2024) (Mar. 2001).
70. Schmidt, M. A. & Payne, G. S. Radiotherapy Planning using MRI. *Physics in medicine and biology* **60**, R323–R361. ISSN: 0031-9155. <https://www.ncbi.nlm.nih.gov/pmc/articles/PMC5137785/> (2024) (Nov. 2015).
71. Vaz, S. C. *et al.* Joint EANM/SNMMI/ESTRO practice recommendations for the use of 2-[18F]FDG PET/CT external beam radiation treatment planning in lung cancer V1.0. en. *European Journal of Nuclear Medicine and Molecular Imaging* **49**, 1386–1406. ISSN: 1619-7089. <https://doi.org/10.1007/s00259-021-05624-5> (2024) (Mar. 2022).
72. INTERNATIONAL COMMISSION ON RADIATION UNITS AND MEASUREMENTS, (ICRU). “*Prescribing, recording, and reporting photon beam therapy (Supplement to ICRU Report 50)*” ICRU Report 62 (ICRU, Bethesda, Maryland, U.S.A., 1999).
73. Gardner, S. J., Kim, J. & Chetty, I. J. Modern Radiation Therapy Planning and Delivery. en. *Hematology/Oncology Clinics of North America* **33**, 947–962. ISSN: 08898588. <https://linkinghub.elsevier.com/retrieve/pii/S088985881930098X> (2024) (Dec. 2019).
74. Burnet, N. G., Thomas, S. J., Burton, K. E. & Jefferies, S. J. Defining the tumour and target volumes for radiotherapy. *Cancer Imaging* **4**, 153–161. ISSN: 1740-5025. <https://www.ncbi.nlm.nih.gov/pmc/articles/PMC1434601/> (2024) (Oct. 2004).
75. Van Herk, M., Remeijer, P., Rasch, C. & Lebesque, J. V. The probability of correct target dosage: dose-population histograms for deriving treatment margins in radiotherapy. *International Journal of Radiation Oncology*Biophysics*Physics* **47**, 1121–1135. ISSN: 0360-3016. <https://www.sciencedirect.com/science/article/pii/S0360301600005186> (2024) (July 2000).
76. INTERNATIONAL COMMISSION ON RADIATION UNITS AND MEASUREMENTS, (ICRU). “*Prescribing, recording, and reporting photon beam therapy*” ICRU Report 50 (ICRU, Bethesda, Maryland, U.S.A., 1993).
77. Cilla, S. *et al.* Template-based automation of treatment planning in advanced radiotherapy: a comprehensive dosimetric and clinical evaluation. en. *Scientific Reports* **10**. Publisher: Nature Publishing Group, 423. ISSN: 2045-2322. <https://www.nature.com/articles/s41598-019-56966-y> (2024) (Jan. 2020).

78. Hernandez, V. *et al.* What is plan quality in radiotherapy? The importance of evaluating dose metrics, complexity, and robustness of treatment plans. English. *Radiotherapy and Oncology* **153**. Publisher: Elsevier, 26–33. ISSN: 0167-8140, 1879-0887. [https://www.thegreenjournal.com/article/S0167-8140\(20\)30813-6/fulltext](https://www.thegreenjournal.com/article/S0167-8140(20)30813-6/fulltext) (2024) (Dec. 2020).
79. Yolanda Smith. *Radiation Therapy Treatment Process | OncoLink* Mar. 2021. <https://www.oncolink.org/cancer-treatment/radiation/introduction-to-radiation-therapy/radiation-therapy-treatment-process> (2024).
80. Unkelbach, J. *et al.* The role of computational methods for automating and improving clinical target volume definition. *Radiotherapy and Oncology. Physics Special Issue: ESTRO Physics Research Workshops on Science in Development* **153**, 15–25. ISSN: 0167-8140. <https://www.sciencedirect.com/science/article/pii/S0167814020308380> (2024) (Dec. 2020).
81. Erdur, A. C. *et al.* Deep learning for autosegmentation for radiotherapy treatment planning: State-of-the-art and novel perspectives. en. *Strahlentherapie und Onkologie*. ISSN: 1439-099X. <https://doi.org/10.1007/s00066-024-02262-2> (2024) (Aug. 2024).
82. Fouzia Altaf. *FIGURE 7: Typical process of segmentation with Deep Learning: A...* en. July 2019. https://www.researchgate.net/figure/Typical-process-of-segmentation-with-Deep-Learning-A-Convolutional-Neural-Network-CNN_fig5_334498427 (2024).
83. Primakov, S. P. *et al.* Automated detection and segmentation of non-small cell lung cancer computed tomography images. en. *Nature Communications* **13**, 3423. ISSN: 2041-1723. <https://www.nature.com/articles/s41467-022-30841-3> (2024) (June 2022).
84. Ronneberger, O., Fischer, P. & Brox, T. en. in *Medical Image Computing and Computer-Assisted Intervention – MICCAI 2015* (eds Navab, N., Hornegger, J., Wells, W. M. & Frangi, A. F.) Series Title: Lecture Notes in Computer Science, 234–241 (Springer International Publishing, Cham, 2015). ISBN: 978-3-319-24573-7 978-3-319-24574-4. http://link.springer.com/10.1007/978-3-319-24574-4_28 (2024).
85. Heilemann, G. *et al.* Clinical Implementation and Evaluation of Auto-Segmentation Tools for Multi-Site Contouring in Radiotherapy. English. *Physics and Imaging in Radiation Oncology* **28**. Publisher: Elsevier. ISSN: 2405-6316. [https://www.phiro.science/article/S2405-6316\(23\)00106-9/fulltext](https://www.phiro.science/article/S2405-6316(23)00106-9/fulltext) (2024) (Oct. 2023).

86. Netherton, T. J., Cardenas, C. E., Rhee, D. J., Court, L. E. & Beadle, B. M. The Emergence of Artificial Intelligence within Radiation Oncology Treatment Planning. en. *Oncology* **99**, 124–134. ISSN: 0030-2414, 1423-0232. <https://karger.com/OCL/article/doi/10.1159/000512172> (2024) (2021).
87. Borys, K. *et al.* Explainable AI in medical imaging: An overview for clinical practitioners – Beyond saliency-based XAI approaches. *European Journal of Radiology* **162**, 110786. ISSN: 0720-048X. <https://www.sciencedirect.com/science/article/pii/S0720048X23001006> (2024) (May 2023).
88. Brouwer, C. L. *et al.* Machine learning applications in radiation oncology: Current use and needs to support clinical implementation. *Physics and Imaging in Radiation Oncology* **16**, 144–148. ISSN: 2405-6316. <https://www.ncbi.nlm.nih.gov/pmc/articles/PMC7807598/> (2024) (Nov. 2020).
89. Robert, C. *et al.* Clinical implementation of deep-learning based auto-contouring tools—Experience of three French radiotherapy centers. *Cancer/Radiothérapie. 32e Congrès national de la Société française de radiothérapie oncologique* **25**, 607–616. ISSN: 1278-3218. <https://www.sciencedirect.com/science/article/pii/S1278321821001220> (2024) (Oct. 2021).
90. Meyer, P., Noblet, V., Mazzara, C. & Lallement, A. Survey on deep learning for radiotherapy. *Computers in Biology and Medicine* **98**, 126–146. ISSN: 0010-4825. <https://www.sciencedirect.com/science/article/pii/S0010482518301318> (2024) (July 2018).
91. Andratschke, N. *et al.* European Society for Radiotherapy and Oncology and European Organisation for Research and Treatment of Cancer consensus on re-irradiation: definition, reporting, and clinical decision making. en. *The Lancet Oncology* **23**, e469–e478. ISSN: 14702045. <https://linkinghub.elsevier.com/retrieve/pii/S1470204522004478> (2024) (Oct. 2022).
92. Paradis, K. C. *et al.* The Special Medical Physics Consult Process for Reirradiation Patients. *Advances in Radiation Oncology* **4**, 559–565. ISSN: 2452-1094. <https://www.sciencedirect.com/science/article/pii/S2452109419300612> (2024) (Oct. 2019).
93. Willmann, J. *et al.* Re-irradiation in clinical practice: Results of an international patterns of care survey within the framework of the ESTRO-EORTC E2-RADIatE platform. en. *Radiotherapy and Oncology* **189**, 109947. ISSN: 01678140. <https://linkinghub.elsevier.com/retrieve/pii/S0167814023898413> (2024) (Dec. 2023).
94. Minniti, G., Niyazi, M., Alongi, F., Navarria, P. & Belka, C. Current status and recent advances in reirradiation of glioblastoma. *Radiation Oncology (London, England)* **16**, 36. ISSN: 1748-717X. <https://www.ncbi.nlm.nih.gov/pmc/articles/PMC7890828/> (2024) (Feb. 2021).

95. Murray, L. *et al.* Treatment plan optimisation for reirradiation. en. *Radiotherapy and Oncology* **182**, 109545. ISSN: 01678140. <https://linkinghub.elsevier.com/retrieve/pii/S016781402300083X> (2024) (May 2023).
96. Fox, T., Elder, E. & Crocker, I. en. in *PET-CT in Radiotherapy Treatment Planning* 35–51 (Elsevier, 2008). ISBN: 978-1-4160-3224-3. <https://linkinghub.elsevier.com/retrieve/pii/B9781416032243500062> (2024).
97. Nix, M. *et al.* Dose summation and image registration strategies for radiobiologically and anatomically corrected dose accumulation in pelvic re-irradiation. en. *Acta Oncologica* **61**, 64–72. ISSN: 0284-186X, 1651-226X. <https://www.tandfonline.com/doi/full/10.1080/0284186X.2021.1982145> (2024) (Jan. 2022).
98. Zhang, A., Li, J., Qiu, H., Wang, W. & Guo, Y. Comparison of rigid and deformable registration through the respiratory phases of four-dimensional computed tomography image data sets for radiotherapy after breast-conserving surgery. *Medicine* **96**, e9143. ISSN: 0025-7974. <https://www.ncbi.nlm.nih.gov/pmc/articles/PMC5815729/> (2024) (Dec. 2017).
99. Dowling, J. A. & O'Connor, L. M. Deformable image registration in radiation therapy. *Journal of Medical Radiation Sciences* **67**, 257–259. ISSN: 2051-3895. <https://www.ncbi.nlm.nih.gov/pmc/articles/PMC7753986/> (2024) (Dec. 2020).
100. Nenoff, L. *et al.* Review and recommendations on deformable image registration uncertainties for radiotherapy applications. en. *Physics in Medicine & Biology* **68**, 24TR01. ISSN: 0031-9155, 1361-6560. <https://iopscience.iop.org/article/10.1088/1361-6560/ad0d8a> (2024) (Dec. 2023).
101. Murr, M. *et al.* Applicability and usage of dose mapping/accumulation in radiotherapy. English. *Radiotherapy and Oncology* **182**. Publisher: Elsevier. ISSN: 0167-8140, 1879-0887. [https://www.thegreenjournal.com/article/S0167-8140\(23\)00065-8/fulltext](https://www.thegreenjournal.com/article/S0167-8140(23)00065-8/fulltext) (2024) (May 2023).
102. Chiara Paganelli. “Patient-specific validation of deformable image registration in radiation therapy: Overview and caveats” - Paganelli - 2018 - *Medical Physics* - Wiley Online Library Sept. 2018. <https://aapm.onlinelibrary.wiley.com/doi/10.1002/mp.13162> (2024).
103. Brock, K. K., Mutic, S., McNutt, T. R., Li, H. & Kessler, M. L. Use of image registration and fusion algorithms and techniques in radiotherapy: Report of the AAPM Radiation Therapy Committee Task Group No. 132. *Medical Physics* **44**. Publisher: John Wiley & Sons, Ltd, e43–e76. ISSN: 0094-2405. <https://aapm.onlinelibrary.wiley.com/doi/10.1002/mp.12256> (2024) (July 2017).

104. Rong, Y. *et al.* Rigid and Deformable Image Registration for Radiation Therapy: A Self-Study Evaluation Guide for NRG Oncology Clinical Trial Participation. en. *Practical Radiation Oncology* **11**, 282–298. ISSN: 18798500. <https://linkinghub.elsevier.com/retrieve/pii/S1879850021000576> (2024) (July 2021).
105. Niebuhr, N. I. *et al.* Biologically consistent dose accumulation using daily patient imaging. *Radiation Oncology* **16**, 65. ISSN: 1748-717X. <https://doi.org/10.1186/s13014-021-01789-3> (2024) (Apr. 2021).
106. Stephan Klein & Marius Staring. *elastix, the manual* Jan. 2023. <https://elastix.dev/download/elastix-5.1.0-manual.pdf> (2024).
107. Mattes, D., Haynor, D. R., Vesselle, H., Lewellyn, T. K. & Eubank, W. *Non-rigid multimodality image registration* in *Medical Imaging 2001: Image Processing* **4322** (SPIE, July 2001), 1609–1620. <https://www.spiedigitallibrary.org/conference-proceedings-of-spie/4322/0000/Nonrigid-multimodality-image-registration/10.1117/12.431046.full> (2024).
108. Wasserthal, J. *et al.* TotalSegmentator: Robust Segmentation of 104 Anatomic Structures in CT Images. *Radiology: Artificial Intelligence* **5**, e230024. ISSN: 2638-6100. <https://www.ncbi.nlm.nih.gov/pmc/articles/PMC10546353/> (2024) (July 2023).
109. Maude Cornu. *Deformable image registration strategies for pelvic tumour sites* 2024.
110. NEMA. *1 Scope and Field of Application* 2024. https://dicom.nema.org/medical/dicom/current/output/chtml/part01/chapter_1.html#sect_1.1 (2024).
111. NEMA. *6 DICOM Information Model* 2024. https://dicom.nema.org/medical/dicom/current/output/chtml/part04/chapter_6.html (2024).
112. NEMA. *A Composite Information Object Definitions (Normative)* 2024. https://dicom.nema.org/medical/dicom/current/output/chtml/part03/chapter_A.html (2024).
113. Yaniv, Z., Lowekamp, B. C., Johnson, H. J. & Beare, R. SimpleITK Image-Analysis Notebooks: a Collaborative Environment for Education and Reproducible Research. en. *Journal of Digital Imaging* **31**, 290–303. ISSN: 1618-727X. <https://doi.org/10.1007/s10278-017-0037-8> (2024) (June 2018).
114. NEMA. *C.7.6.2 Image Plane Module* 2024. https://dicom.nema.org/medical/dicom/current/output/chtml/part03/sect_C.7.6.2.html#sect_C.7.6.2.1.1 (2024).
115. SimpleITK. *SimpleITK: itk::simple::ResampleImageFilter Class Reference* 2024. https://simpleitk.org/doxygen/latest/html/classitk_1_1simple_1_1ResampleImageFilter.html#a850affc7fc3ce420c04f754d5d7773a5 (2024).

116. Zou, K. H. *et al.* Statistical Validation of Image Segmentation Quality Based on a Spatial Overlap Index. *Academic radiology* **11**, 178–189. ISSN: 1076-6332. <https://www.ncbi.nlm.nih.gov/pmc/articles/PMC1415224/> (2024) (Feb. 2004).
117. Reinke, A. & Maier-Hein, L. Common limitations of performance metrics in biomedical image analysis. en (2021).
118. Taha, A. A. & Hanbury, A. Metrics for evaluating 3D medical image segmentation: analysis, selection, and tool. *BMC Medical Imaging* **15**, 29. ISSN: 1471-2342. <https://doi.org/10.1186/s12880-015-0068-x> (2024) (Aug. 2015).
119. WNY urology. *Cauda equina syndrome* Apr. 2020. <https://www.thebiketethebody.com/post/cauda-equina-syndrome> (2024).
120. Vogel, J. D. *et al.* The American Society of Colon and Rectal Surgeons Clinical Practice Guidelines for the Management of Colon Cancer. en. *Diseases of the Colon & Rectum* **65**, 148–177. ISSN: 0012-3706. <https://journals.lww.com/10.1097/DCR.0000000000002323> (2024) (Feb. 2022).
121. Yu, C. *et al.* Multi-organ segmentation of abdominal structures from non-contrast and contrast enhanced CT images. *Scientific Reports* **12**, 19093. ISSN: 2045-2322. <https://www.ncbi.nlm.nih.gov/pmc/articles/PMC9646761/> (2024) (Nov. 2022).
122. Joskowicz, L., Cohen, D., Caplan, N. & Sosna, J. Inter-observer variability of manual contour delineation of structures in CT. en. *European Radiology* **29**, 1391–1399. ISSN: 0938-7994, 1432-1084. <http://link.springer.com/10.1007/s00330-018-5695-5> (2024) (Mar. 2019).
123. Romanò, C. *et al.* Influence of different urinary bladder filling levels and controlling regions of interest selection on deformable image registration algorithms. en. *Physica Medica* **75**, 19–25. ISSN: 11201797. <https://linkinghub.elsevier.com/retrieve/pii/S1120179720301204> (2024) (July 2020).
124. Takayama, Y. *et al.* Evaluation of the performance of deformable image registration between planning CT and CBCT images for the pelvic region: comparison between hybrid and intensity-based DIR. en. *Journal of Radiation Research* **58**, 567–571. ISSN: 0449-3060, 1349-9157. <https://academic.oup.com/jrr/article/58/4/567/2966317> (2024) (July 2017).
125. Saleh-Sayah, N. K., Weiss, E., Salguero, F. J. & Siebers, J. V. A distance to dose difference tool for estimating the required spatial accuracy of a displacement vector field: Distance to dose difference analysis. en. *Medical Physics* **38**, 2318–2323. ISSN: 00942405. <http://doi.wiley.com/10.1118/1.3572228> (2024) (Apr. 2011).



Die approbierte gedruckte Originalversion dieser Diplomarbeit ist an der TU Wien Bibliothek verfügbar
The approved original version of this thesis is available in print at TU Wien Bibliothek.

Appendix

organ	2219	2281	2282	2319	2339	2390	2419	2551	2678	2694	Mean
Bladder	1	1	1	1	1	0	0	0	1	0	0.6
Bowel	1	1	1	1	1	0	1	0	1	0	0.7
Canal anal	1	0	0	0	0	0	0	0	0	0	0.1
Cauda equina	0	0	1	1	0	0	0	0	1	0	0.3
LumbSacPlex R	0	1	1	1	1	1	1	1	1	1	0.9
LumbSacPlex L	0	1	1	1	1	1	1	1	1	1	0.9
Rectum	1	0	1	1	1	1	1	1	1	1	0.9
Urethra	1	1	0	0	0	0	0	0	0	1	0.3

Table 5.1: Organs used as controlling ROIs in ContROI and Wall methods

Name	Tasks			patient	
CT1	export from RS*	import to 3DS*			
CT2	export from RS	import to 3DS			
CT1 STURCT	export from RS	import to 3DS			
Summed dose CT1	sum plan to evaluation	export from RS	import to 3DS		
CT1 seg	run TotalSegmentator				
CT2 seg	run TotalSegmentator				
DIR Transform	run Elastix				
DIR CT1 STRUCT	Transform				
DIR Summed dose CT1	Transform				
Export 3 studies from 3DS	[CT1 + seg]	[CT2 + seg + dose]	[CT2 + DIRSTR]		
new FoRs	CT1i* to CT1	CT2i* to CT2	CT2.2 to CT2		
Rename CTs	"CT1 imported"	"CT2 imported"			
Copy ROIs to CT2i	copy the 10 DIRSTR organs				
delete 3rd CT	delete				
Rename ROIs	4 AI-seg ROIs: "Name_3DS" 10 DIR ROIs: "DIR_Name_ReCare"				
Copy ROIs to original CTs	CT1i -> CT1	CT2i -> CT2			
create Rectum_3DS	in CT1	in CT2			
create CaudaEquina_3DS	in CT1	in CT2			
Excel seg CT1	Run Python script				
Excel seg CT2	Run Python script				
Excel Reg	Run Python script				
Quasirigid DIR	sphere in CT1	sphere in CT2	DIR without image info		
Sum DIR dose	in Plan evaluation RS		export		
Deform noCont ROI	in Plan evaluation RS		export		
Deform ContROI	in Plan evaluation RS		export		
Deform Wall	in Plan evaluation RS		export		
Deform quasiRigid	in Plan evaluation RS		export		
python RT	run script	import to RS			
mean RS check	weighted sum	check with Python mean			
Excel dose mean	Run Python script				
* 3DS: 3D Slicer, RS: RayStation, CT1i: CT1 imported, CT2i : CT2 imported					

Figure 5.1: Checklist method